ISSN 2408-2384 (ONLINE)

Environment and Natural Resources Journal

Volume 23 Number 2 March - April 2025

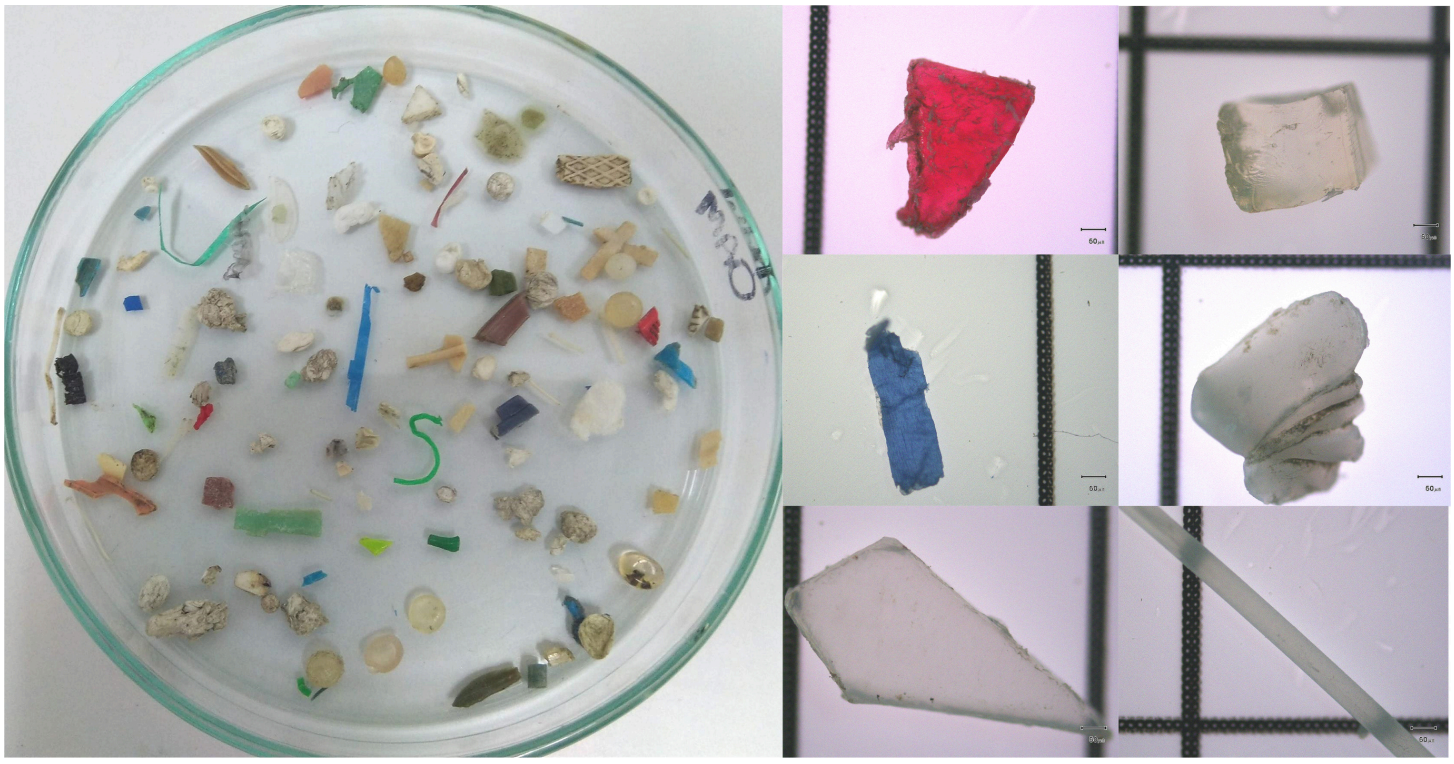

Microplastics observed in the wastewater inlet, showcasing various morphologies and colors

Source: Ta AT, Babel S, Klocke L, Haarstick A. Microplastic pollution in an urban wastewater treatment plant: Unravelling problems and proposing solutions. Page . 185-195

Scopus Clarivate Analytics EBSCO HOST DOAJ ASEAN CITATION INDEX TCI Thai-Journal Citation Index Centre

Environment and Natural Resources Journal (EnNRJ)
Volume 23, Number 2, March - April 2025 ISSN: 2408-2384 (Online)

AIMS AND SCOPE

The Environment and Natural Resources Journal is a peer-reviewed journal, which provides insight scientific knowledge into the diverse dimensions of integrated environmental and natural resource management. The journal aims to provide a platform for exchange and distribution of the knowledge and cutting-edge research in the fields of environmental science and natural resource management to academicians, scientists and researchers. The journal accepts a varied array of manuscripts on all aspects of environmental science and natural resource management. The journal scope covers the integration of multidisciplinary sciences for prevention, control, treatment, environmental clean-up and restoration. The study of the existing or emerging problems of environment and natural resources in the region of Southeast Asia and the creation of novel knowledge and/or recommendations of mitigation measures for sustainable development policies are emphasized.

The subject areas are diverse, but specific topics of interest include:

- Biodiversity
- Climate change
- Detection and monitoring of polluted sources e.g., industry, mining
- Disaster e.g., forest fire, flooding, earthquake, tsunami, or tidal wave
- Ecological/Environmental modelling
- Emerging contaminants/hazardous wastes investigation and remediation
- Environmental dynamics e.g., coastal erosion, sea level rise
- Environmental assessment tools, policy and management e.g., GIS, remote sensing, Environmental Management System (EMS)
- Environmental pollution and other novel solutions to pollution
- Remediation technology of contaminated environments
- Transboundary pollution
- Waste and wastewater treatments and disposal technology

Schedule

Environment and Natural Resources Journal (EnNRJ) is published 6 issues per year in January-February, March-April, May-June, July-August, September-October, and November-December.

Publication Fees

An article publication fee in the Environment and Natural Resources Journal is set at a rate of 250 USD per article, payable after the final acceptance of the manuscript.

Ethics in publishing

EnNRJ follows closely a set of guidelines and recommendations published by Committee on Publication Ethics (COPE).

Environment and Natural Resources Journal (EnNRJ)
Volume 23, Number 2, March - April 2025 ISSN: 2408-2384 (Online)

Editorial Office Address
Research and Academic Service, Research Management Unit,
Faculty of Environment and Resource Studies, Mahidol University
999, Phutthamonthon Sai 4 Road, Salaya, Phutthamonthon, Nakhon Pathom, Thailand, 73170
Phone +662 441 5000 ext. 2108
Website: https://ph02.tci-thaijo.org/index.php/ennrj/index
E-mail: ennrjournal@gmail.com

Environment and Natural Resources Journal (EnNRJ)

Volume 23, Number 2, March - April 2025 ISSN: 2408-2384 (Online)

CONTENT

Environment and Natural Resources Journal

Volume 23
Issue 2
2025

Effects of Biochar Amendment on CO_2 Evolution in Four Ecotypes of Leyte Sab-A Basin Peatland, Philippines

Pearl Aphrodite Bobon-Carnice[1,3,4*], Grechelle N. Socias[2], Mary Yolle S. Corcilles[1,4], Trisha Keith B. Abaño[1,4], and Uzzel Maureen H. Espanta[1,4]

[1]Department of Natural Sciences, Eastern Visayas State University, Tacloban City, Philippines
[2]Department of Chemistry, Eastern Visayas State University, Tacloban City, Philippines
[3]Office of Research and Development, Eastern Visayas State University, Tacloban City, Philippines
[4]Biodiversity and Soil Systems Laboratory, Eastern Visayas State University, Tacloban City, Philippines

ARTICLE INFO

Received: 3 Oct 2024
Received in revised: 8 Dec 2024
Accepted: 11 Dec 2024
Published online: 31 Jan 2025
DOI: 10.32526/ennrj/23/20240274

Keywords:
Biochar/ Carbon/ CO_2 evolution/ Peatland/ Ecotypes/ Land-Use

*** Corresponding author:**
E-mail:
pearl.carnice@evsu.edu.ph

ABSTRACT

Atmospheric carbon cycle criticisms are significant liabilities in existing predictions of future climate. Carbon dioxide (CO_2) discharges caused by climate warming through dense peat stores will frame a stable positive carbon cycle–atmospheric input. An experimental-descriptive analytical method was used to acquire data on quantifying the amount of CO_2 evolved in the four adjacent ecotypes of Leyte Sab-A Basin Peatland (LSBP), Philippines, both with and without biochar incorporation. Results showed that after 120 days of incubation, the CO_2 evolved between ecotypes measured 0.73 mg CO_2/g, 0.31 mg CO_2/g, 0.23 mg CO_2/g, and 0.20 mg CO_2/g for TML (marshland), TPF (peat forest), TAL (agricultural land), and TMV (mixed vegetation), respectively. In comparison, treatments with biochar were 0.81 mg CO_2/g, 0.57 mg CO_2/g, 0.46 mg CO_2/g, and 0.43 mg CO_2/g for TMLB (marshland+biochar), TPFB, TMVB, and TALB, respectively. Results rendered significant differences between ecotypes, and between those with added biochar (p-value: 1.8E-06). This study concludes that TML with and without biochar had the highest evolved CO_2 over time, implying the best ecosystem preservation among the ecotypes. For future studies, these findings establish a scientific basis for adaptive response assessment of peatlands to climate change, and for decisions made in support of policy changes.

1. INTRODUCTION

One of the most significant uncertainties in future climate projections is the interaction between the climate and the terrestrial carbon cycle (Kaur et al., 2022; Lu et al., 2021). The increased decomposition of deep peat deposits that have persisted for centuries to millennia may result in increased carbon dioxide (CO_2) outflow caused by climate change (Humpenöder et al., 2020). Several factors characterize this increased decomposition, including wildfires, human activities, and acidification. The decomposition process accelerated once these occurrences became continuous, releasing carbon dioxide (Jayasekara et al., 2024). As a result, a positive feedback loop may exist between the carbon cycle and the atmosphere. However, due to the limited duration or complementary nature of field discipline and the potential for disturbances during respiration measurements, the long-term climate sensitivity of carbon in peatlands, particularly at depth, remains uncertain.

Moreover, the peatlands are wetland ecosystems characterized by the accumulation of organic matter called “peat”, which derives from dead and decaying plant materials under high water saturation conditions (PAWB-DENR, 2013). It plays an essential role as a global carbon sink, and it stores up to 30% of the world’s soil organic carbon (SOC) pool despite covering only 3% of the Earth’s surface (Yao et al., 2022). Unfortunately, over half of Europe’s former peatland area has been damaged due

Citation: Bobon-Carnice PA, Socias GN, Corcilles MYS, Abaño TKB, Espanta UMH. Effects of biochar amendment on CO_2 evolution in four ecotypes of Leyte Sab-A Basin Peatland, Philippines. Environ. Nat. Resour. J. 2025;23(2):105-117. (https://doi.org/10.32526/ennrj/23/20240274)

to peat quarrying and land use changes such as drainage to make them suitable for agriculture or forestry (Joosten, 2016). Aeration of the soil is necessary for plant growth and makes the soil viable. On the other hand, the transition from anaerobic to aerobic conditions causes the rapid decomposition of peat that has accumulated under waterlogged conditions. As a result, the previous C-sink is now a significant source of atmospheric carbon dioxide (Du et al., 2022), and peatlands are known to be a significant contributor to global climate change issues (Humpenöder et al., 2020).

In the Philippines, there are two sites where peatlands have been confirmed—the Agusan Marsh (Alibo and Lasco, 2012) and the Leyte Sab-A Basin Peatland (LSBP) (Bobon-Carnice et al., 2023). The Leyte Sab-A Basin is located in the three barangays of the municipality of Alang-Alang, Leyte, namely Barangay Langit, Barangay Divisoria, Barangay Tabangohay, and Barangay San Isidro from the municipality of Sta. Fe, Leyte is located along the edges of the Mainit River Irrigation System. The Sab-A Basin is considered the most prominent water catchment area in Leyte. It is an elongated basin aligned northwest-southwest, situated northeast of the island of Leyte, near Tacloban City. The extreme northwest of the basin is somewhat isolated from the central basin by a ridge running south into the basin. Peat (Dolongan peat) is mainly found in the basin's central part, away from the surrounding ridges.

Around the margins of the basin, the Dolongan soil/peat mix is found, presumably since erosion from the surrounding ridges has deposited mineral soil at the foot of the ridges. Peat and mineral soil are interbedded in these areas. In addition, this peatland has been designated as a free zone for the protection, preservation, conservation, and restoration of unique ecosystem management areas due to the government's reclamation efforts. The said free zone has been used to focus on land management, which involves certain activities such as agriculture and settlements that serve the local community's economic needs. The eastern basin's undeveloped peatland is 1,288 ha and consists of marsh woodlands and grass/sedge peat swamp areas. A recent publication indicates that LSBP stores 36.6 Tg of C and could sequester 134.5 Tg of CO_2, representing 0.04% of the total tropical peat C (Bobon-Carnice et al., 2023). It is important to note that since their formation, peatlands have been both absorbing and emitting greenhouse gases (GHGs). As a result, it may take some time before the impact of CO_2 sequestration in peat is observed, but it is believed that the benefits of CO_2 sequestration in peat outweigh the benefits of methane (CH_4) emissions. Peatlands have been studied and found to be CO_2 sinks in some years and sources in others, depending on the climate. As concerns about climate change grow, efforts to assess soil carbon pool capacity and alterations have been reignited (Jackson et al., 2017). Most field studies on soil CO_2 budget measure CO_2 effluxes at the surface and CO_2 concentrations within the soil. Surprisingly, determining CO_2 effluxes provides a clear picture of its production in the land, and its emissions from depleted, carbon-rich soils like peatlands are becoming increasingly recognized as critical to the global carbon cycle (Hermans et al., 2022).

The reaction to climatic warming via CO_2 evolution has been considered worldwide for the most recent decades. In contrast, CO_2 development and soil carbon mineralization have been paid incredible acknowledgment for their massive impact on the global carbon cycle and terrestrial biological systems. Soil respiration is the CO_2 emission from soils, providing insight into soil carbon stocks and inputs. This flux influences the global carbon cycle as a potential regulator of the global greenhouse effect and climate. Temperature is often positively associated with soil respiration rates. As a result, higher temperatures are frequently associated with escalated soil respiration estimations, accelerating carbon cycling via autotrophic respiration and contributing to a potentially substantial positive response to climatic warming via heterotrophic soil carbon respiration (Tang et al., 2019). It has been thought that the recent rise in global temperature due to climate change has caused a higher estimate of soil respiration.

Consequently, it has led to a more significant greenhouse effect and a positive reaction loop for climate change. On the other hand, most field investigations of soil CO_2 budgets only assess CO_2 effluxes at the surface and its concentrations within the soil, providing only a limited view of CO_2 production in the soil. CO_2 evolution rates can be used to assess the effects of inorganic and organic matter on soil and its use. Several factors influence the mineralization of organic materials, including deposit quality or composition, soil temperature, water availability, and soil properties (Weber and Quicker, 2018).

Therefore, reducing greenhouse gas emissions and extracting CO_2 from the atmosphere are essential to minimizing climate change's adverse effects. A comprehensive examination is required before

investing in and executing these techniques to make educated decisions. One possible option for removing CO_2 from the environment is biochar production, which involves roasting biomass without oxygen to create a stable, carbon-rich material. Initial research on using biochar as a soil amendment is still in its infancy, but preliminary findings indicate that it may reduce the requirement for supplementary fertilizers and water. Through enhancing soil carbon sequestration, biochar has the potential to significantly contribute to climate change mitigation (Chagas et al., 2022). According to Söderqvist (2019), the pyrolysis process reforms the fast degradable carbon compounds in the biomass into more stable structures in the biochar. These carbon structures are more resistant to degradation than the original carbon compounds in the biomass. From this, the amount of carbon in the atmosphere circulating in the fast cycle can be reduced when carbon is introduced into a slower carbon cycle. This can be seen in contrast to burning fossil fuels, which release carbon from long-term storage into the atmosphere (Qambrani et al., 2017).

Biochar is increasingly recognized as a good soil amendment for nutrient retention and water-holding capacity (Rubin et al., 2022). Its peat incorporation could help mitigate nutrient leaching, enhance plant growth, and support restoration efforts (Cai et al., 2021). Soil acidity is a common problem for denuded peatlands, and adding biochar could buffer it, creating a more favorable environment for microbial activity and vegetation recovery (Wang et al., 2024). It has also been found to restrain GHG emissions, improving soil carbon sinks (Mosa et al., 2023) and peat stabilization (Ritter et al., 2022). Nevertheless, this study has yet to test the performance of biochar with peat if its decomposition dynamics are the same with mineral soils.

In this light, the researchers pursue the conduct of this study with the primary purpose of quantifying the CO_2 evolution rates of distinct peatland ecotypes and assessing the possibility of biochar to mitigate climate change by inhibiting carbon dioxide evolution in peatland ecosystems. This study's findings are expected to substantially impact understanding the biochar's effectiveness in mitigating climate change and on future land use and carbon sequestration plans. By studying the impacts of biochar on CO_2 evolution rates in several peatland ecotypes, this work gives essential insights into the feasibility and potential benefits of employing biochar as a strategy for carbon sequestration in peatland ecosystems.

2. METHODOLOGY

2.1 The study site

The study was conducted in Leyte Sab-A Basin Peatland (LSBP). Samples were taken from the three barangays of the municipality of Alang-Alang, Leyte, Philippines, namely Barangay Langit, Barangay Divisoria, Barangay Tabangohay, and Barangay San Isidro in the municipality of Sta. Fe, Leyte, Philippines. The site presented in Figure 1 is located along the edges of the Mainit River Irrigation System. It has 3,088.00 ha, of which over half has been reclaimed for agriculture (Bobon-Carnice et al., 2023). The remaining unutilized peatland of 1,288 ha in the basin's eastern part consists of a small swamp forest and sedge/grass peat swamp (PAWB-DENR, 2013).

2.2 Sampling procedure

Four ecosystem types were identified in Sab-A Basin, Leyte: marshland (ML), peat forest (PF), agricultural land (AL), and mixed vegetation (MV). Topsoil (0-20 cm) from these ecosystem types was collected using core samples: three for soil incubation and one for bulk density, moisture content, and oven-dried weight (ODW) measurement. One-time sampling was done to collect the peat substrate after a day of site visit and ecosystem re-assessment.

2.3 Biochar preparation

The study used an improvised pyrolyzer to produce pyrolysis from poultry litter. This improvised pyrolyzer comprises a cylindrical tin can (with lid), which is 10 inches high and 3 inches radius, and a rectangular tin can, whose capacity is 15 kg with a complete measurement of 24×15×15 inches. To produce the pyrolysis, the researchers poured one kilogram of feedstock inside a cylindrical tin sealed with its lid. Then, the said tin was placed inside a rectangular tin can with fire at about 400-600°C heat temperature. The procedure lasted approximately 6-8 h until the poultry litter turned into biochar. After eight hours, the biochar was removed from the pyrolyzer and cooled for 5 to 10 min until the biochar's temperature moved to 40°C. After the cooling process, it was crushed, pulverized, and homogenized to its desired size, 1-2 mm in range, using a wooden mallet. This crushed poultry litter biochar was set aside and prepared for the next experiment.

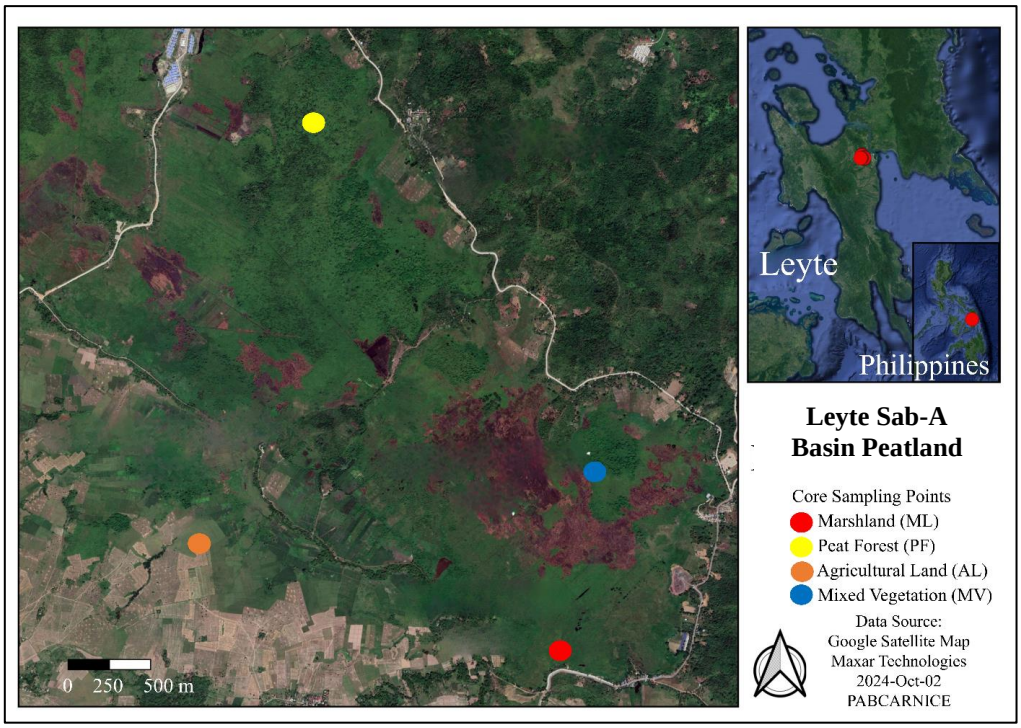

Figure 1. Map of sampling sites in Sab-A Basin, Leyte, Philippines.

2.4 Incubation

This process used fresh, top peat samples as the primary substrate. This experiment formulated nine treatments (TML (marshland), TPF (peat forest), TAL (agricultural land), TMV (mixed vegetation), BIOCHAR (biochar, no peat samples), TPFB (peat forest+biochar), TMLB (marshland+biochar), TALB (agricultural land+biochar), and TMVB (mixed vegetation+biochar)) with three replications each. All the ecosystem peat samples were put inside a glass jar measuring 8" in height × 2.5" in diameter, with a total capacity of 400 g. Each glass jar contains 25 g of peat substrate, and treatments with biochar were incorporated with 5 g. Then, biochar was evenly spread. Subsequently, the samples were then transferred to the laboratory facility of Eastern Visayas State University, Tacloban City, where the experimental set-up was located. The samples were stored in a closed room with a controlled temperature not exceeding 35°C and no exposure to direct sunlight. As a controlled experiment, three additional glass jars containing only 15 mL of NaOH were labeled TO1, TO2, and TO3. The experimental design employed a randomized complete block design (RCBD), and various treatments were analyzed over 120 days. The indicated number of incubation days under controlled conditions has been validated to be enough to detect short – to medium-term decomposition experiments (Nikonova et al., 2023; de Jong et al., 2020; Jian et al., 2020; Hogg et al., 1992).

2.5 Carbon dioxide evolution determination

The evolved carbon dioxide was measured using a standard method (Anderson, 1982; Jenkinson and Powlson, 1976). The peat samples were placed in jars with 15 mL of 0.1 sodium hydroxide (NaOH) solution, and the jars were tightly sealed to prevent CO_2 exchange with the atmosphere. After every three days of exposure, the NaOH was collected and titrated with 0.05 N hydrochloric acid (HCl) solution and 0.05 N barium chloride ($BaCl_2$) solution using a phenolphthalein indicator. Each ecotype's moisture content was calculated, and about 3-5 mL of water was added to emulate its natural moisture content, estimated at 50-70%. Water is added every time the substrate's water content is visibly reduced based on the watermark outside the jar. The following formula was used to calculate the milligrams of CO_2 evolved and grams of organic material decomposed for each treatment (Jennings et al., 2010):

$$\text{Milligrams C or } CO_2 = (B - V)\,NE$$

Where; V=volume (mL) of acid to titrate the alkali in the CO_2 collectors from the treatments to the endpoint; B=volume (mL) of acid to titrate the alkali

in the CO_2 collectors from the control to the endpoint; N=normality of acid; E=equivalent weight.

*If data are expressed in terms of carbon, E=6. *If data are expressed in terms of carbon dioxide, E=22. The evolved and cumulative carbon dioxide were expressed as mg CO_2/g peat soil.

2.6 Calculation and data analysis

In order to calculate the percentage weight of the different treatments, the oven-dry weight of each treatment subtracted from the initial weight was determined. The initial weight is calculated by taking the difference between the weight of the different amendments and the moisture content. This calculation is essential to determine the effectiveness of the different treatments for reducing carbon dioxide emissions and increasing carbon sequestration.

A one-way analysis of variance (ANOVA) was performed, following the Duncan Multiple Range Test (DMRT), at a significance level of 0.05 to identify whether there were statistically notable differences between the treatments. In addition, linear regression was employed to evaluate the correlations between the impacts of biochar on CO_2 evolution, between temperature and the number of days of decomposition, and between CO_2 evolution and the number of days of decomposition.

3. RESULTS AND DISCUSSION

3.1 Biochar effect on the degree of decomposition

During the first seven days of peat ecotypes' decomposition, the CO_2 evolved in the process was low, with values of 0.17 mg CO_2/g (ML), 0 mg CO_2/g (PF), 0 mg CO_2/g (MV), and 0.10 mg CO_2/g (AL). This is attributed to the commencement of the decomposition process in the initial stage, with the rate expected to increase gradually over time (Abro et al., 2011). Moreover, the CO_2 evolution of TPF, TMV, and TAL was also low in the first seven weeks and gradually increased through the following weeks until the last day of incubation, as shown in Figure 2.

The results were consistent in that the rate of evolved carbon dioxide was low (1.43 g/kg) in the first week of incubation and continuously increased until the last day. Conversely, TML showed a significant increase on the fourth day, contradicting the results of Abro et al. (2011). Nevertheless, some results may be consistent with the results that TML showed. The previous studies of Hossain et al. (2017) and Rahman et al. (2014) showed that the maximum carbon dioxide emission was found and recorded during the first week of incubation.

The lowest CO_2 evolved rates were recorded from Day 1 to Day 54 for treatments PF (0 mg CO_2/g), MV (0 mg CO_2/g), and AL (0.05 mg CO_2/g), but ML's lowest CO_2 evolved rates of 0.17 mg CO_2/g were recorded from Day 3.

Moreover, Figure 2 demonstrated that after 120 days of decomposition, TML (0.51 mg CO_2/g) obtained the highest degree of decomposition due to the highest evolved CO_2, seconded by TPF (0.34 mg CO_2/g), TAL (0.24 mg CO_2/g), and TMV (0.01 mg CO_2/g), which attained the lowest degree of decomposition.

TML, attaining the highest evolved CO_2, in which its decomposition patterns show rapid decomposition from Day 3 to Day 111. It was observed that on the 111th day, TML had its highest decomposition peak due to its anoxic wet condition. Moreover, there was a decrease in CO_2 from Day 111 to Day 120 due to the remaining organic materials that are slowly decomposable. The implication of this result may vary on the peat-soil carbon storage mechanisms of ML that influence the destabilization/stabilization of the SOC; it relates to the peat ecotype biotic components that impact the ecotype decomposition. In this study, marshland dominated by herbaceous floras and its wet characteristics may implicate the rapid decomposition resulting in evolved carbon dioxide ascending.

Figure 3 revealed that after 120 days of decomposition, BIOCHAR (4.04 mg CO_2/g) attained the highest degree of decomposition due to the highest evolved CO_2, seconded by TMLB (1.53 mg CO_2/g), then TPFB (1.21 mg CO_2/g), followed by TMVB (1.17 mg CO_2/g), and TALB (1.09 mg CO_2/g) is the lowest.

Compared to the unamended peat soil, peat respiration was significantly higher in the peat ecotypes with biochar incorporation. The results are the same as the study of Cheng et al. (2018), in which incorporating biochar into the peat soil increased its respiration with the increasing incubation time and high temperature. All the treatments with biochar incorporation (Figure 3) increased the CO_2 evolution relative to the control (BIOCHAR), which ranges from 0-4 CO_2 mg/g compared to the unamended treatments (Figure 2), which only ranges from 0-1.5 CO_2 mg/g. Biochar attains the highest evolved CO_2, and its decomposition patterns show a steady decomposition rate from Day 60 to Day 120. Further, it was observed that on the 15th day, biochar had its highest

decomposition peak. This response could be attributed to the loss of C from the biochar itself and the abiotic release of CO_2 from biochar minerals formed during pyrolysis (Amalina et al., 2022; Jones et al., 2012). It also implies that the maximum carbon dioxide emission on the 15th day was recorded due to a high temperature (27.6°C) (Zhao et al., 2017). The said results contrast with other articles that experimented on sandy loam soil (Lu et al., 2014), which suppressed decomposition, also with biochar as a soil amendment (Hua et al., 2014), and with biochar and straw incorporation (Hou et al., 2020). Further, straw composting experiments inhibit CO_2 release (Lin et al., 2022), and the same is true with the soils amended with cornstalk biochar with different rations (Zhou et al., 2023).

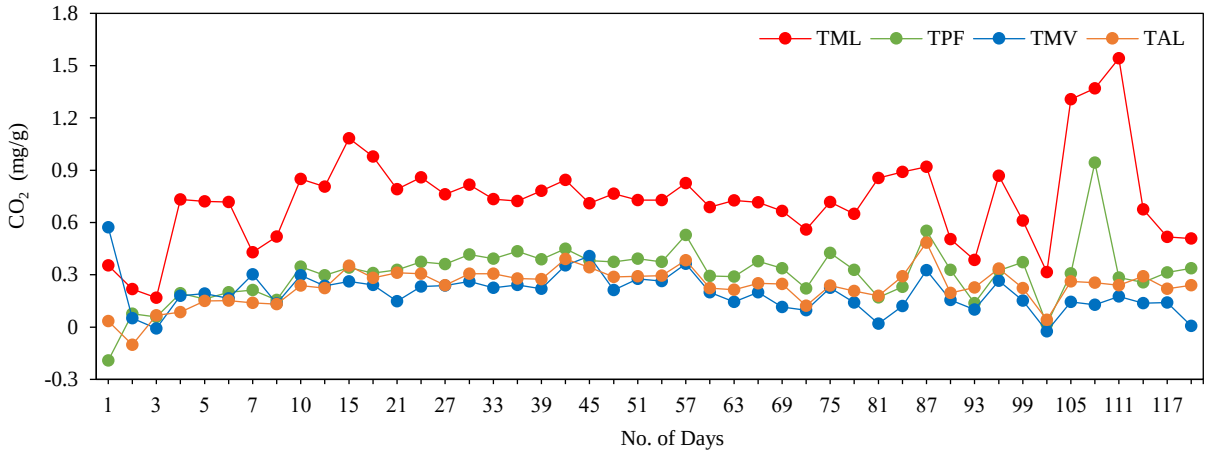

Figure 2. CO_2 (mg/g) evolved of peat ecotypes after 120 Days of decomposition

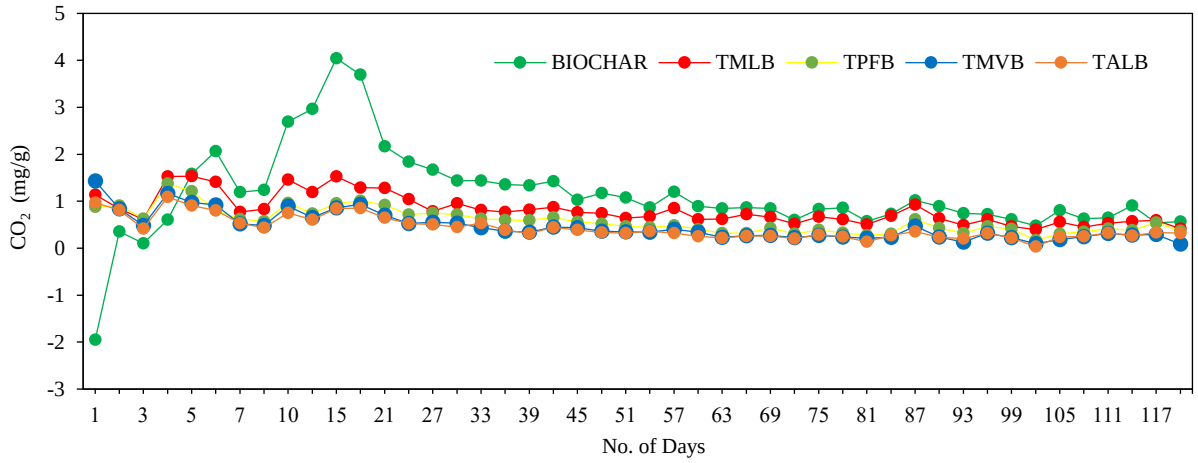

Figure 3. CO_2 (mg/g) evolved of peat ecotypes with biochar incorporation after 120 Days of decomposition.

3.2 Carbon dioxide evolution

Figure 4 shows that TML (R^2=0.0602), TPF (R^2=0.0961), TMV (R^2=0.1115), and TAL (R^2=0.0812), which means that only 6.02% (TML), 9.61% (TPF), 11.15% (TMV), and 8.12% (TAL) of the CO_2 evolved variation are explained by the number of days of. These low values imply that the number of days is not a strong predictor of CO_2 evolution. The majority of the variation could be due to other factors that affect CO_2 evolution, such as peat moisture, peat temperature, organic matter availability, and microbial activity, which may fluctuate independently of time (Vandecasteele, 2023; Rankin et al., 2022).

On the other hand, adding biochar to the different ecotype substrates rendered contrasting results. Figure 5 shows that for Biochar (R^2=0.1219), TMLB (R^2=0.5686), TPFB (R^2=0.6039), TMVB (R^2=0.5923), and TALB (R^2=0.5734), which implies that 56.86% (TMLB), 60.39% (TPFB), 59.23% (TMVB), and 57.34% (TALB) that number of days progresses, there is a significant and predictable change in CO_2 evolution rates. This potentially means that adding biochar to the

different ecotypes of peat substrates increases microbial activity and decomposition of organic matter (Deshoux et al., 2023; Xiang et al., 2023; Bobon-Carnice, 2014). Nevertheless, even with such results, the model leaves the remaining variation unexplained; it cannot be neglected as CO_2 evolution can be affected by other variables such as temperature (a by-product of decomposition) and moisture content of the different ecotypes (Jiang et al., 2024). On the other hand, it is expected that biochar (R^2=0.1219) treatment alone would render a weak linear relationship with time as it does not contain any peat substrate, and biochar alone has high recalcitrance to decomposition (Azzi et al., 2024) and is interestingly comparable to the results of the peat ecotypes without biochar.

It has been reported that when biochar is used as a soil amendment, it stimulates soil fertility and improves soil quality by increasing soil pH, increasing the ability to retain moisture, attracting more useful fungi and other microbes, improving the ability of cation exchange, and preserving the nutrients in the soil (Ajema, 2018). Additionally, the study of Sovova et al. (2021) discovered that biochar's efficacy differed between peat soil ecotypes. This may imply the reason for the difference in the relationship between the treatments and biochar application.

In contrast, Cheng et al. (2018) argue that abiotic CO_2 release is unlikely to explain the observed increase, as contributions from this source would typically increase with higher biochar production temperatures due to decreased colloidal mineral content and an increase in metal oxide formation (Angın, 2013). The additional CO_2 could, therefore, originate from the microbial-induced solubilization and breakdown of the biochar (Jiang et al., 2016). Overall, the results imply that treatments with biochar incorporation were significantly higher than those without.

Peat ecotypes with and without biochar amendment exhibited a linear inclination with significant differences during incubation, as shown in Figure 4 and Figure 5. Moreover, ecotypes with 5 g biochar addition significantly increased the evolved CO_2 between the 15th and 20th day. These outcomes were dependable with the study of Rahman et al. (2014), who stated that organic deposits significantly increased when biochar was added compared to treatments without biochar.

3.3 Cumulative value of CO_2 (mg) evolved and percentage weight loss

Cumulative CO_2 (mg/g peat soil) value on peat ecotypes without biochar varied slightly in all four treatments after 120 days of incubation. From Day 1 to Day 120, ML (33.64 mg/g peat soil) tends to have the highest cumulative CO_2 value (Figure 6). On the 10th day and onwards, the decomposition of the four treatments significantly increased.

The overall cumulative value of CO_2 (mg/g peat soil) evolved of TML, TPF, TAL, and TMV (mixed vegetation) is 33.64, 14.20, 10.76, and 9.04, respectively, which implies that TML has the highest degree of decomposition, and TMV has the lowest (Figure 6). TML (marshland) accumulated the highest carbon dioxide evolved compared to the other treatments because of their anoxic wet conditions. Marshland ecosystems provide an optimum natural environment for the sequestration and long-term storage of carbon dioxide (CO_2) from the atmosphere (Mitsch et al., 2013), possibly due to TML accumulating the highest carbon dioxide evolution.

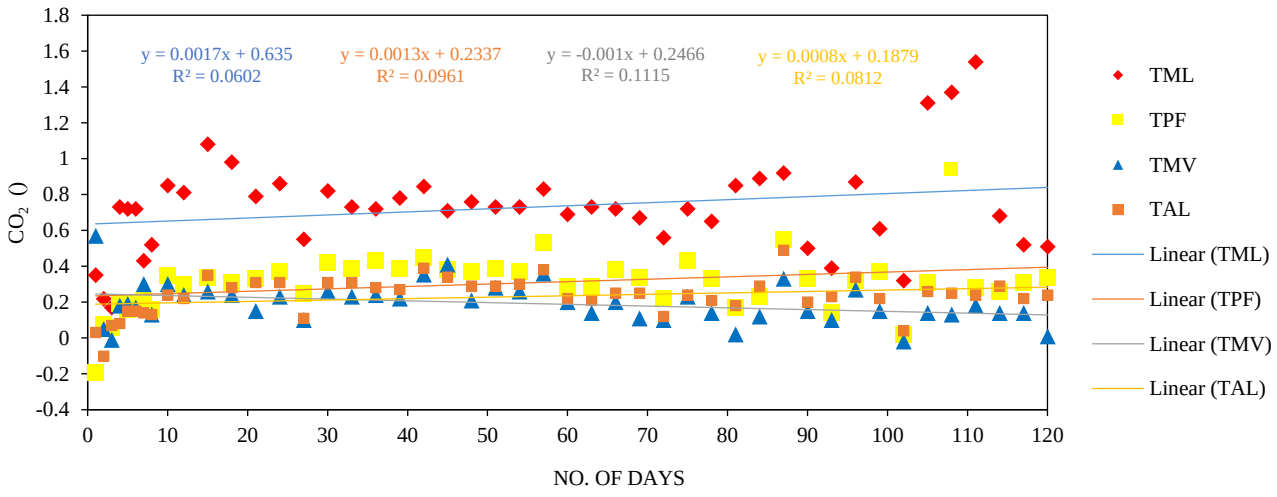

Figure 4. Linear regression analysis of peat ecotypes with biochar CO_2 evolved and the number of days of decomposition

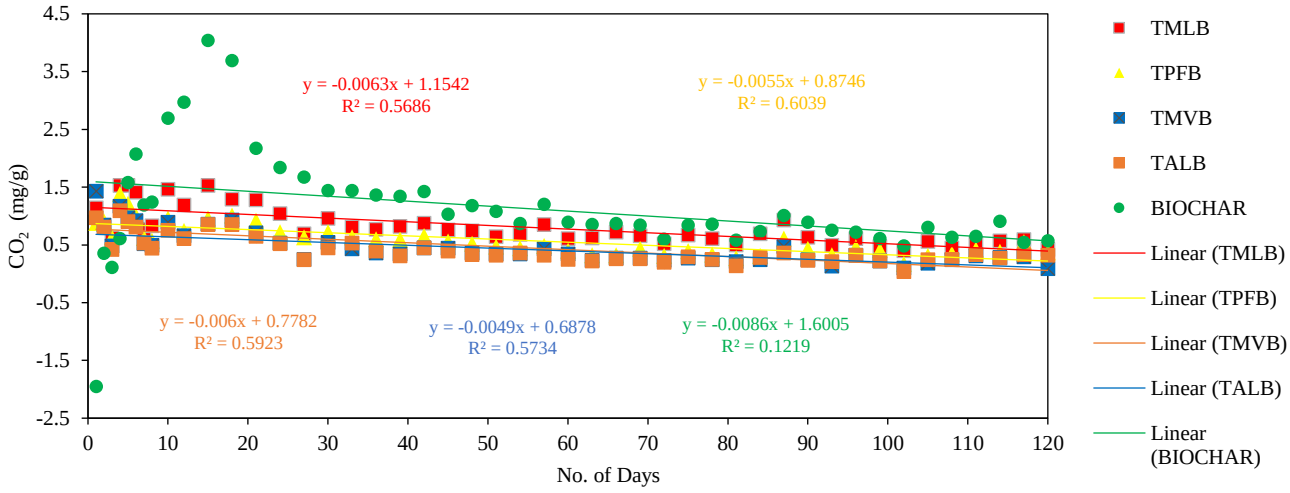

Figure 5. Linear regression analysis of peat ecotypes without biochar CO_2 evolved and the number of days of decomposition

The implication of this result varies on the ecotype characteristics and components (abiotic and biotic) that influence the mechanism of the peat soil on rapid decomposition. The effect of ecotypes on the cumulative emission of CO_2 at the end of 120 days of incubation was significant ($F=65.55$, $p<0.05$).

TPF lost about 79.83% of its total ODW for 120 days, while TML, TAL, and TMV attained 77.51%, 51.73%, and 51.35%, respectively. This could be due to TPF vegetation being dominated by forest trees that have not been degraded yet, with the probability of a high percentage of bioavailable carbon in its substrate that could be easily decomposed (Jayasekara et al., 2024). TML evolved the highest carbon dioxide (Figure 7), which is directly proportional to weight loss, as in the case of the other three treatments. Such high CO_2 evolution compared to other ecotypes could be due to the fine root systems of the marshland (Dargie et al., 2024), which are dominated by macrophytes (Bobon-Carnice et al., 2023). On the other hand, treatment TMV attained the lowest carbon dioxide evolution (Figure 6) and the lowest percentage of weight loss (Figure 7). This could be due to peat compaction due to anthropological intervention where different trees and a mix of agricultural tillage are being practiced.

Cumulative CO_2 (mg/g peat soil) value on peat ecotypes with added biochar varied slightly in all five treatments after 120 days of incubation. From Day 1 to Day 120, BIOCHAR (biochar alone) tends to have the highest cumulative CO_2 value. Subsequently, on the 10^{th} day and onwards, the five treatments significantly increased the degree of decomposition (Figure 8). The reason BIOCHAR alone accumulated the highest carbon dioxide evolved compared to the other four treatments is that BIOCHAR could be due to the process of pyrolyzing it; the pyrolysis process seriously affects the quality of biochar and its potential value in carbon sequestration (Rawat et al., 2019). Furthermore, it has been reported that when biochar is used as a soil amendment, it stimulates soil fertility and improves soil quality by increasing soil pH, increasing the ability to retain moisture, attracting more useful fungi and other microbes, improving the ability of cation exchange, and preserving the nutrients in the soil (Ajema, 2018). Moreover, it can be further analyzed in the study of Sovova et al. (2021) on the impacts of biochar application on soil characteristics and plant growth across several peat soil ecotypes. The study concluded that biochar application enhanced plant growth by enhancing soil parameters like pH, cation exchange capacity, and water-holding capacity. Therefore, it may imply the reason for the exponential increase of evolved carbon in all the peat ecotypes with added biochar as an amendment.

Treatment MLB lost about 67.19% of its total ODW for 120 days, while TPFB, BIOCHAR, TALB, and TMVB attained 62.89%, 59.62%, 48.67%, and 45.07%, respectively (Figure 9). As with the other treatments, BIOCHAR and TMLB evolved the highest carbon dioxide, directly proportional to weight loss. Conversely, treatment ALB attained the lowest carbon dioxide evolved, which should supposedly have the lowest weight loss. Despite this, results (Figure 9) revealed that TMVB recorded the lowest weight loss of its total ODW for 120 days.

Overall cumulative value of CO_2 (mg/g peat soil) evolved of BIOCHAR (biochar alone), TMLB (marshland+biochar), TPFB (peat forest+biochar), TMVB (mixed vegetation+biochar), and TALB

(agricultural land+biochar) is 52.22, 37.42, 26.58, 21.14, and 19.81, respectively, which implies that BIOCHAR (biochar alone) has the highest degree of decomposition, TMLB (marshland+biochar) is next, and TALB (agricultural land+biochar) has the very slightest degree of decomposition. The results imply that biochar addition to TALB could enhance weight loss during decomposition but not much with carbon dioxide evolution. To this, treatment BIOCHAR has a higher evolved carbon dioxide, which is not much compared to weight loss. It further implies that incorporating biochar into the peat significantly reduced weight loss by 45% with 5 g of biochar application on each peat ecotype.

Current results show that the biochar treatments (Figure 8) exhibited higher cumulative CO_2 evolution than those without biochar (Figure 6). This could be due mainly to the significantly higher emission of CO_2 in the first two weeks. Some studies have reported similar results by Troy et al. (2013), Rogovska et al. (2011), and Keith et al. (2011), which indicated that labile C in biochars could effectively lead to an increase in CO_2 emission. Furthermore, the study of Tomczyk et al. (2020) shows that the biochar produced at lower temperatures induced more cumulative CO_2 emissions. Consequently, Giweta's (2020) review highlights the significant influence of environmental factors such as temperature, moisture, and soil pH on decomposition. In addition, it is worth noting that in real environments, it does not account for natural variability such as temperature and moisture fluctuations, soil microbial diversity, environmental factors (rainfall, erosion), and field heterogeneity (soil texture, pH, varying organic content). However, baseline understanding is essential before conducting field studies and large-scale applications.

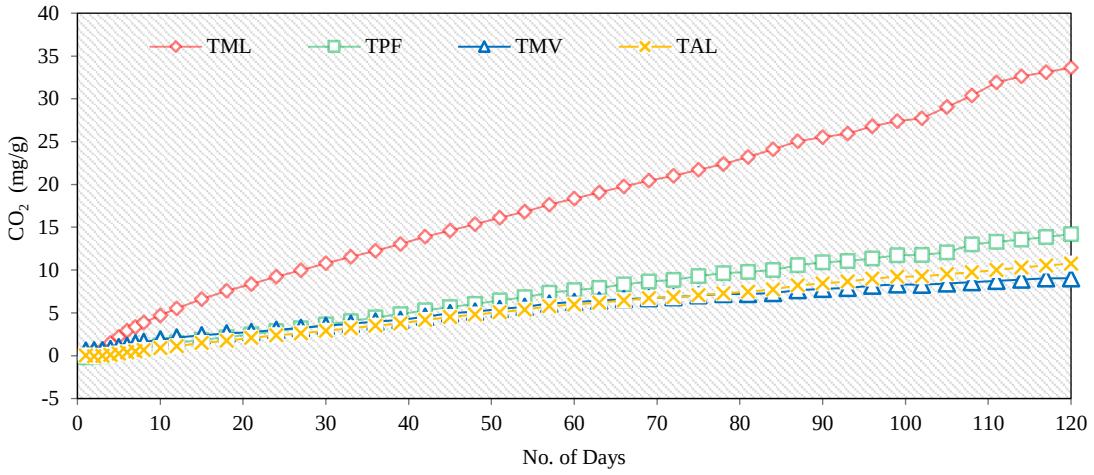

Figure 6. Cumulative value of CO_2 (mg/g) evolved of the peat ecotypes without biochar for 120 days

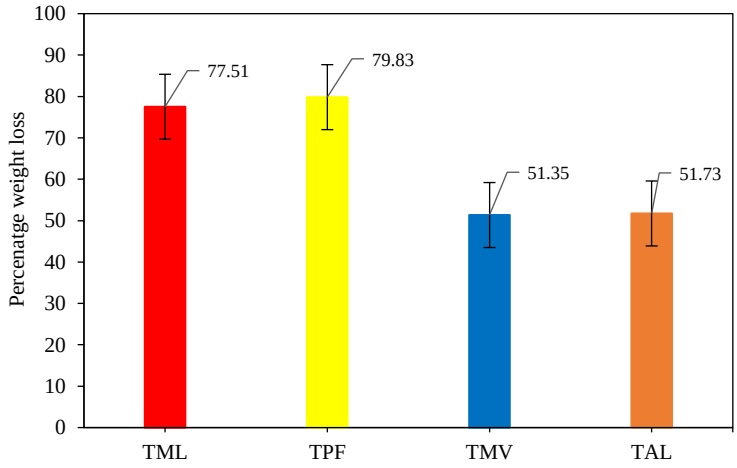

Figure 7. Percent weight loss of the peat ecotypes without biochar after 120 days

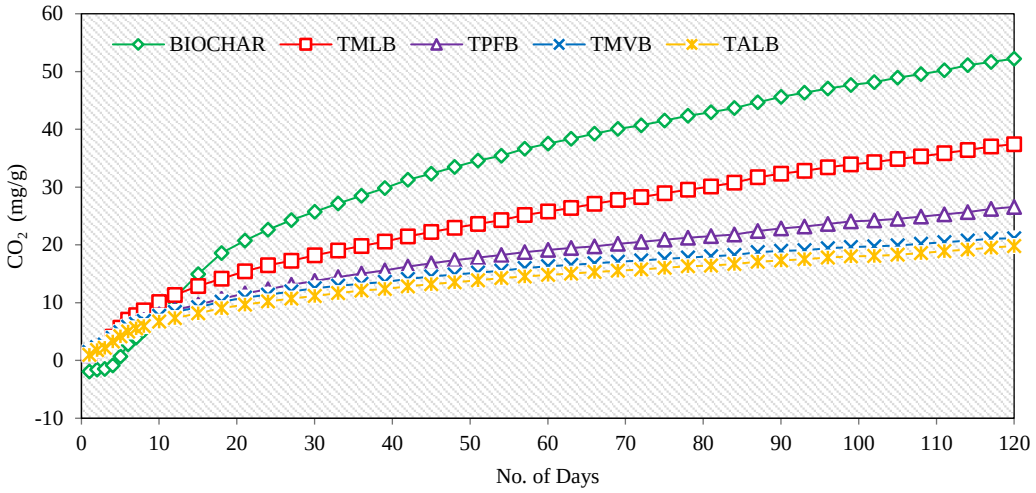

Figure 8. Cumulative value of CO_2 (mg/g) evolved of the peat ecotypes with biochar for 120 days

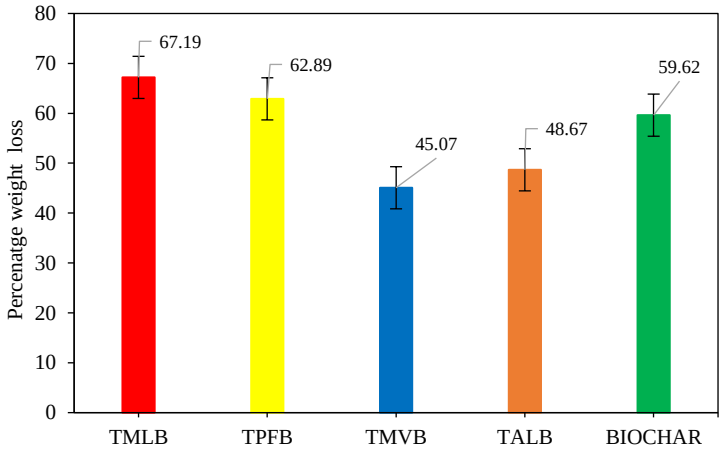

Figure 9. Percent weight loss of the peat ecotypes with biochar after 120 days

According to the results shown in Table 1, the differences in cumulative CO_2 evolution between the treatments with and without biochar are insignificant ($p>0.05$) between PF (12.38 CO_2 evolved/g), MV (12.10 CO_2 evolved/g), and AL (9.06 mg CO_2 evolved/g) but significantly different with ML (3.79 CO_2 evolved/g). The highest cumulative CO_2 evolution was observed in ML, both with and without biochar. It may be attributed to its anorexic wet condition compared to other peat ecotypes. It is consistent with Jien et al. (2015) claim that the effects of the initial labile C pool on the cumulative CO_2 emission may vary according to its soil texture and soil pH, which are suggested to be critical control factors in carbon decomposition or CO_2 emission. It was also stated in the study of Shen et al. (2021) that marshlands' carbon sequestration function is critical to slowing climate change and maintaining regional environmental stability. Wetland carbon sequestration capacity is reflected in part by vegetation biomass. This further coincides with the recent paper of Bobon-Carnice et al. (2023) on the same area where ML rendered the highest C-stocks (15,289.13 mg/ha) among other ecotypes. Therefore, investigating the biomass of marsh vegetation can provide a scientific foundation for estimating marshes' carbon storage and sequestration capacity. It is hypothesized that ML contains organic material that is susceptible to decomposition due to its type of vegetation that is dominated by grasses and sedges, comparing it to PF, which contains trees with higher lignin content, and with MV and AL that is already disturbed and peat is already mixed with mineral soil. The future findings can provide a scientific foundation for accurately evaluating the adaptation actions of wetland ecosystems to climate change and decision support for the adaptive management of wetland ecosystems. In contrast, the lowest cumulative carbon dioxide emission was observed in MV without added biochar.

Table 1. Cumulative value difference of the peat ecotypes with and without biochar

Peat ecotypes	Cumulative value of CO_2 (mg/g) evolved		Cumulative value difference (CO_2 mg/g)
	With biochar	Without biochar	
Marshland (ML)	37.42[a]	33.64[a]	3.79[a]
Peat forest (PF)	26.58[b]	14.20[b]	12.38[b]
Mixed vegetation (MV)	21.14[b]	9.04[b]	12.10[b]
Agricultural land (AL)	19.81[b]	10.76[b]	9.06[b]

*Values with the same letter indicate no significant difference

*Analyzed and evaluated using the 0.05 level Duncan Multiple Range Test (DMRT) ($p<0.05$)

4. CONCLUSION

The study explored the CO_2 evolution of different peat ecotypes and biochar applications to test if biochar can inhibit the decomposition and release of CO_2. Results revealed that TMLB (37.42 mg/g) rendered the highest cumulative CO_2 evolved, followed by TPFB (26.58 mg/g), TMVB (21.14 mg/g), and TALB (19.81 mg/g), comparing it to treatments without biochar (ML=33.64 mg/g; PF=14.20 mg/g; AL=10.76 mg/g; and MV=9.04 mg/g). This study implies that biochar accelerates CO_2 evolution, and treatments without biochar application render CO_2 less evolved. Moreover, TPF (79.83%) and TML (77.51%) rendered the highest weight loss percentage. The same ecotypes rendered the highest weight loss percentage with biochar application (TMLB=67.19%; TPFB=62.89%). These results are essential in comprehending peatland ecosystems' decomposition and carbon dynamics. Further, one of the novel elements of this research is the emphasis on applying biochar in peat soil. Previous biochar and soil carbon sequestration research has primarily concentrated on agricultural soils or other non-peat ecosystems. It has shown that biochar has the potential to sequester carbon in other ecosystems, but explicitly in peatlands. This study further suggests that long incubation time, field study application, and exploring different biochar compositions should be studied to understand its decomposition dynamics when applied to peat. Thus, its effectiveness in mitigating greenhouse gas emissions and carbon sequestration in peat soils is relatively uncertain.

ACKNOWLEDGEMENTS

The authors would like to thank the faculty of the Department of Natural Science, College of Arts and Sciences, Eastern Visayas State University, Tacloban City, Philippines, for assisting during the laboratory and experimental work.

AUTHOR CONTRIBUTIONS

Bobon-Carnice, P.A.B.: Supervision, Conceptualization, Investigation, Methodology, Experiment, Validation, Formal Analysis, Visualization, Writing - Revise and Editing. Socias, G.N.: Supervision, Investigation, Methodology, Experiment, Validation, Formal Analysis, Visualization. Corcilles, M.Y.S.: Conceptualization, Investigation, Experiment, Visualization, Formal Analysis, Writing - Original Draft. Abaño, T.K.B.: Conceptualization, Investigation, Methodology, Experiment, Formal Analysis. Espanta, U.M.H.: Conceptualization, Investigation, Methodology, Experiment, Visualization.

DECLARATION OF COMPETING INTEREST

The authors declare that they have no known competing financial interests or personal relationships that could have appeared to influence the work reported in this paper.

REFERENCES

Abro SA, Tian XH, You DH, Wang XD. Emission of carbon dioxide influenced by nitrogen and water levels from soil incubated straw. Plant, Soil and Environment 2011;57(6):295-300.

Ajema L. Effects of biochar application on beneficial soil organism. International Journal of Research Studies in Science, Engineering and Technology 2018;5(5):9-18.

Alibo VLB, Lasco RD. Carbon storage of Caimpugan Peatland in Agusan Marsh, Philippines and its role in greenhouse gas mitigation. Journal of Environmental Science and Management 2012;15(2):50-8.

Amalina F, Abd Razak AS, Krishnan S, Sulaiman H, Zularisam AW, Nasrullah M. Biochar production techniques utilizing biomass waste-derived materials and environmental applications: A review. Journal of Hazardous Materials Advances 2022;7:Article No. 100134.

Anderson JP. Soil respiration. In: Methods of Soil Analysis Part 2, 2nd ed. Agronomy Monograph, ASA and SSSA, Madison; 1982. p. 831-71.

Angın D. Effect of pyrolysis temperature and heating rate on biochar obtained from pyrolysis of safflower seed press cake. Bioresource Technology 2013;128:593-7.

Azzi ES, Li H, Cederlund H, Karltun E, Sundberg C. Modelling biochar long-term carbon storage in soil with harmonized analysis of decomposition data. Geoderma 2024;441:Article No. 116761.

Bobon-Carnice PA, Chanton JP, Migo VP, Faustino-Eslava DV. Carbon storage of Leyte Sab-A Basin Peatland, Philippines. Environment and Natural Resources Journal 2023;21(5): 402-16.

Bobon-Carnice PA. Attenuation of amoeba in biocharamended clayey and sandy soil. IAMURE International Journal of Ecology and Conservation 2014;11(1):69-86.

Cai JF, Jiang F, Liu XS, Sun K, Wang W, Zhang MX, et al. Biochar-amended coastal wetland soil enhances growth of *Suaeda salsa* and alters rhizosphere soil nutrients and microbial communities. Science of the Total Environment 2021;788:Article No. 147707.

Chagas JK, de Figueiredo CC, Ramos ML. Biochar increases soil carbon pools: Evidence from a global meta-analysis. Journal of Environmental Management 2022;305:Article No. 114403.

Cheng H, Jones DL, Hill P, Bastami MS, Tu CL. Influence of biochar produced from different pyrolysis temperature on nutrient retention and leaching. Archives of Agronomy and Soil Science 2018;64(6):850-9.

Dargie GC, del Aguila-Pasquel J, Córdova Oroche CJ, Irarica Pacaya J, Reyna Huaymacari J, Baker TR, et al. Net primary productivity and litter decomposition rates in two distinct Amazonian peatlands. Global Change Biology 2024; 30(8):e17436.

de Jong AE, Guererro-Cruz S, van Diggelen JM, Vaksmaa A, Lamers LP, Jetten MS, et al. Changes in microbial community composition, activity, and greenhouse gas production upon inundation of drained iron-rich peat soils. Soil Biology and Biochemistry 2020;149:Article No. 107862.

Deshoux M, Sadet-Bourgeteau S, Gentil S, Prévost-Bouré NC. Effects of biochar on soil microbial communities: A meta-analysis. Science of the Total Environment 2023;902:Article No. 166079.

Du Y, Pei W, Zhou H, Li J, Wang Y, Chen K. Net ecosystem exchange of carbon dioxide fluxes and its driving mechanism in the forests on the Tibetan Plateau. Biochemical Systematics and Ecology 2022;103:Article No. 104451.

Giweta M. Role of litter production and its decomposition, and factors affecting the processes in a tropical forest ecosystem: A review. Journal of Ecology and Environment 2020;44(1):1-9.

Hermans R, McKenzie R, Andersen R, Teh YA, Cowie N, Subke JA. Net soil carbon balance in afforested peatlands and separating autotrophic and heterotrophic soil CO_2 effluxes. Biogeosciences 2022;19(2):313-27.

Hogg EH, Lieffers VJ, Wein RW. Potential carbon losses from peat profiles: Effects of temperature, drought cycles, and fire. Ecological Applications 1992;2(3):298-306.

Hossain MB, Rahman MM, Biswas JC, Miah MM, Akhter S, Maniruzzaman M, et al. Carbon mineralization and carbon dioxide emission from organic matter added soil under different temperature regimes. International Journal of Recycling of Organic Waste in Agriculture 2017;6:311-9.

Hou R, Li T, Fu Q, Liu D, Li M, Zhou Z, et al. Effects of biochar and straw on greenhouse gas emission and its response mechanism in seasonally frozen farmland ecosystems. Catena 2020;194:Article No. 104735.

Hua L, Lu Z, Ma H, Jin S. Effect of biochar on carbon dioxide release, organic carbon accumulation, and aggregation of soil. Environmental Progress and Sustainable Energy 2014; 33(3):941-6.

Humpenöder F, Karstens K, Lotze-Campen H, Leifeld J, Menichetti L, Barthelmes A, et al. Peatland protection and restoration are key for climate change mitigation. Environmental Research Letters 2020;15(10):Article No. 104093.

Jackson RB, Lajtha K, Crow SE, Hugelius G, Kramer MG, Piñeiro G. The ecology of soil carbon: Pools, vulnerabilities, and biotic and abiotic controls. Annual Review of Ecology, Evolution, and Systematics 2017;48(1):419-45.

Jayasekara C, Leigh C, Shimeta J, Silvester E, Grover S. Organic matter decomposition in mountain peatlands: Effects of substrate quality and peatland degradation. Plant and Soil 2024. DOI: https://doi.org/10.1007/s11104-024-06725-4.

Jenkinson DS, Powlson DS. The effects of biocidal treatments on metabolism in soil: I. Fumigation with chloroform. Soil Biology and Biochemistry 1976;8(3):167-77.

Jennings PA, Mullen CA, Roy M. Titration and pH measurement. In: Encyclopedia of Life Sciences (ELS). Chichester: John Wiley and Sons, Ltd; 2010.

Jian S, Li J, Wang G, Kluber LA, Schadt CW, Liang J, et al. Multi-year incubation experiments boost confidence in model projections of long-term soil carbon dynamics. Nature Communications 2020;11(1):Article No. 5864.

Jiang X, Denef K, Stewart CE, Cotrufo MF. Controls and dynamics of biochar decomposition and soil microbial abundance, composition, and carbon use efficiency during long-term biochar-amended soil incubations. Biology and Fertility of Soils 2016;52:1-14.

Jiang W, Xiong M, Shuzhen ZO, Di KA. Microbial genes for degrading plant-derived carbon are the key factors affecting soil respiration and temperature sensitivity in plateau peatlands. Pedosphere 2024;34(6):1026-37.

Jien SH, Wang CC, Lee CH, Lee TY. Stabilization of organic matter by biochar application in compost-amended soils with contrasting pH values and textures. Sustainability 2015;7(10):13317-33.

Jones DL, Rousk J, Edwards-Jones G, DeLuca TH, Murphy DV. Biochar-mediated changes in soil quality and plant growth in a three year field trial. Soil Biology and Biochemistry 2012;45:113-24.

Joosten HA. Peatlands across the globe. In: Peatland Restoration and Ecosystem Services: Science, Policy and Practice. Cambridge University Press Ebooks; 2016. p. 19-43.

Kaur S, Babbar D, Sarif O, Ghatak A, Jaafari A. Assessment of carbon sequestration using InVEST model in Delhi, India. In: Conservation, Management and Monitoring of Forest Resources in India. Cham: Springer International Publishing; 2022 p. 33-56.

Keith A, Singh B, Singh BP. Interactive priming of biochar and labile organic matter mineralization in a smectite-rich soil. Environmental Science and Technology 2011;45(22):9611-8.

Lin X, Wang N, Li F, Yan B, Pan J, Jiang S, et al. Evaluation of the synergistic effects of biochar and biogas residue on CO_2 and CH_4 emission, functional genes, and enzyme activity during straw composting. Bioresource Technology 2022; 360:Article No. 127608.

Lu W, Ding W, Zhang J, Li Y, Luo J, Bolan N, et al. Biochar suppressed the decomposition of organic carbon in a cultivated sandy loam soil: A negative priming effect. Soil Biology and Biochemistry 2014;76:12-21.

Lu X, Vitousek PM, Mao Q, Gilliam FS, Luo Y, Turner BL, et al. Nitrogen deposition accelerates soil carbon sequestration in tropical forests. Proceedings of the National Academy of Sciences 2021;118(16):e2020790118.

Mosa A, Mansour MM, Soliman E, El-Ghamry A, El Alfy M, El Kenawy AM. Biochar as a soil amendment for restraining greenhouse gases emission and improving soil carbon sink: Current situation and ways forward. Sustainability 2023;15(2):Article No. 1206.

Mitsch WJ, Bernal B, Nahlik AM, Mander Ü, Zhang L, Anderson CJ, et al. Wetlands, carbon, and climate change. Landscape Ecology 2013;28:583-97.

Nikonova L, Kurganova I, Lopes de Gerenyu V, Rogova O, Golovatskaya E. Impact of temperature and moisture on the decomposition of peat-forming plants: Results of a two-year incubation experiment. Forests 2023;14(12):Article No. 2355.

Protected Areas and Wildlife Bureau Department of Natural Resources (PAWB-DENR). The National Wetlands Action Plan for the Philippines 2011-2016. Philippines: National Wetlands Action Plan for the Philippines (NWAPP); 2013.

Qambrani NA, Rahman MM, Won S, Shim S, Ra C. Biochar properties and eco-friendly applications for climate change mitigation, waste management, and wastewater treatment: A review. Renewable and Sustainable Energy Reviews 2017;79:255-73.

Rahman L, Whitelaw-Weckert MA, Orchard B. Impact of organic soil amendments, including poultry-litter biochar, on nematodes in a Riverina, New South Wales, vineyard. Soil Research 2014;52(6):604-19.

Rawat J, Saxena J, Sanwal P. Biochar: A sustainable approach for improving plant growth and soil properties. In: Biochar - An Imperative Amendment for Soil and the Environment. Intech Open; 2019. p. 1-17.

Rankin TE, Roulet NT, Moore TR. Controls on autotrophic and heterotrophic respiration in an ombrotrophic bog. Biogeosciences 2022;19(13):3285-303.

Ritter S, Paniagua P, Hansen CB, Cornelissen G. Biochar amendment for improved and more sustainable peat stabilisation. Proceedings of the Institution of Civil Engineers-Ground Improvement 2022;177(2):129-40.

Rogovska N, Laird D, Cruse R, Fleming P, Parkin T, Meek D. Impact of biochar on manure carbon stabilization and greenhouse gas emissions. Soil Science Society of America Journal 2011;75(3):871-9.

Rubin RL, Anderson TR, Ballantine KA. Biochar simultaneously reduces nutrient leaching and greenhouse gas emissions in restored wetland soils. Wetlands 2020;40(6):1981-91.

Shen X, Jiang M, Lu X, Liu X, Liu B, Zhang J, et al. Aboveground biomass and its spatial distribution pattern of herbaceous marsh vegetation in China. Science China Earth Sciences 2021;64(7):1115-25.

Sovova S, Enev V, Smilek J, Kubikova L, Trudičová M, Hajzler J, et al. The effect of biochar application on soil properties and growth of the model plant Zea mays. Ecocycles 2021;7(2):46-54.

Söderqvist H. Carbon Stability of Biochar: Methods for Assessment and Indication [dissertation]. Sweden: KTH Royal Institute of Technology, Stockholm; 2019.

Tang J, Bradford MA, Carey J, Crowther TW, Machmuller MB, Mohan JE, et al. Temperature sensitivity of soil carbon. In: Mohan JE, editor. Ecosystem Consequences of Soil Warming: Microbes, Vegetation, Fauna and Soil Biogeochemistry. London, United Kingdom: Academic Press; 2019. p. 75-208.

Tomczyk A, Sokołowska Z, Boguta P. Biochar physicochemical properties: Pyrolysis temperature and feedstock kind effects. Reviews in Environmental Science and Bio/Technology 2020;19(1):191-215.

Troy SM, Lawlor PG, O'Flynn CJ, Healy MG. Impact of biochar addition to soil on greenhouse gas emissions following pig manure application. Soil Biology and Biochemistry 2013; 60:173-81.

Vandecasteele B. Oxygen uptake rate versus CO_2 based respiration rate for assessment of the biological stability of peat, plant fibers and woody materials with high C:N ratio versus composts. Waste Management 2023;167:74-80.

Wang K, Wang S, Zhang X, Wang W, Wang X, Kong F, et al. The amelioration and improvement effects of modified biochar derived from *Spartina alterniflora* on coastal wetland soil and Suaeda salsa growth. Environmental Research 2024; 240:Article No. 117426.

Weber K, Quicker P. Properties of biochar. Fuel 2018;217:240-61.

Xiang Y, Liu Y, Niazi NK, Bolan N, Zhao L, Zhang S, et al. Biochar addition increased soil bacterial diversity and richness: Large-scale evidence of field experiments. Science of the Total Environment 2023;893:Article No. 164961.

Yao H, Peng H, Hong B, Guo Q, Ding H, Hong Y, et al. Environmental controls on multi-scale dynamics of net carbon dioxide exchange from an alpine peatland on the eastern Qinghai-Tibet Plateau. Frontiers in Plant Science 2022;12:Article No. 791343.

Zhao C, Liu B, Piao S, Wang X, Lobell DB, Huang Y, et al. Temperature increase reduces global yields of major crops in four independent estimates. Proceedings of the National Academy of Sciences 2017;114(35):9326-31.

Zhou Y, Li D, Li Z, Guo S, Chen Z, Wu L, et al. Greenhouse gas emissions from soils amended with cornstalk biochar at different addition Ratios. International Journal of Environmental Research and Public Health 2023;20(2):Article No. 927.

Environment and Natural Resources Journal

Volume 23
Issue 2
2025

Nexus between Livelihood Strategies and Food Security Status in Landslide-prone Areas of the Gammo Highlands, South Ethiopia: A Quantitative Analysis

Lemma Tadesse*, Abera Uncha, and Thomas Toma

Arba Minch University, Department of Geography and Environmental Studies, Ethiopia

ARTICLE INFO

Received: 18 Jul 2024
Received in revised: 5 Dec 2024
Accepted: 16 Dec 2024
Published online: 27 Feb 2025
DOI: 10.32526/ennrj/23/20240204

Keywords:
Food security/ Gamo zone/ Livelihood strategies/ South Ethiopia

*** Corresponding author:**
E-mail:
tadesse_lemma@yahoo.com

ABSTRACT

Investigating the relationship between various livelihood strategies and food security status is crucial to understanding how different economic activities impact access to food security. This study explores the relationship between multiple livelihood strategies and the food security status among rural households vulnerable to landslide hazards in the Gacho Baba District of the Gammo Highlands South Ethiopia. Data were collected from 289 statistically selected sample households in the district employing multistage sampling techniques. Questionnaires assessed the demographic, socioeconomic, and food security-related data. Meanwhile, livelihood strategies were categorized based on on-farm, off-farm, and non-farm activities. Food security status was assessed using the Household Food Insecurity Access Scale (HFIAS), Food Consumption Score (FCS), and Reduced Coping Strategies Index (RCSI). Pearson correlation and one-way Multivariate Analysis of Variance (MANOVA) were inferential statistical tools used for data analysis. The Pearson correlation analysis revealed significant negative associations between livelihood strategies and food insecurity indicators. This suggests that diversifying livelihood activities is the best way to lower levels of food insecurity. Furthermore, the MANOVA results underscored the substantial impact of livelihood strategies on food security outcomes, underscoring the pivotal role of livelihood diversification in bolstering food security. Post hoc comparisons underscored the benefits of combining on-farm, off-farm, and non-farm activities for improved food security outcomes. The findings emphasize the need for targeted interventions promoting livelihood diversification to mitigate food insecurity risks among vulnerable rural households. Further research is warranted to explore underlying mechanisms and develop tailored strategies addressing multifaceted challenges in accessing nutritious food.

1. INTRODUCTION

The global dialogue surrounding food security emphasizes the critical need to comprehend the relationship between livelihood strategies and food security (FAO, 2023). With millions worldwide grappling with hunger and malnutrition, food security remains a pressing concern (Agostoni et al., 2023; Balehegn et al., 2020). Livelihood strategies, spanning various activities from agricultural practices to off-farm employment opportunities, significantly influence households' ability to obtain food resources (Fitzpatrick et al., 2019). Nevertheless, environmental hazards like landslides present formidable obstacles to food production and distribution, exacerbating food insecurity worldwide (Adu-Baffour et al., 2021).

In Africa, where a significant portion of the population relies on agriculture for livelihood and sustenance, the nexus between livelihood strategies

Citation: Tadesse L, Uncha A, Toma T. Nexus between livelihood strategies and food security status in landslide prone areas of Gamo Highlands, South Ethiopia: A quantitative analysis. Environ. Nat. Resour. J. 2025;23(2):118-131. (https://doi.org/10.32526/ennrj/23/20240204)

and food security assumes heightened importance (Asiedu et al., 2017). Subsistence farming remains prevalent, particularly in rural areas, where smallholder farmers face myriad challenges, including land degradation, erratic rainfall, and limited access to inputs and markets (FAO, 2022). Consequently, food insecurity is pervasive across the continent, with millions grappling with hunger and malnutrition (Alexander et al., 2016).

Within Sub-Saharan Africa, environmental vulnerabilities further compound the challenges of food security (Pawlak and Kolodziejczak, 2020). Landslides, triggered by factors such as deforestation and heavy rainfall, pose a significant threat to livelihoods and food production (Kurnia and Hizbaron, 2020). In countries like Ethiopia, where rugged terrain and climatic variability are prevalent, landslide-prone areas pose unique challenges to food production and distribution (Anderson et al., 2021). Against this backdrop, exploring the interplay between livelihood strategies and food security status has added significance as policymakers and practitioners seek sustainable solutions to address hunger and poverty (Kassegn and Endris, 2021). Understanding how different livelihood strategies affect food security among rural households is crucial for developing effective interventions to enhance food security in these vulnerable communities (USAID, 2022).

In southern Ethiopia, the Gamo Zone is characterized by its diverse topography, ranging from fertile valleys to steep mountain slopes (Yirgu, 2022; Amejo, 2018; Assefa and Bork, 2016). However, this scenic landscape belies the challenges communities face, particularly in areas prone to landslides (Shano et al., 2021). The Gacho Baba district, nestled within the Gamo Zone, exemplifies the complex dynamics, where households struggle with environmental hazards while striving to secure their livelihoods and food security (Cholo et al., 2019). Agriculture serves as the primary livelihood source, but the sustainability of farming practices is threatened by different natural hazards, particularly landslides (Tadesse et al., 2024b). Hence, understanding how livelihood strategies interconnect with food security is paramount in addressing the ongoing crisis regarding food security (Kassegn and Endris, 2021). Therefore, this study investigated the connection between livelihood strategies and food security status. Specifically, (1) to investigate the correlation between households' livelihood strategies and their food security status, (2) to analyze the effect of specific livelihood strategies on household food security status of rural households in the Gacho Baba district of Gamo Highlands South Ethiopia.

2. METHODOLOGY

2.1 Description of the study area

Gach-Baba District, placed within the Gamo Zone of the South Ethiopia Regional State, encompasses the Gamo Highlands. Astronomically, it spans between 5°38'30" and 6°10'50" N latitude and 37°20'30" and 37°31'30" E longitude (Figure 1). The district comprises 11 rural villages: Gatse, Koddo, Wusamo, Merche, Tsayite, Zegiti Bakole, Gerbenssa-Tsenkile, Kuyile, Laka, Zegiti Feriso, and Mazo-Doyisa. Physically, the terrain of the study area is characterized by undulating features that predispose it to various natural hazards. Its topography mainly consists of hills, reaching a maximum elevation of 3,493 meters above sea level, with a general decrease in elevation from west to east. The rugged topography of the Gamo Highlands divides the area into three distinct agroecological zones based on altitude: temperate (37%), cool (39%), and (24%) (Tadesse et al., 2024b).

While agriculture in this region is vulnerable to climate effects, it remains the primary means of sustenance, like many rural areas in Ethiopia, with weaving also being significant within Gamo communities. *Ensete ventricosum* (commonly known as *enset*), potatoes, and cereals, particularly barley, and wheat, form the cornerstone of livelihoods in this region (Massa and Mosa, 2021). However, productivity is hindered by small landholdings, land fragmentation, and poor soil fertility due to various human and natural hazards (Cholo et al., 2018). Consequently, livelihoods in recent times have shifted towards subsistence agriculture and some off-farm economic activities. According to the United Nations Office for the Coordination of Humanitarian Affairs (OCHA, 2021) the population of the Gach-Baba District totaled 101,786, with 51,088 males and 50,697 females. The population structure indicates a young dependency ratio (individuals under the age of 14) of 48.3% and an old dependency ratio (individuals over the age of 64) of 2.7%.

2.2 Methods, data types, and sampling

In the study, a quantitative research approach was utilized to gather and analyze data, a method commonly favored in food security and livelihood strategies studies for its usefulness following the

philosophical underpinnings of post-positivism (Dawadi et al., 2021; Wasti SP et al., 2022). Data were gathered from a statistically determined 289 sample of rural households vulnerable to landslide hazards (Table 1). Thus, the household served was used as the unit of analysis.

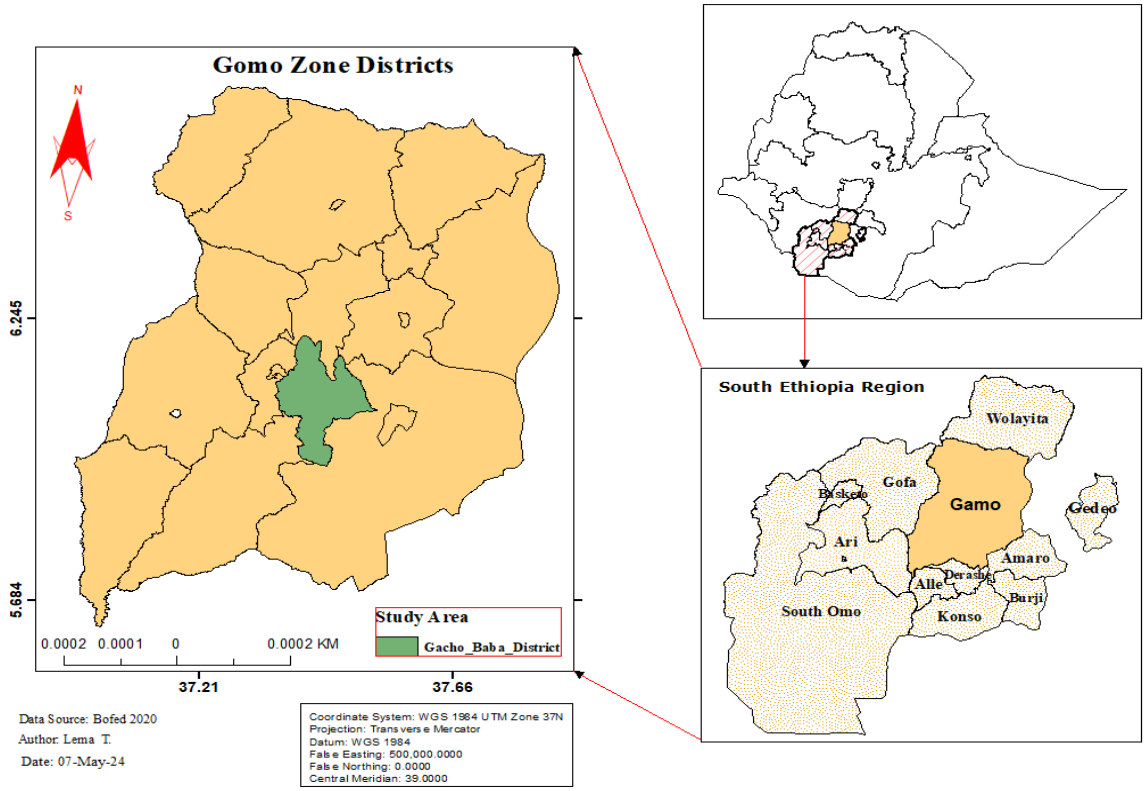

Figure 1. Locational map of the study area

Multistage sampling techniques were utilized, with the non-probability sampling method of purposive sampling being employed to select the study district and sample villages. The Gacho Baba District was purposively chosen due to the researchers' familiarity with its vulnerability to natural hazards. Moreover, the studies have aimed to investigate the linkage between livelihood strategies, and the food security status of rural households in landslide-prone areas. Five out of the 11 villages namely, Gatse, Kodo, Wusamo, Zigiti Merche, and Tsayite, were purposefully selected since these villages are repeatedly affected by landslide hazards negatively impacting livelihood strategies (Tadesse et al., 2024a). Only households in these five villages affected by landslides were included in the study population. After considering various options the required sample size 'n' and the total number of households studied 'N' were determined based on Yamane's (1967) formula, with a precision level (e) of 0.05 and a confidence level of 95% at p = ±5, assuming an existence probability of events as 1.

$$\text{Population, which is illustrated as } = \frac{N}{1+N(e^2)} \text{ Thus, } n = \frac{1{,}045}{1+1{,}045(0.05^2)} = 289 \text{ households} \quad (1)$$

A list of all households' sample frames (N) in each of the five villages was obtained from the records of local administration offices. To ensure gender balance, female and male-headed households were selected using systematic random sampling techniques based on their availability to maintain the proportionality of the sample size. As indicated in Equation 1 the total population list or sample frame becomes 1,045 household heads who had experienced frequent landslide hazards. Consequently, the sample size for each village was selected proportionally using systematic probability sampling techniques (Table 1). As a result, the sample size (n) became 289 household heads.

Table 1. Distribution of the target population, sample, and sampling techniques

No.	Villages (Purposive sampling)	Total HH venerable to landslides hazard (purposive sampling)			Sample HH (Proportional systematic sampling)			Percentage
		M	F	Total	M	F	Total	
1	Gatse	266	1	267	73	1	74	26
2	Kodo	217	3	220	58	3	61	21
3	Wusamo	200	0	200	55	0	55	19
4	Zegiti Merch	199	1	200	54	1	55	19
5	Tsayite	154	4	158	40	4	44	15
Total		1,036	9	1,045	280	9	289	100

To make the process effective, 20 data collectors (5 for each village, but the length of dates of data collection differ based on sample size) and, 5 facilitators (1 for each village) who are properly trained on how to approach respondents and handle the entire data together with the researcher was engaging in the data collection process.

2.3 Instruments of data collection

Questioners composed of closed-ended and open-ended types were this research's primary data collection tools. The questionnaires covered various issues including demographic and socio-economic characteristics of respondents, livelihood strategies, and issues related to food security. Questions related to food security relied on food in/security measurement scores, particularly the Household Food Security Access Scale (HFIAS), the Food Consumption Scale (FCS), and the Reduced Copping Strategies Index (RCSI), obtained from the (Kini, 2022; WFP, 2016; WFP, 2008; USDA, 2000). These are advocated for their quick, precise, and cross-contextual indication of food security (Yenesew and Masresha, 2019).

The questionnaires related to livelihood strategies were also composed of both close-ended and open-ended types of questions that covered various issues regarding livelihood strategies, and related issues. Questions were adapted and developed after reviewing different literature. Before data collection began, the questionnaire was first tested in a pilot study conducted in the rural village of Zegiti-Bakole where actual data collection was not conducted but in similar situations. The objective of the pilot study was to confirm the questionnaires' dependability/internal consistency using Cronbach's alpha to assess the degree to which each item connected with the survey's overall results. It showed the dependability to be 86% for the survey items examining types of livelihood strategies used. Thus, the examination performance of the items verified the validity of the instruments since statistical literature suggests a reliability of 70% and higher for basic research (Haji-Othman et al., 2021; Nunnally, 1978).

2.4 Methods of data analysis

The analysis of this study began with the application of Pearson correlation to examine the relationship between livelihood strategies and various household food security indicators, including HFIAS, FCS, and RCSI. The Pearson correlation coefficient is instrumental in identifying potential associations between variables (Schober et al., 2018). In this context, using Pearson correlation to measure the correlations between household livelihood strategies and food security status is crucial. It quantifies the strength and direction of linear relationships between variables, offering valuable insights into how changes in one variable may be associated with changes in another. According to Nunnally (1978), the Pearson r can be calculated as the mean of the sum of the product of z-scores, mathematically described as:

$$\gamma = \frac{1}{n-1} \sum_{i=1}^{n} \left(\frac{X_i - \bar{X}}{S_X}\right)\left(\frac{Y_i - \bar{Y}}{S_Y}\right) \quad (2)$$

Following these steps, the Pearson correlation coefficient indicates the strength and direction of the linear relationship between the two variables X and Y. The value of r ranges from (-1 to 1), where; r=1 indicates a perfect positive linear relationship, r=-1 indicates a perfect negative linear relationship, and r=0 indicates no linear relationship.

After the correlation analysis, the study proceeded to delve deeper into the examination of the effect of livelihood strategies on households' overall food security status through the utilization of one-way MANOVA (Multivariate Analysis of Variance). With the presence of single with multiple independent

variables (livelihood strategies) and multiple dependent variables (comprising the food security indicators, HFIAS, FCS, and RCSI), for these types of variables, one-way MANOVA emerged as an apt statistical tool (Sadik and Alwan, 2020). Because one-way MANOV facilitated a comprehensive assessment of potential differences in the combined set of dependent variables, reflective of overall food security status, across varying levels of the independent variable distinct livelihood strategies (Khamis and El-Refae, 2020). Therefore the study used one-way MANOVA to find how different livelihood strategies were connected to overall household food security in the study area. To sum up, the study used Pearson correlation and one-way MANOVA to thoroughly understand how different ways households make a living affect their overall food security. By applying these statistical methods, the research finds potential connections and identifies important differences in food security among various livelihood strategies.

3. RESULTS

3.1 Households' livelihood strategies and food security status

Data on households' livelihood strategies were collected using 18 items, which were categorized into on-farm, off-farm, and non-farm activities. The survey findings revealed that the farming households employed a variety of strategies to support their livelihoods (Figure 2). A significant majority of the households, 56% or 163 households, relied exclusively on on-farm activities. These households depended solely on agricultural activities for their income and sustenance, highlighting a strong reliance on traditional farming methods. Another group, comprising 13% of the households, combined on-farm and off-farm activities. These households diversified their income sources by engaging in both agricultural work and supplementary off-farm activities, which might include local employment or other forms of labor outside their farms. Additionally, 12% of the households engaged in both on-farm and non-farm activities.

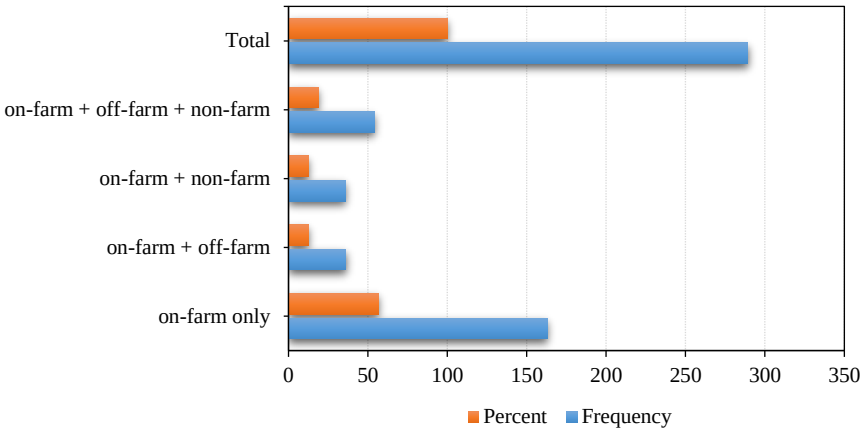

Figure 2. Percentages of household livelihood strategies choice (N=289)

This combination indicates a strategy where households not only rely on farming but also involve themselves in non-agricultural businesses or services, providing a broader base for economic stability. Finally, 19% of the households adopted a holistic approach by incorporating on-farm, off-farm, and non-farm activities. These households utilized a comprehensive strategy to sustain their livelihoods, balancing agricultural work with various other income-generating activities. These findings illustrate the diverse strategies farming households use to support their livelihoods, reflecting their adaptability and resourcefulness in managing economic challenges.

Regarding the food security status of households, data was collected using three food insecurity indicator scales: the Household Food Insecurity Access Scale (HFIAS), the Food Consumption Scores (FCS), and the Reduced Coping Strategies Index (RCSI). The results were presented as follows: The findings from the HFIAS shed light on the varied food security challenges of vulnerable households. Among the households surveyed, a considerable number faced some level of food insecurity. Specifically, 38% of households were food secure, while 12% experienced mild food insecurity. Furthermore, 34% of households were moderately food insecure, and 16% were classified as severely food insecure. These statistics highlight the critical need for targeted interventions to address vulnerable

groups' unique needs and mitigate the adverse effects of food insecurity within communities (Figure 3).

The investigation of food consumption scores (FCS) among households also delineates distinct consumption categories, shedding light on the dietary patterns within the surveyed households (Figure 4). Among the households, 51.3% were classified as "Poor" in terms of food consumption, indicating significant limitations in accessing adequate and diverse food sources. Another 34.9% fell into the "Borderline" category, suggesting precarious food access and potential vulnerability to food insecurity.

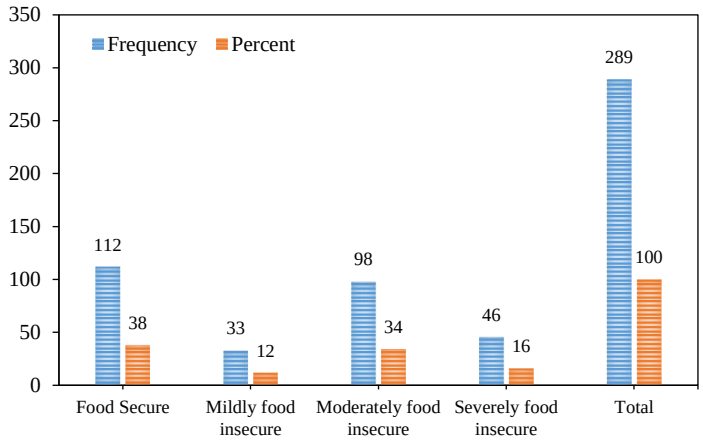

Figure 3. Households' food in/security status (HFIAS) based categorization scheme

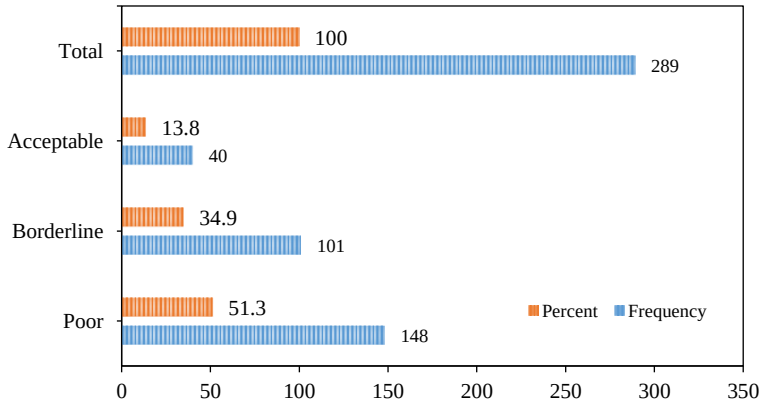

Figure 4. Food consumption score based on food consumption groups of the households

Conversely, 13.8% of households were deemed to have "Acceptable" food consumption levels. These findings underscore the heterogeneous nature of food access and consumption within the community, emphasizing the urgency of targeted interventions to address food insecurity and improve dietary diversity among vulnerable households.

The analysis of consumption coping strategies, measured by the Reduced Coping Strategies Index (RCSI) and its associated severity weights, provides valuable insights into the adaptive mechanisms employed by households facing food insecurity (Figure 5). The severity weights for RCSI were categorized into three levels: low coping (CSI 0-3), medium coping (CSI=4-9), and high coping (CSI≥10). Among the surveyed households, 15.6% exhibited low coping strategies, indicating a relatively lower degree of reliance on coping mechanisms to address food insecurity. In contrast, a larger proportion, constituting 31.1% of households, adopted medium coping strategies, signifying a moderate reliance on coping mechanisms to manage food shortages. Remarkably, the majority of households, comprising 53.3%, demonstrated high coping strategies, indicative of a significant dependence on coping mechanisms to endure severe food insecurity. These findings underscore the adaptive resilience of households in the face of food insecurity challenges, while also highlighting the pressing need for comprehensive interventions to alleviate the underlying causes of food insecurity and reduce households' reliance on coping mechanisms.

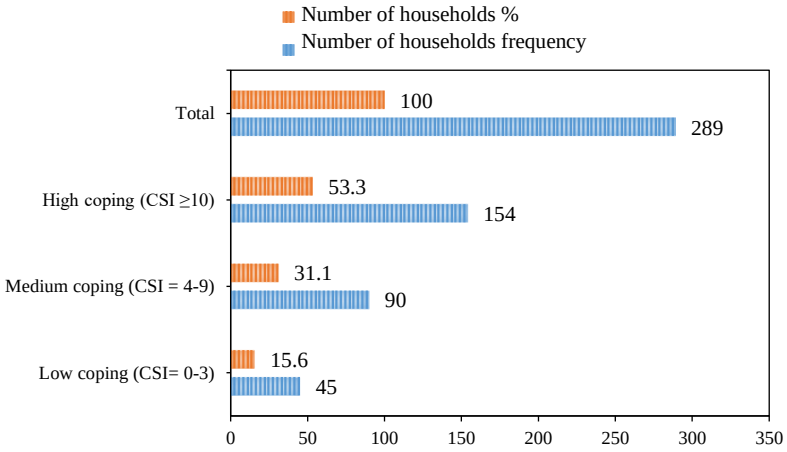

Figure 5. Consumption coping strategies and associated severity weight for RCSI

4. DISCUSSION

4.1 Correlation between households' livelihood strategies and their food security status

In this study, Pearson correlation was utilized to identify whether certain livelihood practices were positively or negatively correlated with food security indicators. Thus, Pearson correlation aids in detecting potential trends and patterns within the data verifying all assumptions, including continuous variables, a linear relationship between variables, the absence of significant outliers, and approximate normal distribution.

As shown in Table 2 the correlation analysis between households' livelihood strategies and food security measures (HFIAS, FCS, and RCSI) revealed significant associations. Households' Livelihood Strategies exhibited a strong negative correlation with HFIAS (r=-0.598, p<0.01), indicating that as Livelihood Strategies increase, the severity of food insecurity access decreases. The result aligns with prior findings (Tadesse et al., 2022; Asfaw et al., 2017) indicating that as livelihood strategies diversify, the severity of food insecurity access decreases. The finding possibly reaffirms the notion that diversified livelihoods are crucial in alleviating food insecurity challenges.

Table 2. Correlations between household's livelihood strategies and food security status

Correlations					
Household livelihood strategies vs food security status		LS	HFIAS	FCS	RCSI
Households livelihood strategies	Pearson correlation	1	-0.598**	0.413**	-0.395**
	Sig. (2-tailed)		0.000	0.000	0.000
	N	289	289	289	289
HFIAS	Pearson correlation	**-0.598****	1	-0.613**	**0.689****
	Sig. (2-tailed)	0.000		0.000	0.000
	N	289	289	289	289
FCS	Pearson correlation	**0.413****	**-0.613****	1	**-0.625****
	Sig. (2-tailed)	0.000	0.000		0.000
	N	289	289	289	289
RCSI	Pearson correlation	-0.395**	0.689**	-0.625**	1
	Sig. (2-tailed)	0.000	0.000	0.000	
	N	289	289	289	289

**Correlation is significant at the 0.01 level (2-tailed).

Additionally, a moderate positive correlation was observed between Livelihood Strategies and FCS (r=0.413, p<0.01), suggesting that households with more diverse livelihood strategies tend to have better food consumption scores. Furthermore, significant negative correlations were found between HFIAS and both FCS (r=-0.613, p<0.01) and RCSI (r=-0.689, p<0.01), indicating that higher levels of food

insecurity access are associated with lower food consumption scores and increased reliance on coping strategies. The moderate positive correlation between livelihood strategies and FCS corroborates earlier research (Giannini et al., 2021) suggesting that households with more diverse livelihood strategies tend to have better food consumption scores. Similarly, the significant negative correlations between HFIAS and both FCS reinforce the understanding that higher levels of food insecurity access are associated with lower food consumption scores and increased reliance on coping strategies, consistent with prior findings (Mekonnen and Gerber, 2017).

Moreover, a significant negative correlation was observed between FCS and RCSI ($r=-0.625$, $p<0.01$), implying that households with better food consumption scores tend to have a lower reliance on coping strategies. The observed negative correlation between FCS and RCSI supports previous research (Almukaddem et al., 2022) indicating that households with better food consumption scores typically have lower reliance on coping strategies. Overall, these findings add to the body of evidence highlighting the intricate relationship between livelihood strategies and various dimensions of food security and underscore the importance of implementing targeted interventions aimed at promoting diversified livelihoods to enhance food security outcomes for vulnerable households.

4.2 The effect of livelihood strategies on the food security status of rural households

One-way Multivariate Analysis of Variance (MANOVA) serves as a crucial statistical tool for investigating the impact of livelihood strategies on the households' food security status (Sadik and Alwan, 2020). simultaneously analyzing multiple dependent variables, such as food insecurity access, consumption patterns, and coping strategies, MANOVA enables a comprehensive assessment of the complex dynamics underlying household food security in rural settings (Finch, 2022; Shone et al., 2017). Moreover, MANOVA's ability to account for correlations between dependent variables and identify multivariate patterns allows for a more nuanced understanding of the relationship between livelihood strategies and food security, thereby guiding efforts to enhance the well-being of rural communities facing food insecurity challenges (Khamis and El-Refae, 2020).

Firstly, as shown in Table 3 the summary of the one-way MANOVA model was run to cheeks the assumption, and the output provides valuable insights into the overall significance of the Intercept and LS (Households Livelihood Strategies) which are independent variable effects on the food security indicators which are dependent variables. The multivariate tests, including Pillai's Trace, Wilks' Lambda, Hotelling's Trace, and Roy's Largest Root, offer comprehensive assessments of the relationships between the independent and dependent variables. As the result revealed for the Intercept effect, all multivariate test statistics exhibit extremely low p-values (Sig.=0.00), indicating highly significant effects. This suggests that there are significant differences between groups in terms of the combined dependent variables. The large values of Pillai's Trace, Hotelling's Trace, and Roy's Largest Root also further affirm the substantial effect of the intercept (Finch, 2022; Maposa et al., 2010).

Table 3. Model summary of one-way MANOVA (multivariate tests)

Multivariate tests						
Effect		Value	F	Hypothesis df	Error df	Sig.
Intercept	Pillai's Trace	0.952	1865.218[b]	3.000	283.000	0.000
	Wilks' Lambda	0.048	1865.218[b]	3.000	283.000	0.000
	Hotelling's Trace	19.773	1865.218[b]	3.000	283.000	0.000
	Roy's Largest Root	19.773	1865.218[b]	3.000	283.000	0.000
LS	Pillai's Trace	0.526	20.200	9.000	855.000	0.000
	Wilks' Lambda	0.486	26.433	9.000	688.898	0.000
	Hotelling's Trace	1.034	32.365	9.000	845.000	0.000
	Roy's Largest Root	1.010	95.982[c]	3.000	285.000	0.000

[a]Design: Intercept + LS; [b]Exact statistic; [c]The statistic is an upper bound on F that yields a lower bound on the significance level.

Moving to the LS effect, again, all multivariate test statistics demonstrate highly significant results (Sig.=0.000). This implies that there are significant differences between groups regarding the dependent variables when considering the LS variable (Landler et al., 2022; Barnett, 2020). The values of Pillai's Trace, Wilks' Lambda, Hotelling's Trace, and Roy's Largest Root indicate the magnitude of the LS effect on the dependent variables (Ates et al., 2019; Brown, 2014; Tabachnick and Fidell, 2013). The design statement clarifies the composition of the model, indicating that both the intercept and LS variables are included in the analysis. The notation about exact statistics (b. Exact statistic) suggests that the reported values are precise rather than approximations. Furthermore, the note about Roy's Largest Root (c. The statistic is an upper bound on F that yields a lower bound on the significance level) provides additional context for interpreting this statistic, indicating its conservative estimate of significance (Sadik and Alwan, 2020; Maposa et al., 2010).

Overall, the results from the Multivariate Tests table confirm that both the intercept and LS variables have significant effects on the dependent variables. These findings underscore the importance of considering both the baseline (intercept) and the LS variable when analyzing the multivariate relationship between the independent and dependent variables. The highly significant results suggest that these effects are not due to random chance but reflect meaningful differences between groups in terms of the combined dependent variables.

Secondly, the analysis of the one-way MANOVA (Table 4) regarding the effect of livelihood strategies on the food security status of rural households reveals significant conclusions across multiple dependent variables. The tests of between-subjects effects indicate substantial impacts of livelihood strategies on household food security, as reflected in the Type III Sum of Squares and associated F-statistics. For the HFIAS, FCS, and RCSI, the Type III Sum of Squares values are notable, with corresponding F-statistics indicating highly significant effects ($p<0.001$). These results emphasize the importance of considering livelihood strategies in understanding variations in food security outcomes among rural households. The finding allied with the findings of (Landler et al., 2022) that endorse the higher R-squared indicates significant relationships between variables. In this regard, the higher R-squared values in this analysis that is 0.492 for HFIAS, 0.265 for FCS, and 0.268 for RCSI suggest that a substantial proportion of the variance in food security status can be attributed to differences in livelihood strategies. Additionally, the adjusted R-squared values provide further confirmation of the robustness of these relationships, indicating that the effects of livelihood strategies on food security remain significant even after adjusting for potential confounding factors. Overall, these findings highlight the critical importance of addressing livelihood strategies in developing interventions and policies aimed at enhancing food security and resilience among rural households.

Table 4. Summary of One-way MANOVA about the effect of livelihood strategies on the food security status of rural households

Tests of between-subjects effects						
Independent variable	Dependent variable	Type III sum of squares	df	Mean square	F	Sig.
Livelihood strategies	HFIAS	66.917	3	22.306	92.029	0.000
	FCS	49.777	3	16.592	34.264	0.000
	RCSI	52.457	3	17.486	34.854	0.000
a. R Squared=0.492 (Adjusted R squared=0.487)						
b. R Squared=0.265 (Adjusted R squared=0.257)						
c. R Squared=0.268 (Adjusted R squared=0.261)						

Finally, the post hoc comparisons following the one-way MANOVA (Table 5) analysis provide detailed insights into the specific differences in food security status among rural households based on their adopted livelihood strategies (Landler et al., 2018). Using the Bonferroni correction method, post hoc comparisons were conducted for variations in food security outcomes across different combinations of livelihood strategies and HFIAS, FCS, and RCSI scores (Table 5). The comparisons reveal significant mean differences between various combinations of livelihood strategies. Notably, households engaging in a combination of on-farm, off-farm, and non-farm activities consistently show the most favorable food

security outcomes across all three variables, with significantly lower HFIAS scores, higher FCS scores, and fewer RCSI employed compared to households with other livelihoods strategies. Conversely, households solely relying on on-farm activities tend to experience higher levels of food insecurity, lower food consumption scores, and more pronounced coping strategies, highlighting the potential benefits of livelihood diversification in improving food security among rural households, which is aligned with findings of (Tesema and Berhanu, 2018; FAO et al., 2014) revealing the positive impact of diversified income sources on household resilience and food security.

Moreover, the post hoc comparisons underscore the importance of considering the additive effects of different livelihood strategies on food security outcomes. Such as households combining on-farm and off-farm activities demonstrate significantly better food security indicators compared to those solely engaged in on-farm activities, indicating the potential synergistic benefits of diversifying livelihood sources. These findings align with (Kassegn and Endris, 2021) emphasizing the positive associations between livelihood diversification and food security, as diverse income streams can buffer households against agricultural shocks and income volatility, ultimately improving overall food access and dietary diversity.

Table 5. The post hoc comparison of One-way MANOVA about the effect of livelihood strategies on the food security status of rural households

Multiple comparisons							
Bonferroni							
Dependent variable	(I) Households livelihood strategies	(J) Households livelihood strategies	Mean difference (I-J)	Std. error	Sig.	95% Confidence interval	
						Lower bound	Upper bound
HFIAS	On-farm only	On-farm + off-farm	0.0198	0.09066	1.000	-0.2211	0.2607
		On-farm + non-farm	0.0723	0.09066	1.000	-0.1686	0.3131
		On-farm + off-farm + non-farm	1.2472*	0.07730	**0.000**	1.0418	1.4525
	On-farm + off-farm	On-farm only	-0.0198	0.09066	1.000	-0.2607	0.2211
		On-farm + non-farm	0.0525	0.11604	1.000	-0.2558	0.3608
		On-farm + off-farm + non-farm	1.2274*	0.10593	0.000	0.9459	1.5088
	On-farm + non-farm	On-farm only	-0.0723	0.09066	1.000	-0.3131	0.1686
		On-farm + off-farm	-0.0525	0.11604	1.000	-0.3608	0.2558
		On-farm + off-farm + non-farm	1.1749*	0.10593	**0.000**	0.8935	1.4563
	On-farm + off-farm + non-farm	On-farm only	-1.2472*	0.07730	**0.000**	-1.4525	-1.0418
		On-farm + off-farm	-1.2274*	0.10593	**0.000**	-1.5088	-0.9459
		On-farm + non-farm	-1.1749*	0.10593	**0.000**	-1.4563	-0.8935
FCS	On-farm only	On-farm + off-farm	-0.0776	0.12815	1.000	-0.4181	0.2628
		On-farm + non-farm	0.0821	0.12815	1.000	-0.2584	0.4226
		On-farm + off-farm + non-farm	-1.0591*	0.10926	**0.000**	-1.3494	-0.7688
	On-farm + off-farm	On-farm only	0.0776	0.12815	1.000	-0.2628	0.4181
		On-farm + non-farm	0.1597	0.16402	1.000	-0.2761	0.5955
		On-farm + off-farm + non-farm	-0.9815*	0.14973	**0.000**	-1.3793	-0.5837
	On-farm + non-farm	On-farm only	-0.0821	0.12815	1.000	-0.4226	0.2584
		On-farm + off-farm	-0.1597	0.16402	1.000	-0.5955	0.2761
		On-farm + off-farm + non-farm	-1.1412*	0.14973	**0.000**	-1.5390	-0.7434
	On-farm + off-farm + non-farm	On-farm only	1.0591*	0.10926	**0.000**	0.7688	1.3494
		On-farm + off-farm	0.9815*	0.14973	**0.000**	0.5837	1.3793
		On-farm + non-farm	1.1412*	0.14973	**0.000**	0.7434	1.5390

Table 5. The post hoc comparison of One-way MANOVA about the effect of livelihood strategies on the food security status of rural households (cont.)

Multiple comparisons							
Bonferroni							
Dependent variable	(I) Households livelihood strategies	(J) Households livelihood strategies	Mean difference (I-J)	Std. error	Sig.	95% Confidence interval	
						Lower bound	Upper bound
RCSI	On-farm only	On-farm + off-farm	-0.1752	0.13044	1.000	-0.5218	0.1713
		On-farm + non-farm	-0.0919	0.13044	1.000	-0.4384	0.2547
		On-farm + off-farm + non-farm	1.0414*	0.11121	**0.000**	0.7460	1.3369
	On-farm + off-farm	On-farm only	0.1752	0.13044	1.000	-0.1713	0.5218
		On-farm + non-farm	0.0833	0.16695	1.000	-0.3602	0.5269
		On-farm + off-farm + non-farm	1.2167*	0.15240	**0.000**	0.8118	1.6216
	On-farm + non-farm	On-farm only	0.0919	0.13044	1.000	-0.2547	0.4384
		On-farm + off-farm	-0.0833	0.16695	1.000	-0.5269	0.3602
		On-farm + off-farm + non-farm	1.1333*	0.15240	**0.000**	0.7284	1.5382
	On-farm + off-farm + non-farm	On-farm only	-1.0414*	0.11121	**0.000**	-1.3369	-0.7460
		On-farm + off-farm	-1.2167*	0.15240	**0.000**	-1.6216	-0.8118
		On-farm + non-farm	-1.1333*	0.15240	**0.000**	-1.5382	-0.7284

Based on observed means. The error term is mean square (error) = 0.502.

*The mean difference is significant at the 0.05 level.

In conclusion, the post hoc comparisons following the one-way MANOVA analysis provide valuable insights into the complex relationships between livelihood strategies and food security outcomes among rural households. By elucidating the differential impacts of various livelihood combinations on food security indicators, these findings offer actionable guidance for policymakers and development practitioners seeking to design effective interventions to promote food security and resilience in the study areas. However, further research is needed to explore the underlying mechanisms driving these observed differences and to develop targeted strategies that address the multifaceted challenges facing rural households in accessing adequate and nutritious food.

5. CONCLUSION AND RECOMMENDATION

The study provided valuable insights into how different livelihood strategies affect food security among rural households, in landslide-prone areas employing food security measurement scores such as the Household Food Insecurity Access Scale (HFIAS), Food Consumption Score (FCS), and Reduced Coping Strategies Index (RCSI) to measure various aspects of food security. The comprehensive data gathered from these tools allowed for a nuanced understanding of the complex relationships between livelihood strategies and food security outcomes, offering critical information for developing targeted interventions to enhance food security among vulnerable rural communities. The study found that households used various livelihood strategies, significantly impacting food security. Most households depended solely on farming, but those that combined farming with off-farm and non-farm activities had better food security outcomes. The study also revealed that households with diversified livelihoods had less food insecurity, better food consumption scores, and fewer coping mechanisms. Those engaged in a mix of farming, off-farm, and non-farm activities showed better food security indicators. This highlights the importance of diversifying livelihood strategies to improve resilience against food insecurity.

Using one-way MANOVA, the study showed that different livelihood strategies had significant impacts on various dimensions of food security. The findings emphasized the need for interventions that consider the diverse livelihood strategies of households, especially those that promote diversification and income-generating activities. Post hoc comparisons gave detailed insights into how different livelihood combinations affected food

security, helping policymakers design better-targeted interventions to improve food access and resilience.

Finally, the study highlights the importance of diversifying livelihood strategies for improving food security in rural, landslide-prone areas. Policymakers should prioritize programs that encourage households to engage in a mix of farming, off-farm, and non-farm activities. This could involve providing training, resources, and incentives for rural communities to diversify their income sources, which in turn could enhance their resilience to food insecurity. It also calls for additional research to better understand the mechanisms through which livelihood strategies affect food security. Policymakers should support and fund research initiatives that explore these dynamics, particularly about environmental factors like landslides, to inform more comprehensive and effective food security strategies.

ACKNOWLEDGEMENTS

Authors extend their sincere appreciation to all individuals who generously provided data for this research. Their valuable contributions significantly enriched this study and were integral to its successful completion. We are grateful for their willingness to share their expertise and information, which contributed immensely to the advancement of our work.

AUTHORS' CONTRIBUTION: L.T. has performed the study design, literature review, data collection, software analysis, result interpretation, and writing the first draft of the manuscript. A.U. and T.T. screen and coach the work proposed by the first author acting as a tiebreaker or criticizing and editing the work.

FUNDING: This study did not receive any funding.

DATA AVAILABILITY: The datasets used and/or analyzed during the current study are available from the corresponding author upon reasonable request.

CODE AVAILABILITY: The datasets used and/or analyzed during the current study are available from the corresponding author upon reasonable request.

DECLARATIONS

Ethics approval and consent to participate: Approval to conduct research and collect data from respondents was obtained from Arba Minch University Department of Geography and Environmental Studies with a research permit of GeEs 07/16-2023, and carried out by the relevant guidelines listed in the ethics statement. Furthermore, respondents were requested to provide informed consent before taking part in the interview.

Competing Interests: The authors declare no competing interests.

REFERENCES

Adu-Baffour F, Daum T, Birner R. Governance challenges of small-scale gold mining in Ghana: Insights from a process net-map study. Land Use Policy 2021;102(3-4):Article No. 105271.

Agostoni C, Baglioni M, La Vecchia A, Molari G, Berti C. Interlinkages between climate change and food systems: The impact on child malnutrition-narrative review. Nutrients 2023;15(2):Article No. 416.

Alexander P, Brown C, Arneth A, Finnigan J, Rounsevell MDA. Human appropriation of land for food: The role of diet'. Global Environmental Change 2016;41:88-98.

Almukaddem L, Alali J, Habib W. An analytical study of food security indicators for farm households in the coastal area of Syria. Journal of Aridland Agriculture 2022;8:14-9.

Amejo AG. Mapping soil terrain resources and descriptions of agroecological zones in Dawuro and Gamo Gofa zones in south-western Ethiopia. Journal of Soil Science and Environmental Management 2018;9(10):164-79.

Anderson E, Wei R, Liu B, Plummer R, Kelahan H, Tamez M, et al. Improving healthy food choices in low-income settings in the United States using behavioral economic-based adaptations to choice architecture. Frontiers in Nutrition 2021;8:Article No. 734991.

Asfaw A, Simane B, Hassen A, Bantider A. Determinants of nonfarm livelihood diversification: Evidence from rainfed-dependent smallholder farmers in north-central Ethiopia (Woleka sub-basin). Development Studies Research 2017;4(1):22-36.

Asiedu B, Adetola JO, Odame KI. Aquaculture in troubled climate: Farmers' perception of climate change and their adaptation. Cogent Food and Agriculture 2017;3(1):Article No. 1296400.

Assefa E, Bork HR. Dynamics and driving forces of agricultural landscapes in Southern Ethiopia a case study of the Chencha and Arbaminch areas. Journal of Land Use Science 2016;11(3):278-93.

Ates C, Kaymaz O, Kale HE, Tekindal MA. Comparison of test statistics of nonnormal and unbalanced samples for multivariate analysis of variance in terms of type-I error rates. Computational and Mathematical Methods in Medicine 2019;15:Article No. 2173638.

Balehegn M, Duncan A, Tolera A, Ayantunde AA, Issa S, Karimou M, et al. Improving adoption of technologies and interventions for increasing the supply of quality livestock feed in low-and middle-income countries. Global Food Security 2020;26:Article No. 100372.

Barnett J. Global environmental change II: Political economies of vulnerability to climate change. Progress in Human Geography 2020;44(6):1172-84.

Brown TA. Confirmatory Factor Analysis for Applied Research. 2nd ed. New York, USA: Guilford Publications; 2014.

Cholo TC, Fleskens L, Sietz D, Peerlings J. Land fragmentation, climate change adaptation, and food security in the Gamo Highlands of Ethiopia. Agricultural Economics 2019; 50(1):39-49.

Cholo TC, Fleskens L, Sietz D, Peerlings J. Is Land fragmentation facilitating or obstructing adoption of climate adaptation measures in Ethiopia? Sustainability 2018;10(7):Article No. 2120.

Dawadi S, Shrestha S, Giri RA. Mixed-methods research: A discussion on its types, challenges, and criticisms. Journal of Practical Studies in Education 2021;2(2):25-36.

Finch WH. Multivariate analysis of variance for multilevel data: A simulation study comparing methods. The Journal of Experimental Education 2022;90(1):173-90.

Fitzpatrick K, Greenhalgh-Stanley N, Ver Ploeg M. Food deserts and diet-related health outcomes of the elderly. Food Policy 2019;87:Article No. 101747.

Food and Agriculture Organization of the United Nations (FAO). International fund for agricultural development, united nations children's fund, world food programme, and world health organization. The state of food security and nutrition in the world 2023: Report on the urbanization, agrifood systems transformation, and healthy diets across the rural-urban continuum [Internet]. 2023 [cited 2024 Apr 21]. Available from: https://www.who.int/publications/m/item/the-state-of-food-security-and-nutrition-in-the-world-2023.

Food and Agriculture Organization of the United Nations (FAO). Report on the building resilience to climate change-related and other disasters in Ethiopia challenges, lessons, and the way forward [Internet]. 2022 [cited 2024 Mar 21]. Available from: https://openknowledge.fao.org/items/704fc8be-cd6e-4206-914c-7a0354bdfa2c.

Food and Agriculture Organization of the United Nations (FAO), World Food Programme (WFP), International Fund for Agricultural Development (IFAD). The state of food insecurity in the world 2014: Strengthening the enabling environment for food security and nutrition [Internet]. 2014 [cited 2024 Mar 29]. Available from: https://reliefweb.int/report/world/state-food-insecurity-world-2014-strengthening-enabling-environment-food-security-and.

Giannini A, Nebie EKI, Ba D, Ndiaye O. Livelihood strategies shape vulnerability of households' food security to climate in Senegal. Frontiers in Climate 2021;3:Article No. 731036.

Haji-Othman Y, Yusuff MSS, Ahmad MN. Pilot testing of internal consistency and reliability of questionnaire items in the compliance behavior of income Zakat study. International Journal of Research in Business and Social Science 2021;11(9):1590-601.

Kassegn A, Endris E. Review on livelihood diversification and food security situations in Ethiopia. Cogent Food and Agriculture 2021;7(1):Article No. 1882135.

Khamis F, El-Refae G. Applying multivariate and univariate analysis of variance on socioeconomic, health, and security variables in Jordan. Statistics, Opimimaization and Information Computing 2020;8(2):386-402.

Kini J. Multidimensional food security index: A comprehensive approach. Asian Journal of Agricultural Extension, Economics and Sociology 2022;40(12):317-31.

Kurnia W, Hizbaron DR. Sustainable livelihood strategies: Comparative cases at the aftermath of landslide at Ponorogo and Bantul, Indonesia. IOP Conference Series: Earth and Environmental Science 2020;451(1):Article No. 012102.

Landler L, Ruxton GD, Malkemper EP. The multivariate analysis of variance as a powerful approach for circular data. Movement Ecology 2022;10:Article No. 21.

Landler L, Ruxton GD, Malkemper EP. Circular data in biology: Advice for effectively implementing statistical procedures. Behavioral Ecology and Sociobiology 2018;72:Article No. 128.

Massa MM, Mosa A. Conservational tree growing by smallholder farm households: evidence from Gamo highlands of Southern Ethiopia. Environmental Systems Research 2021;10:Article No. 5.

Maposa D, Mudimu E, Ngwenya O. A multivariate analysis of variance (MANOVA) of the performance of sorghum lines in different agro-ecological regions of Zimbabwe. African Journal of Agricultural Research 2010;5(3):196-203.

Mekonnen DA, Gerber N. Aspirations and food security in rural Ethiopia. Food Security 2017; 9:371-85.

Nunnally JC. Psychometric Theory. 2nd ed. New York, USA: McGraw-Hill; 1978.

Pawlak K, Kolodziejczak M. The role of agriculture in ensuring food security in developing countries: Considerations in the context of the problem of sustainable food production. Sustainability 2020;12(13):Article No. 5488.

Sadik NJ, Alwan IM. Applied multivariate analysis of variance in experiment of randomized design. Periodicals of Engineering and Natural Sciences 2020;8(1);365-37.

Shano L, Raghuvanshi TK, Meten M. Landslide susceptibility mapping using frequency ratio model: The case of Gamo Highland, South Ethiopia. Arabian Journal of Geosciences 2021;14(7):Article No. 623.

Schober P, Boer MC, Schwarte LA. Correlation coefficients: Appropriate use and interpretation. Anesthesia and Analgesia 2018;126(5):1763-8.

Shone M, Demissie T, Yohannes B, Yohannis M. Household food in security and associated factors in West Abaya District, Southern Ethiopia. Agriculture and Food Security 2017; 6:Article No. 2.

Tabachnick BG. Fidell LS. Using Multivariate Statistics. 6th ed. Boston, MA; Pearson; 2013.

Tadesse E, Tessema A, Abaynesh Y. Rural livelihood strategies and food security: The case of Bensa Woreda, Sidama National Regional State, Ethiopia. Research on Humanities and Social Sciences 2022;12(22):1-19.

Tadesse L, Uncha A, Toma T. Landslide vulnerability mapping using multi-criteria decision-making approaches: In Gacho Babba District, Gamo Highlands Southern Ethiopia. Discover Applied Sciences 2024a;6:Article No. 31.

Tadesse L, Uncha A, Toma T. Multiple indicators-based assessment of rural food security status in landslide-prone areas of Southern Ethiopia. Discover Sustainability 2024b;5(109);1-23.

Tesema D, Berhanu A. Rural livelihood strategies and household food security of farmers surrounding derba cement factory, Oromia Region, Ethiopia. Rural Sustainability Research 2018;40(335):1-17.

United States Agency for International Development (USAID). Final FY 2022 global food security strategy (GFSS) implementation report [Internet]. 2022 [cited 2024 May 11]. Available from: https://www.usaid.gov/sites/default/files/202312/FY%202022%20GFSS%20Implementation%20Report.pdf.

United Nations Office for the Coordination of Humanitarian Affairs (OCHA). Annual report on the overview of the work of world vision in Ethiopia from October 2019 to September 2020 [Internet]. 2021 [cited 2024 May 18]. Available from: https://reliefweb.int/report/ethiopia/2020-annual-report-ethiopia.

United States Department of Agriculture (USDA). Guide to measure household food security [Internet]. 2000 [cited 2024 Jul 6]. Available from: https://nhis.ipums.org/nhis/resources/FSGuide.pdf.

Wasti SP, Simkhada P, van Teijlingen ER, Sathian B, Banerjee I. The growing importance of mixed-methods research in health. Nepal Journal of Epidemiol 2022;12(1):1175-8.

World Food Programme (WFP). Report on the Gambia-comprehensive food security and vulnerability analysis (CFSVA) [Internet]. 2016 [cited 2024 Jun 11]. Available from: https://www.wfp.org/publications/gambia-comprehensive-food-security-vulnerability-analysis-cfsva-december-2016.

World Food Programme (WFP). Food consumption analysis: Calculation and use of the food consumption score in food security analysis [Internet]. 2008 [cited 2024 May 11]. Available from: https://docplayer.net/21477560-Food-consumption-analysis-calculation-and-use-of-the-food-consumption-score-in-food-security-analysis.html.

Yamane T. Statistics: An Introductory Analysis. 2nd ed. New York, USA: Harper and Row; 1967.

Yenesew E, Masresha D. Impact of livelihood diversification on rural household food security: Evidence from Goncha-SisoEnesie District of Amhara Regional State, Ethiopia. International Journal of Agricultural Economics 2019; 4(6):288-97.

Yirgu T. Assessment of soil erosion hazard and factors affecting farmers' adoption of soil and water management measure: A case study from upper Domba Watershed, Southern Ethiopia. Heliyon 2022;8(6):e09536.

Environment and Natural Resources Journal

Volume 23
Issue 2
2025

Development of Sustainable Packaging Cushions from Coconut Waste Using 3D Printing Techniques

Pongsak Kitirojapn[1], Sakol Teeravarunyou[2*], Kodchahem Kamolwit[1], and Pavinee Pattanachan[2]

[1]School of Architecture and Design, King Mongkut's University of Technology, Thailand
[2]Environmental and Energy Management for Community and Circular Economy (EEC&C) Research Group, King Mongkut's University of Technology, Thailand

ARTICLE INFO

Received: 8 Aug 2024
Received in revised: 8 Nov 2024
Accepted: 18 Dec 2024
Published online: 17 Feb 2025
DOI: 10.32526/ennrj/23/20240224

Keywords:
Coconut fiber/ Waste material/ Packaging/ Mold design/ 3D printing

*** Corresponding author:**
E-mail:
sakol.tee@mail.kmutt.ac.th

ABSTRACT

Coconut fiber and coconut coir dust can be used to create environmentally friendly packaging. Additionally, recycled corrugated paper can be combined with tapioca starch to bind coconut coir dust and paper. Using these techniques, our objective was to develop a novel process for producing different items with coconut pulp paper and 3D-printed molds. The results indicated that the optimal weight ratios of paper, coconut fiber, and coconut coir dust for a bottle, corner cushion and wrapping cushions were 60:20:20, 60:20:20, and 80:20:0, respectively. The 3D-printed molds were designed with rounded chamfers to facilitate easy extraction of the molded paper. Both the bottle and corner cushions exhibited a tensile strength of 0.53 MPa with 12% NaOH treatment. The wrapping cushion demonstrated the highest flexural strength, at 10.33 MPa with 12% NaOH. Overall, NaOH treatment improved the mechanical properties of the coconut fiber compared to untreated fiber. For compression, the bottle and corner cushions achieved values of 3,196.38 N and 1,550.68 N, respectively. Furthermore, both the bottle and wrapping cushions passed the drop test from a height of 150 centimeters. In Thailand, the coconut industry reports revenues of approximately 4.66 billion THB in 2023 and produces 337 million metric tons of waste. This research demonstrates the great potential of coconut by-products, and the utilization of waste valued at 647 million THB. Future studies could explore innovative mold designs to enable the production of more complex packaging and decorative items, further enhancing the economic and environmental benefits of coconut waste utilization.

1. INTRODUCTION

The cultivation of aromatic coconuts in Thailand has steadily increased over the years. According to the Agricultural Production Information System, the cultivated area rose from 53,108 acres in 2011 to 81,376 acres in 2021. However, this increased production creates significant waste material, particularly coconut husk. This study focuses on waste reduction and value addition, utilizing aromatic coconut husks presents a significant opportunity (Thyavihalli Girijappa et al., 2019). Numerous research studies have explored various combinations of cushion materials. One notable finding was that a study combining coconut fiber with rice husk developed and tested a sustainable cushioning material. The optimal composition, found to be 50% coconut fiber with 50% rice husk, which showed superior performance in cushioning applications and exhibited optimal resilience, successfully enduring impacts up to a height of 92 centimeters in drop tests (Mohamad et al., 2024). However, this blend necessitates the use of latex adhesive, a chemical compound. Castro (2012) investigated the effectiveness of coconut fiber as a cushioning material through shock absorption tests. Interestingly, unprocessed coconut fiber wrappings performed better than coconut fiber wrappings that included binding agents. However, binders allow for denser packing of

Citation: Kitirojapn P, Teeravarunyou S, Kamolwit K, Pattanachan P. Development of sustainable packaging cushions from coconut waste using 3D printing techniques. Environ. Nat. Resour. J. 2025;23(2):132-141. (https://doi.org/10.32526/ennrj/23/20240224)

the cushioning material, reducing air gaps between the fibers and enhancing the flexibility of the material.

The study of the development of packaging paper from tender coconut husk with starch as an additive show that the paper has good mechanical properties and a degradation rate of approximately 70% within 20 days. This indicates that tender coconut husk is a biodegradable material with the potential to produce paper used for packaging materials (Pandiselvam et al., 2024). Another method for paper production involves blending 25% coir fiber with 75% newspaper and a 20-minute beating process to achieve optimal mechanical properties (Othman et al., 2013). A further investigation explored the combination of coir and cotton fiber as constituents to produce carry bags. The study yielded results indicating an Izod test impact value of 0.15 J, alongside a tensile strength measurement of 0.00268 MPa (Vishnu Nandan et al., 2023). In another investigation, waste paper and coconut fiber were combined in a 4:1 ratio, resulting in a tensile strength exceeding 0.00001 MPa. There is room for further exploration into the various types of waste paper and the optimal ratio of waste paper to coconut fiber in future investigations.

Currently, the pulp manufacturing process involves blending raw materials, molding pulp onto forms, extracting excess water, and pressing and drying it between two heated matched halves of a mold. However, this method demands significant heat energy and water consumption. Furthermore, the aluminum molds used in pulp molding machines are costly and require large quantities, this presents challenges for customization and affordability, especially within local communities. However, there is a promising alternative on the horizon. By utilizing recycled cardboard in conjunction with molds generated with 3D printers, a more cost-effective solution becomes accessible to local communities (Flowalistik, 2023). This straightforward approach not only simplifies implementation but also provides similar functionality. The aim of this study is to explore 3D printing technology's use in creating molds capable of shaping materials like coconut fiber, coconut coir dust, and recycled cardboard. The experiment seeks to determine the optimal ratios of these components, considering the functional efficacy of the 3D-printed molds in the molding process. The binder also serves as an organic material that promotes environmental friendliness. Integrating technology, innovation, and research can make these materials usable and applicable. The identified research gaps are: 1) The absence of a standardized formula for a coconut waste-based mixture in cushioning materials, and 2) Limited research in the application of 3D-printed molds for the production process of sustainable cushioning materials.

2. METHODOLOGY

The study investigated the composition ratios of materials used in shaping cushion-resistant materials for products (bottles) and packaging (corners) using the Triaxial Blend method. This method involves three types of materials: recycled corrugated paper, coconut fibers, and coconut coir dust. Since the wrapping shock-proof cushion requires flexibility when wrapping, coconut coir dust is not appropriate to be an ingredient.

Five different material ratios will be tested and adjusted accordingly to ensure suitability for each specific application (Table 1), with a focus on safety and efficiency of the produced cushion-resistant materials.

Table 1. Ratios of percentage formulation of materials

Ratio	Percentage Formulation			Remarks
	Corrugated paper	Coconut fiber	Coconut coir dust	
A	60	20	20	For bottle and corner cushion
B	40	20	40	Same as above
C	20	20	60	Same as above
D	80	20	0	For wrapping shock-proof cushion
F	60	40	0	Same as above

2.1 Material preparation

2.1.1 Coconut fiber

The preparation of coconut fibers can be divided into two steps. Step 1: Coconut fibers that have not been treated with chemicals are tested for mechanical properties, and the best fibers are selected for the next step. Step 2: Coconut fibers are treated with NaOH (Shoeb et al., 2024). In preparing

chemically treated coconut fibers, the appropriate conditions for treating coconut fibers are studied. The main factor studied is the concentration of NaOH at three levels: 12%, 14%, and 16%, with a boiling time of 3 h at a temperature of 100±5 degrees Celsius (°C). In the chemical treatment process, NaOH concentrations of 12%, 14%, and 16% were selected to optimize the fiber's mechanical properties. These concentrations were chosen based on their effectiveness in breaking down lignin and hemicellulose, which improves the tensile and flexibility characteristics of coconut fibers. In various studies, around 12% NaOH is commonly used as it effectively removes lignin, hemicellulose, and other impurities from natural fibers. The % yield was calculated, revealing that 12% NaOH provided the highest % yield. Increasing the NaOH concentration resulted in a decrease in % yield (Sayakulu and Soloi, 2022). This concentration optimally improves fiber surface roughness, which enhances adhesion between the fiber and the matrix in composites, without over-degrading the fibers.

2.1.2 Coconut coir dust

To prepare coconut coir dust, it is initially passed through a standard mesh sieve with a size of No. 16 (gap size of 1.18 mm). This step aims to facilitate the subsequent use of coconut coir dust as a composite material for manufacturing impact-resistant materials. Then, the coconut coir dust that has undergone sieving is dried in a hot air oven at 60 °C for 24 h to maintain a constant moisture content of less than 10%.

2.1.3 Pulp paper

To shape impact-resistant materials, discarded cardboard is utilized. It is shredded into small pieces and soaked in water for 24 h to soften it, making it easier to pulp. Afterwards, it is finely pulped using a paper pulp beater.

2.1.4 Binder

Use a ratio of 20 g of tapioca starch to 200 mL of tap water per 100 g of material. Mix the starch and water thoroughly, bring to a boil, and stir until a sticky consistency is achieved. It should form a clear gel that looks like a wet paste glue.

2.1.5 Enhanced 3D printing mold process

The present study explores the use of 3D printing technology to create cushioning materials tailored for diverse packaging needs. Utilizing a Delta X 200 printer and 1.75 mm Poly Lactic Acid (PLA) filament, the mold design comprises male and female parts with a precise 1.5 mm gap to ensure optimal material thickness and flexibility. Key design considerations include the integration of multiple drainage holes to prevent air pockets to ensure uniform density. Additionally, the molds feature angled slopes in addition to rounded chamfers, approximately 3 mm radius, to facilitate the smooth removal of molded objects and avoiding any potential damage during the extraction process. The thickness of the cushioning material can be customized by altering the 1.5 mm gap, providing the necessary level of protection for different products. The 3D printing mold process was enhanced to support the specific needs of the coconut fiber composite material. Using PLA allows for a sustainable and flexible approach, aligning with the project's environmental goals and providing a cost-effective solution for mold modifications as required.

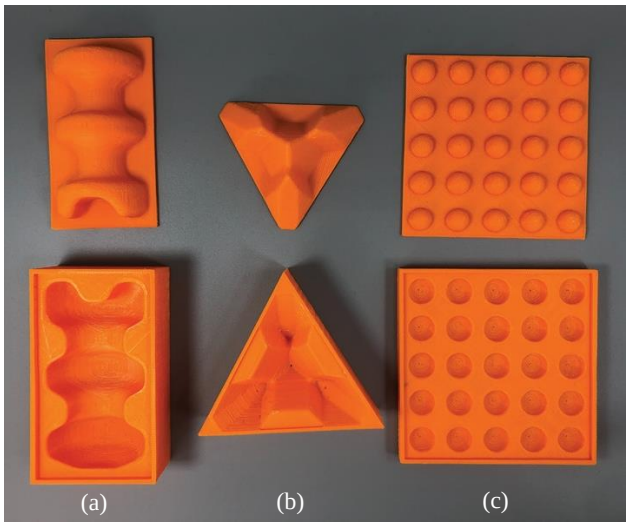

Figure 1. 3D-printed molds for (a) bottle cushion, (b) corner cushion, and (c) wrapping cushion

Three distinct usage patterns for the cushioning materials were tested:

1. Bottle cushion (Figure 1(a)): Molds were designed with cavities that conform to the contours of small glass bottles, such as perfume or herbal oil bottles, ensuring a secure fit and minimizing the risk of breakage.

2. Corner cushion for triangular packaging (Figure 1(b)): Molds produce triangular-shaped cushioning materials that fit into the corners of packaging, effectively reducing external impacts by absorbing and distributing force.

3. Wrapping cushion (Figure 1(c)): Molds create flexible, elongated cushioning materials suitable for wrapping or bundling products.

2.2 Mechanical properties of the samples

The samples will undergo mechanical testing according to ASTM standards using an Impact Testing Machine and a Universal Testing Machine (UTM) for impact resistance, tensile strength, flexural strength, and compressive strength. A) Impact Test: Rectangular specimens will be tested per ASTM D256 standards using the Izod method. B) Tensile Test: Dumbbell-shaped specimens will be tested per ASTM D638 standards for tensile and flexural strength. C) Compression Test: Compression testing will be conducted on bottle and corner configurations to determine compressive strength.

2.3 Scanning electron microscopy (SEM)

The microstructure of the board samples was analyzed using a Thermo Fisher Scientific Phenom ProX scanning electron microscope (SEM) with an acceleration voltage of 5 kV.

3. RESULTS AND DISCUSSION

3.1 Mechanical properties

Table 2 presents the results of mechanical properties testing of five different formulations (labeled A to E) of cushion packaging. The formulations vary in the proportions of corrugated paper, coconut fiber, and coconut coir dust. The table shows the results of mechanical testing for cushion packaging formulations.

Table 2. Results of mechanical properties testing of cushion packaging (untreated).

Ratio	Formulation (%)			Impact		Tensile		Flexural		Compress	Remarks
	Corrugated paper	Coconut fiber	Coconut coir dust	Energy absorption (J)	Energy absorption per area (kJ/m^2)	Tensile strength (MPa)	Strain (%)	Max strength (N)	Max. stress (MPa)	Max. compression (N)	
A	60	20	20	0.19	0.60	0.47	1.62	11.22	6.43	1,105.59, 167.31	Bottle cushion, Corner cushion
B	40	20	40	0.11	0.33	0.14	0.62	9.43	4.07	1,020.86, 45.43	Same as above
C	20	20	60	0.28	0.86	0.13	0.59	10.70	2.00	1,033.58, 63.27	Same as above
D	80	20	0	0.05	0.15	0.36	1.96	9.38	8.68	-	Wrapping cushion
E	60	40	0	0.04	0.13	0.34	1.86	9.25	9.16	-	Same as above

3.1.1 Impact test

According to the Izod test principles, the test results indicate products (bottle cushion) and packaging (corner cushion), made from a mixture of paper, untreated coconut fiber, and coconut coir dust at ratio C, exhibits the highest ability to withstand impact or shock. This is evidenced by an absorbed energy of 0.28 J and an absorbed energy per unit area of 0.86 kJ/m². Following closely is ratio A, which shows absorbed energy values of 0.19 J and 0.60 kJ/m², respectively. Both sets of specimens exhibit ductile fractures, forming a 45° angle or flexural fracture, maintaining some degree of cohesion (Figure 2(b) and Figure 2(d)). In contrast, ratio B displays the least ability to withstand impact, with average absorbed energy values of 0.11 J and 0.33 kJ/m², respectively. The specimens exhibit brittle fractures, featuring a flat, smooth fracture surface, and separate upon impact (Figure 2(c)). The fracture characteristics significantly influence energy absorption during impact, with ductile fractures yielding higher impact energy absorption compared to brittle fractures. For impact-resistant material in wrapping form, those made from a mixture of paper and untreated coconut fibers at ratios D (Figure 2(e)) and E (Figure 2(f)), have the ability to withstand impact or shock that is relatively similar. The absorbed energy values are approximately 0.05 J and 0.04 J, respectively, with absorbed energy per unit area values around 0.15 kJ/m² and 0.13 kJ/m², respectively.

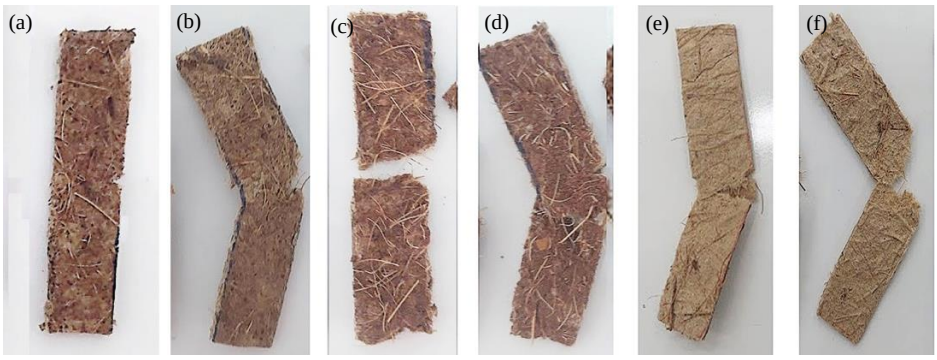

Figure 2. Impact test results of paper, untreated coconut fiber, and coconut coir dust at different ratios: (a) shape before testing, (b) 60:20:20, (c) 40:20:40, (d) 20:20:60, (e) 80:20:0, and (f) 60:40:0

3.1.2 Tensile test

The tensile test determines the stress when a material is subjected to force in a tensile manner, resisting separation (Figure 3). It was found that the ratio A of paper: untreated coconut fiber: coconut coir dust yielded the highest maximum tensile stress and strain values of 0.47 MPa and 1.62%, respectively, for impact-resistant products (bottle cushion) and packaging materials (corner cushion). Similarly, ratio B showed maximum tensile stress and strain values of 0.14 MPa and 0.62%, closely followed by ratio C with values of 0.13 MPa and 0.59%, respectively. An increase in the coconut coir dust content resulted in reduced maximum tensile stress and strain values due to its foam-like structure, which compromises adhesion and cohesion within the composite material. Enhancing tensile strength can be achieved by adding an appropriate amount of coconut coir dust, known for its natural fiber characteristics such as a porous structure and short fibers. However, excessive coconut coir dust may burden other composite materials without improving tensile strength, potentially due to poor interfacial bonding between particles and the matrix.

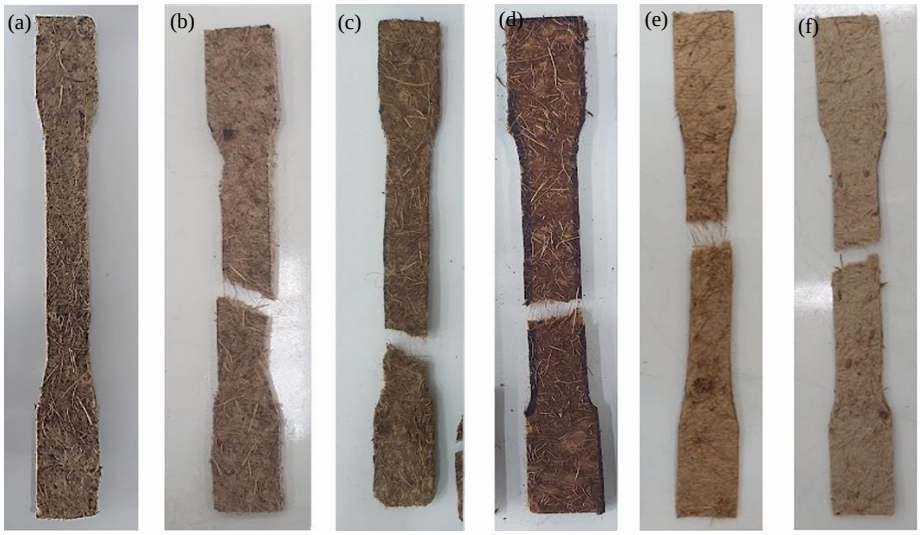

Figure 3. Tensile test results of paper, untreated coconut fiber, and coconut coir dust at various ratios: (a) shape before testing, (b) 60:20:20, (c) 40:20:40, (d) 20:20:60, (e) 80:20:0, and (f) 60:40:0\

3.1.3 Flexural test

In shaping impact-resistant products (bottle cushion) and packaging materials (corner cushion) from a mixture of paper (Figure 4), untreated coconut fiber, and coconut coir dust, ratio of 60:20:20 (Figure 4(b)) exhibits the highest flexural load and flexural strength, measuring 11.22 N and 6.43 MPa, respectively. Notably, ratio of 20:20:60 (Figure 4(d)) has a higher flexural load than ratio 40:20:40 (Figure 4(c)). However, under maximum force, both ratios of 40:20:40 and 20:20:60 exhibit flexural and fracturing characteristics. The strength of composite materials is notably affected by their thickness, with flexural strength decreasing as thickness increases. Ratios

80:20:0 (Figure 4(e)) and 60:40:0 (Figure 4(f)) exhibit similar flexural loads. The inclusion of both short and long coconut fibers in the wrapping-type cushioning material enhances its flexural resistance capabilities.

Figure 4. Flexural test results of paper, untreated coconut fiber, and coconut coir dust at various ratios: (a) shape before testing, (b) 60:20:20, (c) 40:20:40, (d) 20:20:60, (e) 80:20:0, and (f) 60:40:0

3.1.4 Compression test

When formed from a mixture of paper, untreated coconut fiber, and coconut coir dust at ratio A, bottle-type cushion packaging exhibits maximum compressive strength capabilities of 1,105.59 N, whereas corner-type cushion packaging reaches 167.31 N. Similarly, at ratio C, compressive strength capabilities are 1,033.58 N for bottle-type and 63.27 N for corner-type, while at ratio B, these values decrease to 1,020.86 N and 45.43 N, respectively. The fracture or tear characteristics of bottle-type and corner-type cushioning materials under compressive testing at a ratio of 60:20:20 (Figure 5(b)) show that the samples maintain their shape and incur less damage compared to ratios of 40:20:40 (Figure 5(c)) and 20:20:60 (Figure 5(d)). This is because the structure of corrugated paper consists of interconnected curved cells, which have a high compressive strength capacity. Similar to the bottle type, the 60:20:20 (Figure 5(f)) ratio can maintain its shape the best. Then, both the corner and bottle types with a 60:20:20 ratio were selected for testing after being treated with 12% NaOH.

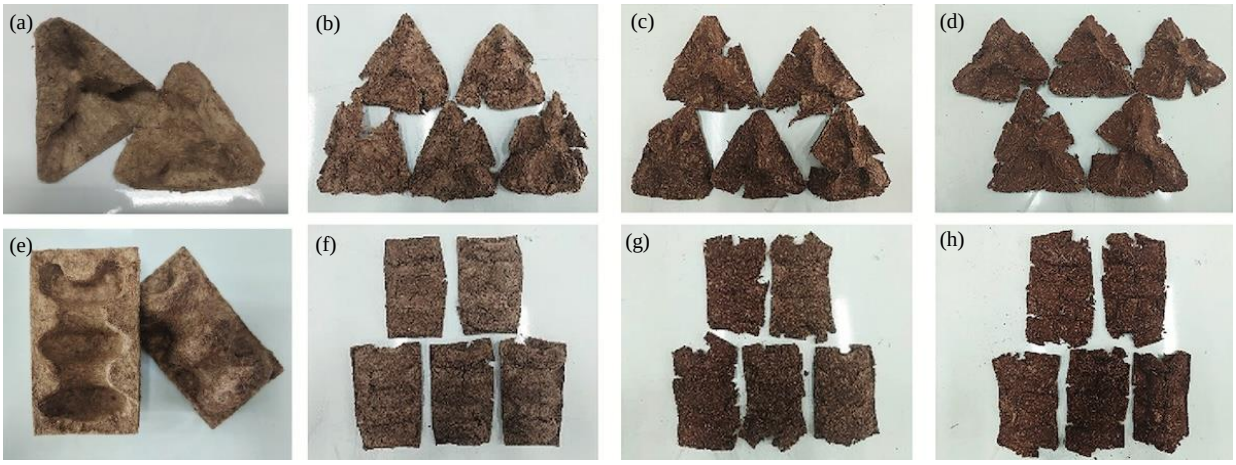

Figure 5. Compression test results of paper, untreated coconut fiber, and coconut coir dust at various ratios: (a) corner cushion shape before testing, (b) 60:20:20 for corner cushion, (c) 40:20:40 for corner cushion, (d) 20:20:60 for corner cushion, (e) bottle cushion shape before testing, (f) 60:20:20 for bottle cushion, (g) 40:20:40 for bottle cushion, and (h) 20:20:60 for bottle cushion

3.2 Coconut fiber treated with NaOH

It was found that cushion packaging products (bottles) and cushion packaging (corners) can be successfully produced using a mixture of paper, coconut fiber (12% NaOH treated), and coconut coir dust at ratio A (60:20:20) Additionally, cushioning material in wrapping form can be produced at ratio D (80:20:0) using the same coconut fiber treatment, which yielded the best mechanical properties compared to using untreated coconut fiber. Cushioning materials in wrapping type from the mixture of coconut fiber treated with NaOH demonstrate good flexibility - they can be rolled, folded, and bent effectively. NaOH exhibits superior mechanical characteristics compared to untreated coconut fibers (Table 3). NaOH accelerates breakdown and removes hemicellulose and lignin from cellulose. Lignin, a natural polymer binding cellulose fibers in plant cell walls and acts as a barrier against microbial degradation of cellulose and hemicellulose. Studies indicate that treated coconut fiber exhibits higher tensile strengths compared to untreated fiber (Mir et al., 2012). For instance, coconut fiber treated with 10% NaOH combined with ethylene vinyl alcohol copolymers (EVOH) and starch achieves tensile strengths ranging from 8.9 to 13.6 MPa (Rosa et al., 2009). In contrast, coconut fiber treated with 12% NaOH in cushioning material composite exhibits tensile strengths of 0.53 to 0.54 MPa. Additionally, the presence of coconut coir may affect the composite's overall hardness due to its soft and highly flexible nature (Mohan et al., 2025). Optimal force reception efficiency can be achieved by adjusting the amount of coconut coir dust. Bottle and corner cushions made by mixing paper, coconut coir dust, and coconut fiber treated with NaOH demonstrate compression strengths 2-3 times higher than cushions using untreated coconut fiber (3,196.38 N and 1,550.68 N for bottle and corner cushions, respectively).

Table 3. The mechanical properties testing results of bottle-type and corner-type cushion packaging, as well as wrapping-form cushioning materials, fabricated using a mixture of materials including coconut fiber treated with 12% NaOH.

Type	Formulation (%)			Impact		Tensile		Flexural		Compression
	Corrugated paper	Coconut fiber	Coconut coir dust	Energy absorption (J)	Energy absorption per area (kJ/m^2)	Tensile strength (MPa)	Strain (%)	Max. flexural Strength (N)	Max. stress (MPa)	Max. compression (N)
Bottle cushion	60	20	20	0.25	0.79	0.53	1.64	11.59	4.54	3,196.38
Corner cushion	60	20	20	0.25	0.79	0.53	1.64	11.59	4.54	1,550.68
Wrapping cushion	80	20	0	0.08	0.25	0.54	2.52	10.33	10.15	-

3.3 Drop test

Three forms of final cushion packaging are used to protect bottles, boxes, and glass tubes (Figure 6). Impact resistance tests on cushioning materials commonly utilize the free-fall test method. In this test, glass bottles filled with water are placed into both bottle-type and wrapping-type cushioning materials. These packaged samples are then inserted into shipping boxes and dropped from specified heights - 30, 60, 90, 120, and 150 centimeters - repeatedly. Upon unpacking the boxes and inspecting the packaged goods, it was observed that the glass bottles did not crack or sustain any damage at any tested height level. This indicates that both bottle-type and wrapping-type cushioning materials made from coconut husk effectively resist impacts, thereby protecting the packaged goods from damage. This research utilizes only 20% coconut fiber in producing cushioning material. In contrast, cushioning materials specifically designed for glass bottles often require up to 50% coconut fiber mixed with rice husks to achieve optimal packaging performance (Mohamad et al., 2024).

3.4 Microstructure study

Scanning Electron Microscope (SEM) analysis was conducted to investigate the microstructure and potential failure characteristics of coconut fiber. This analysis included examining both the surface and cross-sectional features of fibers to assess how these characteristics could affect fiber-matrix adhesion and structural integrity under stress. Two different

composition ratios were analyzed: 1) a mixture of paper, coconut fiber, and coconut coir dust at a 60:20:20 ratio, and 2) a mixture of paper and coconut fiber at an 80:20 ratio, with and without NaOH treatment.

The SEM images of untreated coconut fibers (Figure 7(a)) show a surface with both smooth and rough regions, resulting in an uneven texture that limits adhesion with the matrix, potentially leading to interfacial failure. The presence of lignin and fatty substances between cells provides a strong cohesion within untreated fibers. Embedded spherical structures, or tyloses, resemble small bubbles, which may contribute to structural failure points under stress. The cross-sectional SEM image (Figure 7(c)) reveals a honeycomb-like structure with numerous pores (lumens), which can enhance toughness and energy absorption (Hwang et al., 2016; Faria et al., 2023).

Upon NaOH treatment, the SEM images (Figure 7(d)) show expanded voids and increased surface roughness, which improve mechanical interlocking and fiber-matrix adhesion, reducing potential failure at the fiber-matrix interface. These morphological changes, including increased porosity, contribute to a stronger bond and mitigate interfacial failure, enhancing the overall structural integrity of the treated composite material.

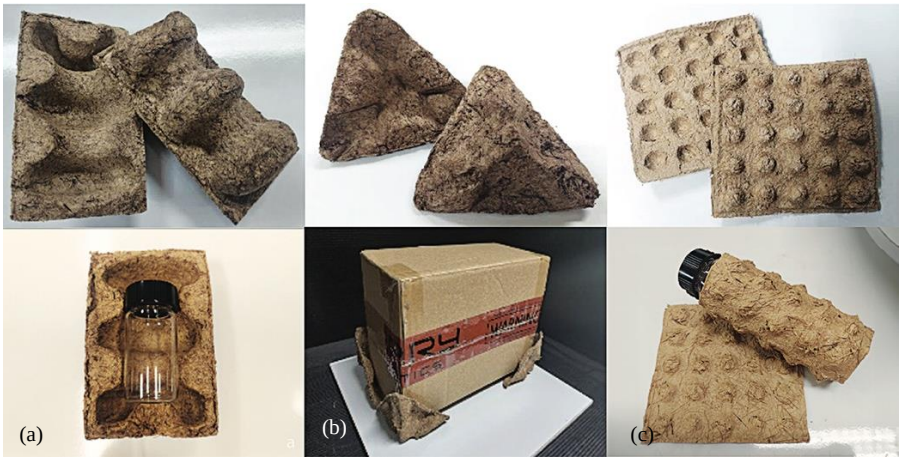

Figure 6. Three forms of final cushion packaging: (a) bottle type, (b) corner type, and (c) wrapping type

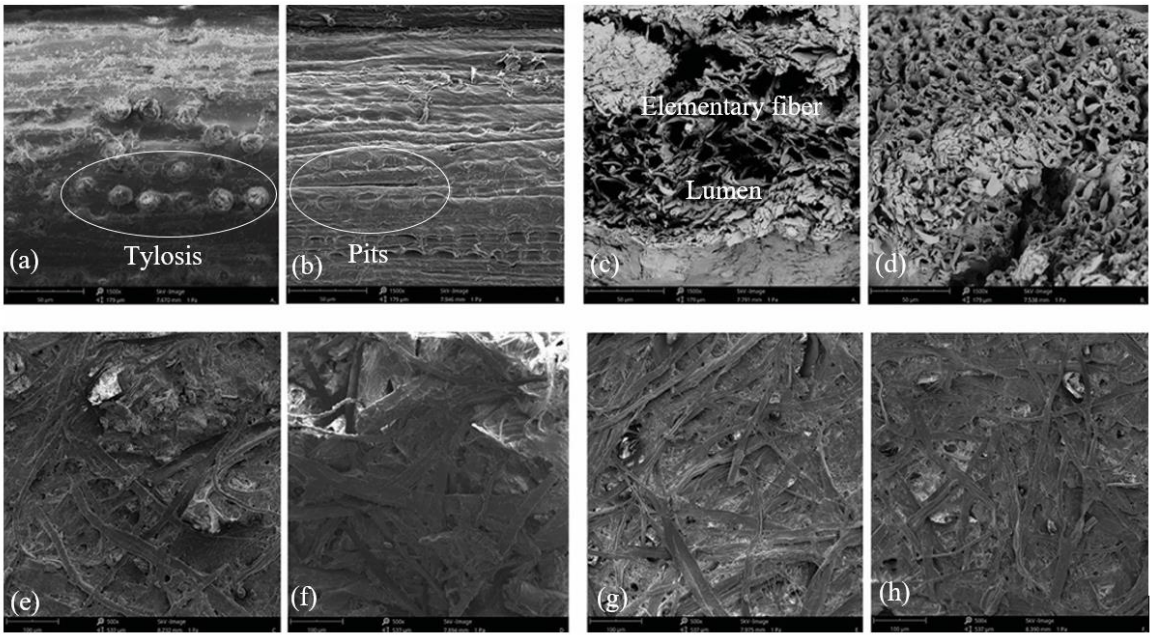

Figure 7. SEM micrographs of coconut fiber (a) Surface of fiber without NaOH, (b) Surface with 12% NaOH, (c) Cross section without NaOH, (d) Cross section with 12% NaOH, (e) Ratio of paper: coconut fiber: coconut coir dust at 60:20:20, (f) 60:20:20 with NaOH, (g) Ratio of paper: coconut fiber at 80:20 and (h) 80:20 with NaOH

This results in increased surface area and porosity for the fibers, leading to a significantly rougher and more uniform fiber surface (Rout et al., 2000; Tran et al., 2014; Bradley and Bradley, 2019). The enhanced porous structure of coconut fiber facilitates improved adhesion with other composite materials, thereby enhancing bonding and adhesion between materials. NaOH treatment also serves to cleanse the surface and unveil surface pores, referred to as pits (Figure 7(b)), which are absent on the surface of untreated fibers (Rosa et al., 2009). When untreated coconut fiber was used as a cushioning material alongside other components (paper and coconut coir dust), poor adhesion between the primary materials and the binder was observed. A non-uniform distribution and weak surface strength were evident, attributed to components within the fiber structure hindering adhesion between fibers and other materials (Figure 7(e) and Figure 7(g)). Studies show that even a slight increase in void content in coconut fiber reinforced composites can lead to significant reductions in tensile, flexural, and shear strengths between layers, up to 10-20% (Mehdikhani et al., 2019). In contrast, using NaOH-treated coconut fiber for cushioning materials results in strong adhesion between the primary materials and the binder (Figure 7(f) and Figure 7(h)). NaOH effectively removes lignin, hemicellulose, and other impurities from the fiber surface, breaking down fibers into smaller strands and promoting better integration and cohesion within the material. This process roughens the fiber surface, increases porosity, and creates larger voids, enhancing mechanical bonding between fibers and the matrix (Reddy and Yang, 2015). Improved compatibility between the primary material and binder contributes to enhanced mechanical properties, consistent with the findings of mechanical testing on cushioning materials described earlier.

4. CONCLUSION

This research confirms that the ratios of corrugated paper, coconut fiber, and coconut coir dust were 60:20:20 for bottles and corners cushions, and 80:20:0 for wrapping cushions. Using NaOH-treated coconut fiber enhances impact, tensile, flexural, and compression strengths, and the 3D printing process needs only two molds. Coconut coir dust provides rigidity, similar to box corners, while coconut fiber offers flexibility, making it ideal for shock absorption and flexibility in wrapping shock-proofing materials. This is the first study to use coconut coir dust in cushioning material, advancing the use of coconut-based materials.

NaOH treatment improves coconut fiber's fineness, porous structure, and blending capabilities. However, the chemical treatment may raise environmental and safety concerns. Future research could explore organic alternatives like amines and amino acids, which might offer eco-friendly options. The tensile strength of corrugated board ranges from 15 to 50 pounds per inch (0.10 to 0.34 MPa), and the bottle, corner, and wrapping cushions achieved values of 0.53 to 0.54 MPa, meeting or exceeding this requirement. Treated coconut fiber cushions offer better compression strength than untreated ones, ensuring adequate protection during transit.

Using 3D-printed molds simplifies the process, requiring only two molds instead of three. The material can be shaped with a manual press and Tapioca starch binding, avoiding the need for sun-drying or high temperatures. Molded fiber, with its potential for future development, could benefit from HP's advances in 3D printing and molded fiber technology (HP Development, 2024) and 3D-printed graphene-reinforced composites (Banupriya et al., 2024) Additionally, coconut husk's versatility allows for creative 3D applications in product designs like lamps, bins, and furniture. Future research should focus on large-scale 3D molds, diverse materials, and advanced polymers to enhance durability and functionality.

ACKNOWLEDGEMENTS

This work was supported by (i) King Mongkut's University of Technology Thonburi (KMUTT), (ii) Thailand Science Research and Innovation (TSRI), and (iii) National Science, Research and Innovation Fund (NSRF), Fiscal year 2023 under project number FRB660073/0164.

REFERENCES

Banupriya R, Jeevan TP, Divya HV, Yashas Gowda TG, Manjunath GA. 3D-printed graphene-reinforced composites: Opportunities and challenges. Polymer Composit 2024; 46(2):1250-66.

Bradley W, Bradley S. Using coconut fiber and shell as functional fillers in polyolefin to enhance properties and reduce costs. SPE Sustainability Newsletter 2019;7:4-12.

D. Pinho da Costa Castro C, de Assis Fonseca Faria J, Dantas TBH. Testing the use of coconut fiber as a cushioning material for transport packaging. Materials Sciences and Applications 2012;3(3):151-6.

Faria DL, Mendes LM, Junior JBG. Effect of surface treatment on the technological properties of coconut fiber-reinforced plant

polyurethane composites. Environmental Science and Pollution Research 2023;30(18):52124-40.

Flowalistik. Pulp it! - 3D printable recycled cardboard molds [Internet]. 2023 [cited 2024 Nov 8]. Available from: https://www.instructables.com/Pulp-It/.

HP Development. HP molded fiber for molded pulp production tooling [Internet]. 2024 [cited 2024 Nov 8]. Available from: https://www.hp.com/us-en/printers/3d-printers/molded-fiber-tooling.html.

Hwang C-L, Tran V-A, Hong J-W, Hsieh Y-C. Effects of short coconut fiber on the mechanical properties, plastic cracking behavior, and impact resistance of cementitious composites. Construction and Build Materials 2016;127:984-92.

Mehdikhani M, Gorbatikh L, Verpoest I, Lomov SV. Voids in fiber-reinforced polymer composites: A review on their formation, characteristics, and effects on mechanical performance. Journal of Composite Materials 2019; 53(12):1579-669.

Mir SS, Hasan SMN, Hossain MJ, Hasan M. Chemical modification effect on the mechanical properties of coir fiber. Engineering Journal 2012;16(2):73-83.

Mohamad MAH, Onn N, Halim MAA, Yahya MS, Haidzir NAFM, Ibrahim MZ. Lean design of alternative packaging cushion material for glass bottles using rice husk and coconut fibre. Journal of Advanced Research in Applied Sciences and Engineering Technology 2024;33(2):107-19.

Mohan S, Thilagavathi G, Rajkhowa R. Composite panels utilizing microdust and coir pith for eco-friendly construction solutions. Journal of the Textile Institute 2025;116(2):175-82.

Othman MH, Main NM, Mon SZK, Mohamad Z. Development of paper using coir fibers as a packaging product. Asian Journal of Scientific Research 2013;6(2):207-16.

Pandiselvam R, Harikrishnan MP, Khanashyam AC, Basil M, Anirudh M, Manikantan MR, et al. Development and characterization of gelatinized starch doped microcellulose paper from tender coconut (*Cocos nucifera* L) husk. Process Safety and Environmental Protection 2024;184:615-23.

Reddy N, Yang Y. Natural cellulose fibers from corn stover. In: Innovative Biofibers from Renewable Resources. Berlin, Heidelberg: Springer; 2015. p. 5-8.

Rosa MF, Chiou B sen, Medeiros ES, Wood DF, Williams TG, Mattoso LHC, et al. Effect of fiber treatments on tensile and thermal properties of starch/ethylene vinyl alcohol copolymers/coir biocomposites. Bioresource Technology 2009;100(21):5196-202.

Rout J, Tripathy SS, Nayak SK, Misra M, Mohanty AK. Scanning electron microscopy study of chemically modified coir fibers. Journal of Applied Polymer Science 2000;79:1169-77.

Sayakulu NF, Soloi S. The effect of sodium hydroxide (NaOH) concentration on oil palm empty fruit bunch (OPEFB) cellulose yield. Journal of Physics: Conference Series. IOP Publishing 2022;2314(1):Article No. 12017.

Shoeb M, Kandasami RK, Singh S, Sebastian S. Framework for Treatment of coconut coir fibres through physico-chemical techniques. International Journal of Geosynthetics and Ground Engineering 2024;10(2):1-22.

Thyavihalli Girijappa YG, Mavinkere Rangappa S, Parameswaranpillai J, Siengchin S. Natural Fibers as Sustainable and Renewable Resource for Development of Eco-Friendly Composites: A Comprehensive Review. Frontier in Material 2019;6:Article No. 226.

Tran LQN, Minh TN, Fuentes CA, Chi TT, Van Vuure AW, Verpoest I. Investigation of microstructure and tensile properties of porous natural coir fibre for use in composite materials. Industrial Crops and Products 2014;65:437-45.

Vishnu Nandan H, Anish R, Jayaprasad G, Sunny S, Scaria Jomon J, Shibin R, et al. Experimental investigations on the mechanical properties and thermal analysis of coir-paper hybrid composite carry bag material. Materials Letters 2023;353:Article No. 132252.

Environment and Natural Resources Journal

Volume 23
Issue 2
2025

Numerical Investigation of Hydraulic Performance in Makhool Spillway Dam

Fatima A. Sadiq[1*], Haitham A. Hussein[2], and Mohd R. Rozainy Zainol[3]

[1]*Department of Civil Engineering, Al-Nahrain University, Baghdad, Iraq*
[2]*Civil Engineering Department, College of Engineering, Al-Nahrain University, Baghdad, Iraq*
[3]*School of Civil Engineering, Engineering Campus, University Sains Malaysia, 14300 Nibong Tebal, Penang, Malaysia*

ARTICLE INFO

Received: 22 Jun 2024
Received in revised: 11 Dec 2024
Accepted: 24 Dec 2024
Published online: 27 Feb 2025
DOI: 10.32526/ennrj/23/20240178

Keywords:
Spillway Dam/ Experimental Validation/ CFD Model/ Numerical modeling/ FLOW3D software/ Makhool Dam

*** Corresponding author:**
E-mail: fatima.mciv22@ced.nahrainuniv.edu.iq

ABSTRACT

Dams are critical hydraulic structures, and analyzing their hydraulic properties is essential for ensuring their functionality. While experimental tests have traditionally been used to evaluate the performance of dams, but now (CFD) software, such as among this the Flow 3D, now offers a reliable alternative or complement to physical models, ensuring accuracy while reducing time and effort. This study investigates Makhools' Spillway Dam in Iraq, one of the country's most significant hydraulic projects. A 3D numerical model of the dam was developed to assess its operation and performance. Its properties were analyzed and validated by comparing the results with physical model data, focusing on key hydraulic parameters such as velocity and water flow depth. The velocity results closely align with the physical model data, with only a minor variation in flow depth, which remains within an acceptable range. The RMSE value for velocity was below 5%, while the difference in the flow depth was approximately 3.63%, indicating a strong correlation between the numerical and physical models. These findings confirm that advanced numerical modeling techniques can effectively complement or serve as a reliable alternative to real-world studies.

1. INTRODUCTION

The spillway is structure of the hydroelectric power plant destined to extravagant the exceptional floods to protect the dam against overtopping. In other words, it is the structure used to avoid exceeding the maximum water level of dam reservoir (Pereira, 2020). These structures, which are built with and without control, are one of the most important hydraulic elements of dams (Pataki and Cahill, 1985). The type of spillway depends on the general arrangement of the works of a hydroelectric power plant, which in turn depends on the topographical and geological characteristics of the site. The spillway generally has five distinct elements: approach channel, control structure, chute channel, energy dissipate, and exit channel (Pereira, 2020). It must be strong enough because it exposes the safety of the dam to danger if the amount of water is greater than its designed limit, especially in the event of a flood (Kocaer and Yarar, 2020). The United States Bureau of Reclamation (USBR) and the United States Army Crop of Engineers (USACE) conducted several model tests and investigations to develop a general formula for spillway hydraulic properties such as discharge coefficients of hydraulic pressure, crest, and energy-dispersion efficiency of the damping basin (Rajaa, 2020). The Physical models simulate and analyze the complexity of flow distribution over a spillway (5) (Erpicum et al., 2016). Creating a physical model is beneficial for understanding the characteristics of a dam and ogee spillway. Physical modeling allows for analyzing hydraulic behavior, such as discharge curves, flow elevation, flow velocity, flow direction patterns, and hydrostatic pressure (Manogaran et al., 2022). It helps in evaluating the effectiveness of energy-dissipating structures, such as stilling basins

Citation: Sadiq FA, Hussein HA, Zainol MRR. Numerical investigation of hydraulic performance in Makhool Spillway Dam. Environ. Nat. Resour. J. 2025;23(2):142-150. (https://doi.org/10.32526/ennrj/23/20240178)

and stepped spillways, and also in minimizing kinetic energy and preventing scour and erosion (Zahari et al., 2022). For more than 100 years, laboratory modeling has been an effective tool for investigations of hydraulic characteristics (Rajaa, 2020). But from previous experiences with physical models, creating a physical model to understand the characteristics of a dam has several disadvantages. Firstly, physical modeling can be time-consuming and expensive, requiring the construction of scaled-down replicas of the structures (Manogaran et al., 2022). Secondly, there is a scale effect in physical modeling, which means that the results obtained from the model may not accurately represent the behavior of the actual structures (i.e., reduced prototype scale according to the law of similarly of Froude number can cause errors in the results) (Kote and Nangare, 2019). This can lead to discrepancies between the measured data and the prototype, affecting the accuracy of the design (Saneie et al., 2016). Errors that may happen in drainage ditches in any design mistake can lead to major and irreversible consequences, studies and experimental studies have recently been seen as supporting parts (Kocaer and Yarar, 2020). Therefore, there has been a surge in investigative studies employing numerical models. These models allow for the examination and simulation of the hydrodynamic performance of spillways with sensible cost and time, thus contributing to recent advances in the field. CFD (computational fluid dynamics) modeling is a numerical method for solving flow equations such as mass and momentum (3D Navier Stokes equations). Recently, there have been many CFD software designed for fluid flow modeling such as Autodesk CFD and CFX, Flow-3D, Sim Scale, Power Flow, Open FOAM, COMSOL Multiphysics, Ansys Fluent, etc. (Li et al., 2011; Samadi et al., 2020; Jahad et al., 2018; Yusuf and Micovic, 2020; Rahimzadeh et al., 2012; Banerjee, 2018; Dargahi, 2006; Sartaj et al., 2006; Hekmatzadeh et al., 2018). Flow-3D software system has been used to model and simulate flow patterns and the flow over dam spillways for many discharges with excellent accuracy, suitable cost, and less time to study more forecasts compared to physical models (Rajaa, 2020). It is considered the best for simulating a water drainage channel. Many studies have been conducted on it and the results have been very good. Several researchers have tried to predict flow characteristics on spillways using numerical and physical models (Rajaa, 2020). Savage and Johnson (2001) gave a numerical study in using the CFD systems of the Flow 3D program discretized with hexahedral cells to compute the flow in order to compare the numerical results with physical model data as presented in the experimental study.

In this research, a simulation was performed on the spillway of Makhool Dam, which was constructed on a scale of 1:50. The aim of the present work is to analyze the differences between experimental and numerical models. The velocity and flow depth results in the experimental model were compared with Makhool spillway dam 3D numerical model (case study) in order to determine the compatibility of results. The VOF method was used in a numerical model to predict two phase flows with turbulence closures, including standard K-e and RNG K-e model. The results are compared, and it was observed that there was a very excellent agreement. It was proven that Flow 3D software is effective in analyzing the hydraulic properties at a lower cost and in less time compared to the physical model.

2. METHODOLOGY

Makhool Dam is one of the under-construction projects on the Tigris River in Iraq. It is located in the northern part of the city of Baiji between the two longitudes (43°12'08"-43°38'48") east, and two latitudes (35°09'21"-35°41'19") north, on the Makhool mountain range in the Salah al-Din Governorate of Iraq as shown in (Figure 1). The Bottom Spillway Discharge (Gated) has a discharging capacity of 15297 cubic meters per second (MoWR, 2020).

2.1 Experimental study

The Experimental studies were acted on the physical model that was established inside the hydraulic laboratory, College of Engineering at Al-Mustansiriya University by (Abbas, 2002), as shown in (Figure 2). The model was created on a scale of 1:50 and the dimensions were represented according to the attached diagram (Figure 3). Hydraulic parameters of the dam such as downstream flow depth and Velocity are obtained by performing Eighty-one experiments on the models in specific places in the dam body (Abbas, 2002). The required results were measured at different times and operating conditions.

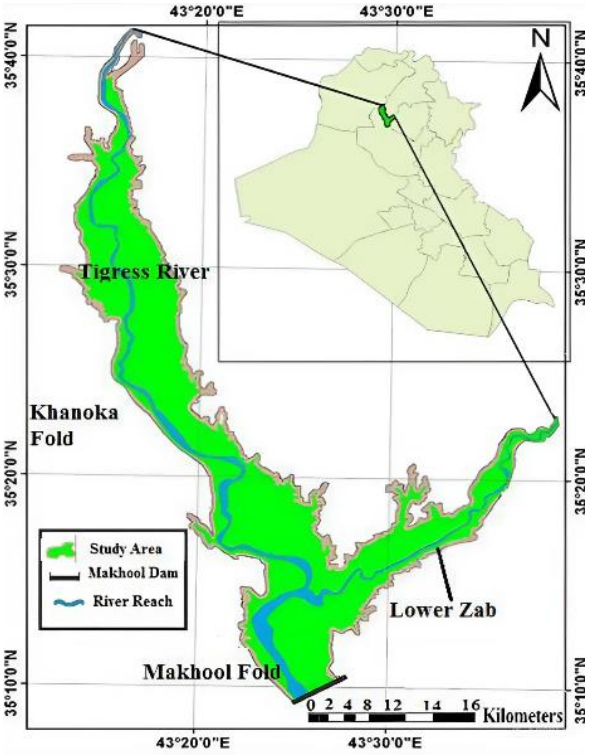

Figure 1. Makhool Dam location (Engineering Consulting Bureau of Anbar University, 2020)

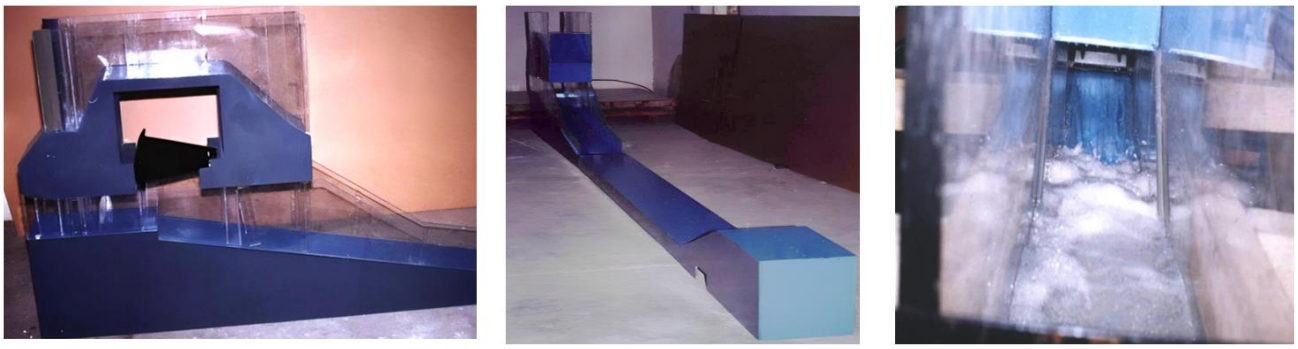

Figure 2. Physical model of for Makhool spillway (Abbas, 2002; Amen, 2002)

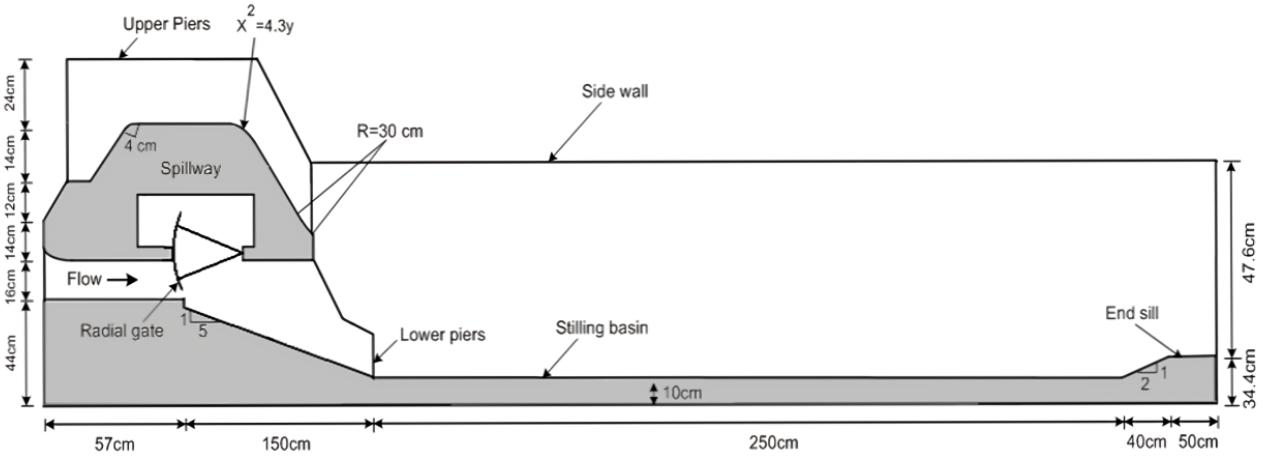

Figure 3. Cross section of Makhool spillway (Abbas, 2002)

2.2 Governing and flow equations

CFD system doing by the governing equations of fluid flow have been divided into a set of algebraic equations that are solved using computers. These equations define the conservation of mass, momentum, and energy within a fluid, accounting for factors like viscosity, turbulence, and thermal effects.

2.2.1 Mass continuity equation

It is expressed in differential form as equation (1) with its variables, which is also known as the equation for the conservation of mass within a fluid flow system.

$$\frac{V_F}{\rho c^2}\frac{\partial p}{\partial t} + \frac{\partial u A_s}{\partial x} + R\frac{\partial v A_y}{\partial y} + \frac{\partial w A_z}{\partial z} + \xi\frac{u A_x}{x} = \frac{R_{5ag}}{\rho} \quad (1)$$

Where; $\frac{V_F}{\rho c^2}\frac{\partial p}{\partial t}$ This term likely represents acoustic wave propagation, where VF is a volume of the fluid, ρ refers to fluid density, p is the pressure, and c refers to the speed of sound in the fluid. This term accounts for the rate of change of pressure over time.

$\frac{\partial u A_s}{\partial x}$ The term refers to the rate of change of the mass flow rate (uAs) to the x direction, where u is a velocity in the x-direction and As is a cross-sectional area perpendicular to the flow. This term accounts for the advection of mass in the x-x-direction.

$R\frac{\partial v A_y}{\partial y}$ This term refers to the rate of change of mass flow rate (vAy) to y direction, Ay is the cross-sectional area perpendicular to the flow, and v is the velocity in the y-direction. R seems to represent some coefficient or term related to the flow.

(R=1, ξ= 0) applied when Cartesian coordinates are to be utilized.

2.2.2 Momentum equations

The equations of motion for the fluid velocity components (u, v, w) in the three coordinate directions are the Navier-Stokes equations with some additional terms:

$$\frac{\partial u}{\partial t} + \frac{1}{V_F}\left\{u A_x \frac{\partial u}{\partial x} + v A_y R\frac{\partial u}{\partial y} + w A_z \frac{\partial u}{\partial z}\right\} - \xi\frac{A_y v^2}{x V_F} = -\frac{1}{\rho}\frac{\partial p}{\partial x} + G_x + f_x - b_x - \frac{R_{SCE}}{\rho V_F}(u - u_w - \delta u_x) \quad (2)$$

$$\frac{\partial v}{\partial t} + \frac{1}{V_F}\left\{u A_x \frac{\partial v}{\partial x} + v A_y R\frac{\partial v}{\partial y} + w A_z \frac{\partial v}{\partial z}\right\} + \xi\frac{A_y u v}{x V_F} = -\frac{1}{\rho}\left(R\frac{\partial p}{\partial y}\right) + G_y + f_y - b_y - \frac{R_{sov}}{\rho V_F}(v - v_z - \delta v_s) \quad (3)$$

$$\frac{\partial w}{\partial t} + \frac{1}{V_F}\left\{u A_x \frac{\partial w}{\partial x} + v A_y R\frac{\partial w}{\partial y} + w A_z \frac{\partial w}{\partial z}\right\} = -\frac{1}{\rho}\frac{\partial p}{\partial z} + G_z + f_z - b_z - \frac{R_{sog}}{\rho V_F}(w - w_w - \delta w_s) \quad (4)$$

Where; (G_x, G_y, G_z) refer to accelerations, (b_x, b_y, b_z) are flow losses across porous baffle plates, and (f_x, f_y, f_z) are viscous accelerations (Hirt and Sicilian,1985; Hirt and Nichols, 1981).

2.2.3 Turbulence models

Turbulence models are mathematical representations, employed in computational fluid dynamics (CFD) for the simulation of turbulent flow phenomena. Turbulence is represented by chaotic, unsteady motion and is present in many practical fluid flow situations, such as air flowing over an airplane wing or water flowing in a river. The available turbulence models vary in complexity and suitability, depending on the properties of the flow being simulated as well as the computational resources available. There are some common types:

(1) RANS (Reynolds Averaged Navier-Stokes) Models: These models are based on the Reynolds-averaged Navier-Stokes equations, where the turbulent quantities are averaged over time, RANS models include the following models (Wilcox, 1998):

(2) k-e model: This is one of the most widely used RANS models and can solve transport equations for turbulent kinetic energy (k) and its dissipation rate (ε).

(3) Spalart-Allmaras model: It is a one-equation model that solves a turbulence variable related to turbulent viscosity (Pope, 2000). As shown in equations 5, 6, and 7.

(4) The RNG Ke model (Renormalization Group): RNG Ke is according to transport equations of the Ke model equations (5, 6, 7) with different coefficients and replaced variables in equation (6) and extracted from equation (8).

(5) LES (Large Eddy Simulation): LES resolves large-scale turbulent structures explicitly while modeling the effects of small-scale turbulence. It's computationally more intensive compared to RANS but provides more accurate predictions for flows with large turbulent structures (Caughey, 2005).

(6) DNS (Direct Numerical Simulation): DNS solves the entire range of turbulent scales without any modeling. It's highly accurate but computationally

very expensive and is typically limited to academic research or small-scale simulations (Davidson, 2015).

(7) Hybrid Models: These combine elements of both RANS and LES to achieve accurate results at a reduced computational cost. Examples include Detached Eddy Simulation (DES) and Scale-Adaptive Simulation (SAS) (Versteeg and Malalasekera, 2007).

(8) Reynolds Stress Models (RSM): RSM directly models the Reynolds stresses in the flow and is more suitable for complex flows with significant streamline curvature or rotation.

(9) Select the suitable turbine model based on elements such as the characteristics of the flow (e.g., boundary layer, separated flow), the required level of accuracy, and the available computational resources. Engineers perform sensitivity analyses using different turbine models to evaluate their impact on simulation results. According to previous studies, accurate results can be obtained from k-e and The RNG Ke models is higher than the LES turbulence model result (Daneshfaraz et al., 2021).

$$\frac{\partial k}{\partial t} + \bar{u}_j \frac{\partial k}{\partial x_j} = \frac{\partial}{\partial x_j}\left[\left(v + \frac{v_T}{\sigma_k}\right)\frac{\partial k}{\partial x_j}\right] + \tau_{ij}\frac{\partial \bar{u}_i}{\partial x_j} - \varepsilon \dots\dots\dots\dots \quad (5)$$

$$\frac{\partial \epsilon}{\partial t} + \bar{u}_J \frac{\partial \varepsilon}{\partial x_j} = \frac{\partial}{\partial x_j}\left[\left(v + \frac{v_T}{\sigma_\varepsilon}\right)\frac{\partial \varepsilon}{\partial x_j}\right] + \frac{\varepsilon}{k}\left(C_{\varepsilon 1}\tau_{ij}\frac{\partial \bar{u}_i}{\partial x_j} - C_{\varepsilon 2}(\varepsilon)\right) \quad (6)$$

Therefore, the turbulent viscosity is given as:

$$v_T = C_\mu \frac{k^2}{\varepsilon} \quad (7)$$

Where; (C_{13}, C_{23}, C_μ) are constant and have the following values (1.44, 1.92, 0.09) Consecutive, (σ_k, σ_ε) are represent the Prandtl number of turbulent K and e, are have the following values (1, 1.3) respectively (Shaheed et al., 2019).

$$C^*_{\varepsilon 2} = C_{2\varepsilon} + \frac{C_\mu \mu^3\left(1-\frac{\mu}{\mu_0}\right)}{1+\beta\mu^3};\ \mu = \frac{k}{\varepsilon}\left(2S_{ij}S_{ij}\right)^{\frac{1}{2}} \quad (8)$$

2.3 Numerical model

The Makhool Dam Spillway was simulated using the FLOW 3D program. FLOW-3D is accurate, fast, and proven CFD software that solves the toughest free-surface flow problems (Flow Science, 2020).

2.3.1 Model geometry

The geometry of the physical model consists of spillway and stilling basin type 1. The numerical model was drawn in Auto-CAD 3D then exported as a STL (stereo lithography) in the Flow-3D program as shown in (Figure 4(a)).

2.3.2 Boundary and initial condition

There are ten boundary conditions which are categorized according to flow condition and spillway design, in this simulation, the boundary conditions applied to the numerical model are shown in the (Table 1) and (Figure 4(b)).

2.3.3 Physics and fluid properties

In Flow-3D many physical properties can be applied in simulation as appropriate to the design. In this research, these options enabled the gravitational non-inertial reference frame and viscosity and turbulence (Saneie et al., 2016). In gravitational non-inertial reference frame option entered into cartesian coordinates (X=0, Y=0, Z= 9.81), As for the viscosity option has been selected viscous flow with the RNG model once and with k-e in other runs. These options were used because they can Predict vortices and give greater accuracy to rotary flow. The fluid properties entered into the modeling are based on the International System of Units (SI) unit (Yusuf and Micovic, 2020), where water at a temperature of 20°C (Rahimzadeh et al., 2012), a density of 1,000 kg/m^3 (Banerjee, 2018), and a dynamic viscosity of 0.001 pa.s were chosen in the modeling (Hekmatzadeh et al., 2018).

Table 1. The boundary conditions of model

(X-min) Upstream boundary	(X-max) Downstream boundary	(Z-min, Z-max) Side boundary	(Y-min) Bottom boundary	(Y-max) Top boundary
inflow(Q)	outflow(O)	wall condition (W)	wall condition (W)	symmetry (S)

2.3.4 Mesh analysis and grid generation

Determined the Grid generation because the solutions accuracy depends on the mesh quality, using Cartesian coordinates, and entering the suitable mesh size which is equal to 0.01. The size of cells was the same in all tests as shown in (Figure 4 (c)-(d)). After selecting the size of mesh size, the Favorizer icon is rendered to view how the grid generated resolves the geometry in addition to the view of the initial fluid region as shown in (Figure 4(e)).

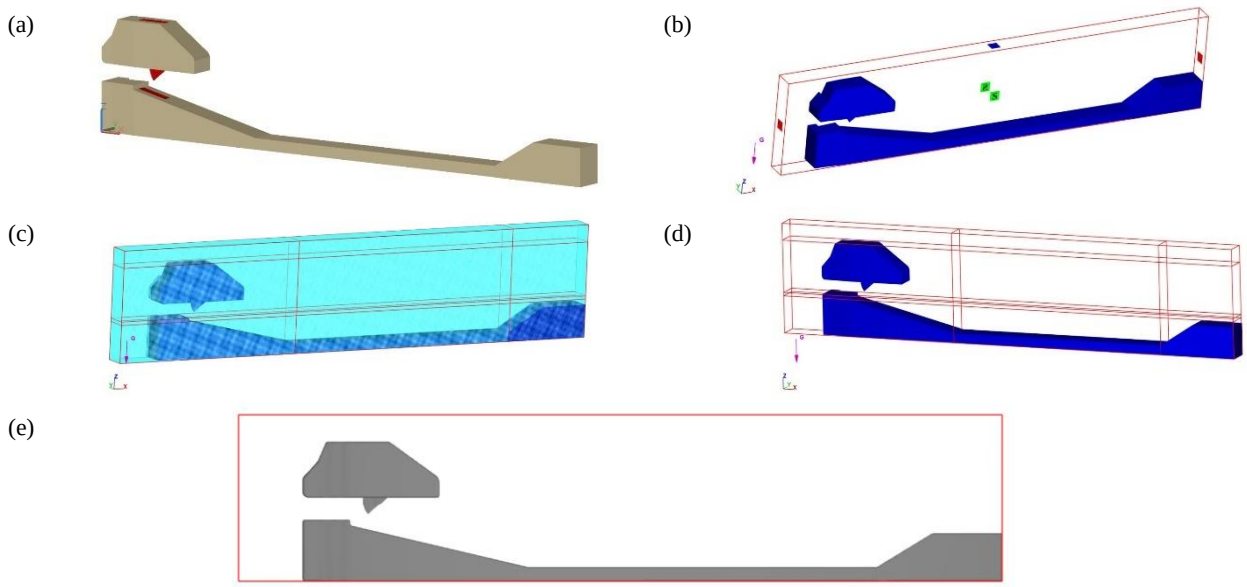

Figure 4. Numerical model: (a) model Geometry; (b) boundary condition; (c) the computational cells; (d) mesh block; (e) favorizer render

3. RESULTS AND DISCUSSION

The hydraulic models were simulated in different scenarios such as different discharges with different gate openings of the spillway based on the data of a physical model in the experimental study and then simulated by using two different equations in Flow 3D software RNG equation and k-e equation because the RNG turbulence and standard k-e models give more stable values than other models according to previous studies. As shown in Supplementary data, which shows the run of the dam for all cases with the velocity and flow water depth parameters. The results were selected after achieving steady state conditions to obtain exact values of a numerical model so the results were close to the results of the laboratory study with some slight differences that are considered acceptable. As shown in (Table 2) it shows the difference in the results and the accuracy of the program.

RMSE was calculated by:

$$\text{RMSE} = \sqrt{\frac{1}{n}\sum_{1}^{n}(y \text{ experimental - } y \text{ numerical })^2} \quad (9)$$

The values of RMSE as presented in (Table 2) indicate accuracy in CFD simulation. The simulation was run for all the indicated points, as shown in Supplementary data, which shows the accuracy of the models in the Flow 3D by the compatibility between the flow state in the physical and numerical models through the shape of the hydraulic jump.

Table 2. Numerical results of simulating Makhool dam by using Flow3D with experimental results

				RNG			KE		
G_0	Q	V_{exp}	Y_{exp}	V_{num}	Diff%	Y_{num}	V_{num}	Diff%	Y_{num}
0.15	0.083	3.28	0.11	3.12	4.878	0.115	3.21	2.134	0.112
	0.07866	3.1975	0.1025	3.1	3.049	0.106	3.125	2.267	0.105
	0.057	2.7142	0.10	2.56	5.681	0.106	2.567	5.423	0.106
0.155	0.0405	1.7743	0.11	1.6563	6.651	0.111	1.66	6.442	0.114
0.16	0.1	3.3064	0.135	3.01	8.964	0.145	3.019	8.692	0.145
	0.083	2.8614	0.1275	2.8107	1.772	0.130	2.8142	1.650	0.130
	0.07866	2.6773	0.13	2.8429	-6.185	0.122	2.71	-1.221	0.128
	0.057	2.0348	0.135	2.01	1.219	0.137	2.1	-3.204	0.131
RMSE				0.005547			0.004854		

G_0 is Gate opening (m), Q is Discharges (m^3/s), V_{exp} is Velocity in the physical model (m/s), Y_{exp} (m) is downstream flow depth in the physical model, V_{num} Velocity in the numerical model (m/s), Y_{num} (m) is downstream flow depth in the numerical model and RMSE is root mean square error (Lafta,2020; Hodson,2022), was used to measure the error in predicting simulated results by comparing them with the experimental results.

3.1 Comparison of velocity

Through Table 2, it can be seen the comparison between the results of the numerical model with experimental tests carried out by (Abbas, 2002). Three gate openings were selected for the physical model, each operated at specific discharges. The run provided positive performance especially when using the Ke turbulence model as shown in (Figure 5).

The velocity magnitudes demonstrate a high level of concordance. The difference rate percentage between the laboratory data and numerical results stands at 8.96% and 8.69% for RNG and Ke turbulence models respectively. Although there is a slight disparity between the numerical velocities and those observed in the laboratory model, this difference is considered acceptable. The levels of difference rate observed in the recorded measurements are considered to be within an acceptable range. It is postulated that the turbulent fluctuations induced by the incoming flood discharge may impact the measurement outcomes, thus serving as a plausible source of difference.

3.2 Comparison of Water Depth

Experimental results of water depth at the specified point (y1) were compared with the simulation results numerical model in Flow-3D. The simulation was run in the following cases illustrating the size of the open gates (0.16-fully gated,0.155,0.15) m, as shown in (Figure 6).

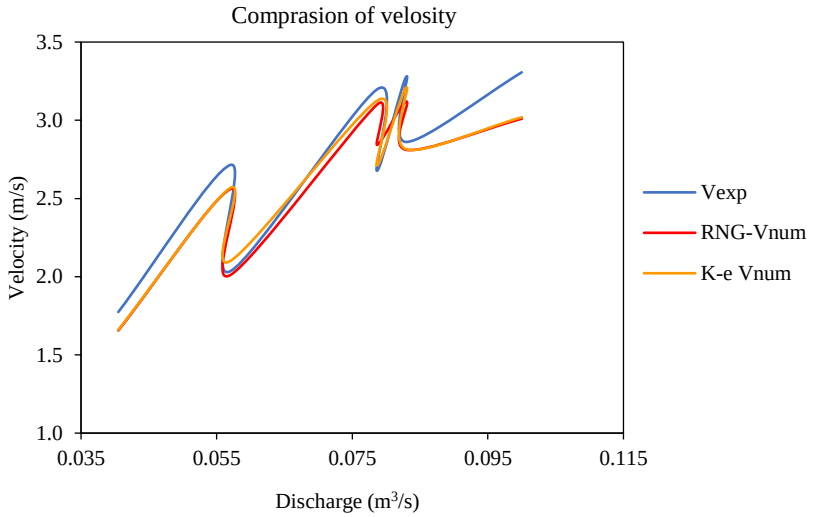

Figure 5. The result of the velocity and validation of experimental and numerical models

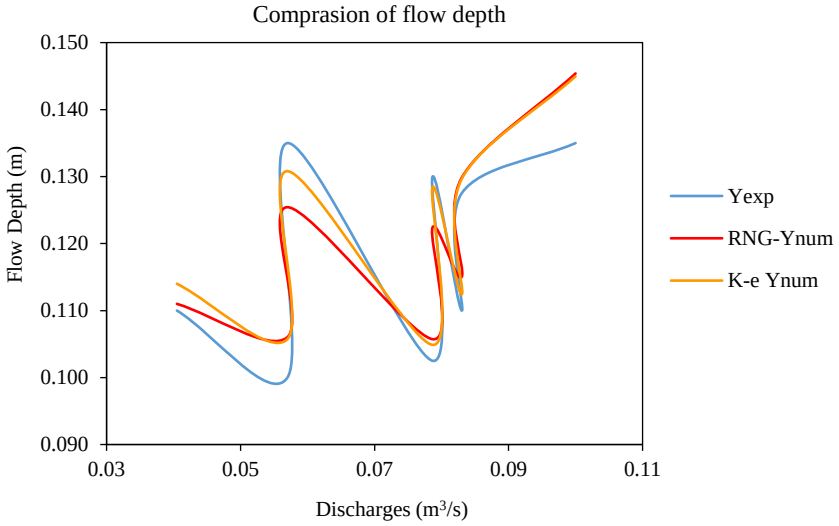

Figure 6. The result of flow depth and validation of experimental and numerical data using standard k-e and RNG turbulence models equation

4. CONCLUSION

The results derived from the research are enumerated as follows:

1. As a result of the studies in the research, it was observed that the difference rate was acceptable between the experimental and numerical analysis velocity and depth results, whether operating by RNG or Ke equation. This agreement the capability of Flow 3D software for numerical simulation of flow over a spillway. It may be more economical in many cases from physical model measurements in a hydraulic laboratory.

2. Turbulence equations effects in the flow usually caused differences in the measurements of the model. It showed that the difference in results between the turbulence models used depends on the type of flow, as the RNG equation is used for complex and unsteady flows, while the KE equation is used for stable flows, so its results are closer to reality in this type of flow.

3. The flow depth of water and velocity were measured at the location where the hydraulic jump is initiated and at a certain distance like the physical model and it was observed that there is some difference in the results but the difference in RMSE was shown to be within the permissible limit.

REFERENCES

Abbas MM. Experimental Investigation on the Hydraulic Performance of the Combined Stilling Basin at Makhool Dam [dissertation]. Baghdad, Iraq: Al-Mustansiriya University; 2002.

Amen RF. Hydraulic Performance of Large Radial Gates Installed in Closed Conduits under High Head for Makhool Dam [dissertation]. Baghdad, Iraq: Al-Mustansiriya University; 2002.

Banerjee D, Jhamnani B. CFD analysis of ogee spillway hydraulics. International Journal of Modern Trends in Engineering Research 2018;5:Article No. 79.

Caughey DA. Turbulence Modeling for Engineers: A Primer. New York, NY: Wiley; 2005.

Daneshfaraz R, Minaei O, Abraham J, Dadashi S, Ghaderi A. 3-D numerical simulation of water flow over a broad-crested weir with openings. ISH Journal of Hydraulic Engineering 2021;25(2):183-9.

Dargahi B. Experimental study and 3D numerical simulations for a free-overflow spillway. Journal of Hydraulic Engineering 2006;132(9):899-907.

Davidson PA. Turbulence: An Introduction for Scientists and Engineers. USA: Oxford University Press; 2015.

Engineering Consulting Bureau of Anbar University. Makhool Dam Project Hydraulic Study. Anbar, Iraq: Engineering Consulting Bureau of Anbar University; 2020.

Erpicum S, Tullis BP, Lodomez M, Archambeau P, Dewals B, Pirotton M. Scale effects in physical piano key weirs models. Journal of Hydraulic Research 2016;54(6):692-8.

Flow Science Inc. FLOW-3D Version 10.0 User Manual [manual]. Santa Fe, NM: Flow Science Inc.; 2020.

Hekmatzadeh AA, Papari S, Amiri SM. Investigation of energy dissipation on various configurations of stepped spillways considering several RANS turbulence models. Iranian Journal of Science and Technology, Transactions of Civil Engineering 2018;42:97-109.

Hodson TO. Root mean square error (RMSE) or mean absolute error (MAE): When to use them or not. Geoscientific Model Development 2022;15:5481-8.

Hirt CW, Nichols BD. Volume of fluid (VOF) method for the dynamics of free boundaries. Journal of Computational Physics 1981;39:201-25.

Hirt C, Sicilian J. A porosity technique for the definition of obstacles in rectangular cell meshes. Proceedings of the 4th International Conference on Numerical Ship Hydrodynamics; 1985 Sep 24-27; Washington, DC; 1985.

Jahad U, Al-Ameri R, Chua L, Das S. Investigating the effects of geometry on the flow characteristics and energy dissipation of stepped spillway using two-dimensional flow modelling. Proceedings of the 21st IAHR Asia and Pacific Division Conogress; 2018 September 2-5; Yogyakarta, Indonesia; 2018. p. 289-96.

Kocaer Ö, Yarar A. Experimental and numerical investigation of flow over ogee spillway. Water Resources Management 2020;34(13):3949-65.

Kote AS, Nangare PB. Hydraulic model investigation on stepped spillway's plain and slotted roller bucket. Engineering, Technology and Applied Science Research 2019;9(4):4419-22.

Lafta BS. Numerical Study of the Effect of Stepped Spillway on Distribution of Flow Parameters [dissertation]. Wasit, Iraq: Wasit University, College of Engineering; 2020.

Li S, Cain S, Wosnik M, Miller C, Kocahan H, Wyckoff R. Numerical modeling of probable maximum flood flowing through a system of spillways. Journal of Hydraulic Engineering 2011;137(1):66-74.

Manogaran T, Zainol MMA, Wahab MKA, Aziz MA, Zahari NM. Assessment of flow characteristics along the hydraulic physical model of a dam spillway. Journal of Civil Engineering, Science and Technology 2022;13:69-79.

Ministry of Water Resources (MoWR). The Center for Studies and Designs. Feasibility Study of Makhool Dam; 2020.

Pataki GE, Cahill JP. Guidelines for Design of Dams. Albany, New York: Division of Water, Department of Environmental Conservation; 1985.

Pereira GM. Spillway Design-Step by Step. United States: CRC Press; 2020.

Pope SB. Turbulent Flows. United Kingdom: Cambridge University Press; 2000.

Rahimzadeh H, Maghsoodi R, Sarkardeh H, Tavakkol S. Simulating flow over circular spillways by using different turbulence models. Engineering Applications of Computational Fluid Mechanics 2012;6(1):100-9.

Rajaa AI. Numerical Modeling of Flow Patterns over Spillway [dissertation]. Anbar, Iraq: University of Anbar, College of Engineering; 2020.

Shaheed R, Mohammadian A, Kheirkhah Gildeh H. A comparison of standard k-ε and realizable k-ε turbulence models in curved and confluent channels. Environmental Fluid Mechanics 2019;19(2):543-68.

Samadi-Boroujeni H, Abbasi S, Altaee A, Fattahi-Nafchi R. Numerical and physical modeling of the effect of roughness height on cavitation index in Chute Spillways. International Journal of Civil Engineering 2020;18(5):539-50.

Saneie M, SheikhKazemi J, Azhdary Moghaddam M. Scale effects on the discharge coefficient of ogee spillway with an arc in plan and converging training walls. Civil Engineering Infrastructures Journal 2016;49(2):361-74.

Sartaj M, Beirami K, Fooladgar A. Analysis of two-dimentional flow over standard ogee spillway using RNG turbulence model. Proceedings of the 7th International Congress on Civil Engineering; Tehran, Iran: Tarbiat Modares University; 2006.

Savage BM, Johnson MC. Flow over ogee spillway: Physical and numerical model case study. Journal of Hydraulic Engineering 2001;127(8):640-9.

Versteeg HK, Malalasekera W. An Introduction to Computational Fluid Dynamics the Finite Volume Method. 2nd ed. India: Pearson Education; 2007.

Wilcox DC. Turbulence Modeling for CFD. La Canada, California: DCW industries, Inc.; 1998.

Yusuf F, Micovic Z. Prototype-scale investigation of spillway cavitation damage and numerical modeling of mitigation options. Journal of Hydraulic Engineering 2020;146(2):Article No. 04019057.

Zahari NM, Zawawi MH, Sidek LM, Ng FC, Abas MA. Discrete particle method numerical simulation on the distributions of suspended particles in the flow of ogee spillway structure. Journal of Advanced Research in Fluid Mechanics and Thermal Sciences 2022;98(1):42-55.

Environment and Natural Resources Journal

Volume 23
Issue 2
2025

Using Recycled Coal Ash from Thermal Power Plants and Rice Husk Ash as Alternative Aggregates for the Manufacturing of Terrazzo Tiles

Nguyen Thi Minh Trang[1], Nguyen Thi Thanh Huong[1], and Ngo Anh Dao Ho[2*]

[1]Department of Urban Infrastructure Engineering, University of Architecture Ho Chi Minh City, Ho Chi Minh City, Vietnam
[2]Faculty of Environment and Labour Safety, Ton Duc Thang University, Ho Chi Minh City, Vietnam

ARTICLE INFO

Received: 5 Aug 2024
Received in revised: 19 Dec 2024
Accepted: 25 Dec 2024 Published online: 24 Feb 2025
DOI: 10.32526/ennrj/23/20240221

Keywords:
Fly ash/ Bottom slag/ Rice husk ash/ Terrazzo tiles/ Aggregate ratio

*** Corresponding author:**
E-mail:
hongoanhdao@tdtu.edu.vn

ABSTRACT

This study investigated the technical specifications of Terrazzo tiles manufactured using coal ash from thermal power plants and rice husk ash (RHA) to partially replace sand and cement as primary aggregates. Sample bricks with different mixed ratios of fly ash, bottom ash (slag), and RHA were produced with a hydrostatic-press machine with a standard mode of 400×400×30 mm. Our results showed that the brick density, flexural strength, and water absorption were significantly affected by the variation of fly ash and RHA content. The optimum ratio by weight of aggregate ingredients was found to be fly ash of 10%wt., RHA of 30%wt., and slag of 5%wt., accompanied by crushed stone at 55%wt. This produced brick products comparable to Terrazzo tiles, type 2, Mac 4.0. This classification satisfies the Vietnamese national standard for exterior bricks, and also is competitive with commercial quality in the local market. The reuse and recycling of waste from thermal power plants and RHA for manufacturing new construction material was thus demonstrated successfully in this study. This helps to emphasize the trend of net zero emissions, and further encourages the concept of reutilization towards sustainable development.

1. INTRODUCTION

According to statistics and estimation from The Vietnam Union of Science and Technology Associations (VUSTA), from 2025 to 2035, the quantity of waste slag generated from all coal thermal power plants in Vietnam is about 12.00-14.48 million tons of fly ash and 2.12-2.56 million tons of bottom ash (Truong, 2019). Based on the Law on Environmental Protection 2020 (Vietnam), ash and slag are encouraged to be recycled and reused as secondary building materials to reduce environmental impacts (VNA, 2020). Specifically, the ash and slag generated from the Formosa Thermal Power Plant (FTPP) in Dong Nai Province, Vietnam, have been certified as recyclable wastes due to the satisfaction of their compositions to the national standards of backfill materials and additives of cement (i.e., TCVN 12249:2018, TCVN 6882:2016) (MOC, 2017). It was reported that the heavy metal content in ash and slag was low (e.g., Hg concentration in fly ash of 0.0005 mg/L is lower than the maximum level regulated by the national standard of hazardous waste of 0.2 mg/L) (Nguyen et al., 2020). Ash and slag from thermal power plants have been investigated for different reuse purposes in the construction material industry, such as additives for cement manufacturing (Abdullah et al., 2011; Le et al., 2019), additives for concrete production (Oner et al., 2005; Teixeira et al., 2019), adobe brick (Dharek et al., 2020; Trang et al., 2021), landfill cover layer (Brännvall and Kumpiene, 2016; Shaikh et al., 2021), backfill material (Li et al., 2020; Behera et al., 2021), and reinforced construction foundations (Mohajerani et al., 2017; Pant et al., 2019; Ashfaq and Moghal, 2022). Thus, further investigation of the combination of ash and other waste materials should be carried out to explore more recycling potentials.

On the other hand, rice cultivation and production also release agricultural wastes, especially

Citation: Trang NTM, Huong NTT, Ho NAD. Using recycled coal ash from thermal power plants and rice husk ash as alternative aggregates for the manufacturing of terrazzo tiles. Environ. Nat. Resour. J. 2025;23(2):151-164. (https://doi.org/10.32526/ennrj/23/20240221)

rice husk (RH) and rice husk ash (RHA). According to the General Statistics Office of Vietnam, the total rice output in 2022 reached 42.66 million tons (GSOV, 2022). A study reported that for each ton of rice produced, there are about 200 kg of RH and 40 kg of RHA generated, which leads to considerable environmental issues (Ling and Teo, 2011). Many studies have shown the prospect of RHA application in building material manufacturing (Peng and Yang, 2016; Hossain and Islam, 2022). However, most studies focus on using RHA burned under controlled temperature and crushed to optimal size. Although the RHA obtained under these conditions can help to improve the mechanical properties and the durability of concrete (de Sensale, 2006; Giaccio et al., 2007), the crushing process leads to high cost of input material since the maximum alternative amount of RHA for cement is just about 10% (w.t.) (Talsania et al., 2015). The investigation of the raw RHA without burning or crushing to apply in construction materials production is still limited. Thus, study on the application of raw RHA as aggregates for adobe brick manufacturing is a promising approach.

Generally, adobe brick is produced through the shaping process without temperature treatment, from which its structural bonding is different from the common one. The strength of adobe brick depends on the pressure or vibration and adhesive components applied during the manufacturing. Also, the durability will be increased over time through the petrified reaction of different aggregates (Trang et al., 2021). In Vietnam, the commercial pavement brick is Terrazzo tiles - one common adobe brick type, which is produced from traditional materials through vibration or static pressing procedures. Compared with other pavement bricks, Terrazzo tiles have many advantages, including having good bearing capacity and no water retention. In terms of composition, Terrazzo tiles are concrete with a low water ratio in which mixed aggregates are pressed tightly in steel molds to form products with particular shapes. Thus, the aggregate ingredients with appropriate proportions and a proper static pressure control for brick shaping play an important role in the brick quality. Previous studies have investigated the feasibility of using industrial wastes (e.g., incineration bottom ash (Huynh et al., 2021), exhausted lime, and glazing sludge (Andreola et al., 2016), and polishing sludge (Al-Zboon et al., 2010)) as alternative raw materials in the production of building bricks and Terrazzo tiles (ceramic tiles) for pavement. Most studies successfully demonstrated that these waste materials can be used to produce Terrazzo tiles of which the transverse strength, water absorption, and tile measurements comply with national standards. However, the effects of aggregate ingredients were not examined in details. In addition, the manufacturing of Terrazzo tiles using coal ash and RHA as the main aggregates has not been studied much in Vietnam. Thus, this study is expected to expand the database for recyclable materials in the field of construction engineering and also tackle environmental issues due to the waste generation.

The objectives of this study include: (1) to determine the aggregates proportion between coal ash and RHA to produce Terrazzo tiles following the abrasion resistance, surface water absorption, and flexural strength guidelines of the Vietnamese Standard TCVN 7744:2013 on Terrazzo tiles (MOC, 2016); and (2) to evaluate the roles of coal ash and RHA to replace sand and cement in aggregate ingredients. Results obtained in this study will promote the development of advanced technology for adobe brick manufacturing using waste materials. The novelty of this study is the combination of 2 waste materials to partially replace the use of cement, which has yet to be conducted in Vietnam. This study shows significance in both environmental and economic aspects, which helps to strengthen the inevitable trend of recycling and reuse in waste treatment.

2. METHODOLOGY

2.1 Preparation of aggregates and additives

2.1.1 Aggregates

Coal ash (fly ash and bottom slag) collected from the Formosa Thermal Power Plant (FTPP) in Dong Nai Province, Vietnam, and rice husk ash (RHA) from Cai Be Rice Milling Factory in Tien Giang Province, Vietnam, were used as the main aggregates. In addition, crushed stone obtained from the Bien Hoa Stone Mine in Dong Nai Province, Vietnam, replaced the use of sand during the brick-making experiments to ensure that the strength of the bricks satisfies the national standard TCVN 7744:2013 (MOC, 2016).

(1) Coal ash: Table 1 shows the compositions and properties of fly ash and bottom slag obtained from FTPP that satisfy the national standard (i.e., TCVN 10302:2014) to serve as the alternative aggregates for the manufacturing of building materials. Also, the extracted concentrations of heavy metals are below the hazardous waste thresholds of the national standard (i.e., QCVN 07:2009) and

meet the requirements to reuse as backfill material (i.e., TCVN 12249:2018).

(2) RHA: The RHA used in this study was directly collected from the raw ash generated at the rice milling factory without the grinding process. Raw RHA with a black color and density of 2.316 g/cm^3 was then separated through a standard sieve of 0.180 mm to obtain fine RHA before mixing with other aggregates. The chemical compositions of fine RHA are presented in Table 2. It shows that the SiO_2 content occurring in RHA is very high (i.e., 91.4%) which is relatively equivalent to SiO_2 content in silica fume (i.e., >90%) - a mineral additive with high pozzolan activity commonly used in mixing concrete and mortar. This result also satisfies the TCVN 8827:2011 national standards on mineral admixture in which the SiO_2 in RHA is regulated above 85% to serve as admixtures for concrete and mortar. Thus, RHA can fill micro-holes in the brick structural matrix, improving its the durability and decreasing the amount of water used to make bricks.

Table 1. Physical-mechanical properties and chemical compositions of FTPP coal ash

Parameters		Type of coal ash		National standard TCVN 10302:2014 (*)	National standard QCVN 07:2009 (**)	National standard TCVN 12249:2018 (***)
		Fly ash	Bottom slag			
Physical-mechanical properties						
Bulk density, (g/cm^3)		0.635	0.812			
Specific gravity, (g/cm^3)		2.264	2.557	-	-	-
Residue on 0.045µm sieve, (%wt.)		19.7	37.1	<25	-	-
Humidity (%)		0.4	1.2	<3	-	-
Chemical compositions						
Content of metal oxides (% w.t.)	SiO_2	52.8	64.2	>70.0	-	-
	Al_2O_3	21.7	19.6		-	-
	Fe_2O_3	6.4	7.2		-	-
	SO_3	2.8	0.6	<3.0	-	-
	K_2O	0.4	0.8	<1.5	-	-
	Na_2O	0.7	0.1		-	-
	MgO	1.0	0.6	-	-	-
	CaO	1.9	2.1	-	-	-
	P_2O_5	1.6	1.8	-	-	-
	LOI- Loss on Ignition	10.7	3.0	<12	-	-
Heavy metal extracted concentration (mg/L)	Arsenic (As)	0.08	0.05	-	2	0.1
	Cadmium (Cd)	<0.001	<0.001	-	0.5	0.1
	Lead (Pb)	<0.001	<0.001	-	15	0.5
	Zinc (Zn)	0.002	0.002	-	250	3.0
	Nickel (Ni)	0.002	0.002	-	70	0.5
	Chromium (Cr)	0.1	0.03	-	5	0.1
	Flouride (F)	1.0	1.0	-	180	10.0

(*) TCVN 10302:2014 - Vietnam national standard for activity admixture - Fly ash for concrete, mortar, and cement.
(**) QCVN 07:2009 - Vietnam National Technical Regulation on Hazardous Waste Thresholds.
(***) TCVN 12249:2018 - Coal ash of thermal power plant using as backfill material - general requirement (Vietnam).

(3) Crushed stone: Crushed stone with an average size of <5.0 mm was used to replace sand as common material to reduce the brick manufacturing cost. The physical-mechanical properties of crushed stone are presented in Table S1 of the Supplementary Material.

2.1.2 Adhesives

(1) Cement: The adhesive partially used in this study was PCB40 cement obtained from Portland Vicem Ha Tien Cement Company with the physical-mechanical properties and chemical composition shown in Table S2 of the Supplementary Material.

Table 2. Chemical compositions of fine RHA

Chemical compositions	Content of metal oxides (%wt.)									
	SiO_2	Al_2O_3	Fe_2O_3	SO_3	K_2O	Na_2O	MgO	CaO	P_2O_5	Loss on ignition
This study	91.4	1.4	0.6	0.4	0.8	0.1	0.5	1.0	0.3	3.5
Vietnamese National Standards (TCVN 8827:2011) (*)	> 85	-	-	-	-	-	-	-	-	< 3.0

(*) TCVN 8827:2011 - Vietnamese National Standard for Highly Activity Pozzolanic Admixtures for Concrete and Mortar - Silica Fume and Rice Husk Ash (RHA)

(2) Geopolymer: Due to high SiO_2 and Al_2O_3 content in coal ash (i.e., Si:Al ratio of 2.4-3.1>2.0) and RHA (i.e., Si:Al ratio of 65.3>5.0), the mixing of these waste materials with an alkaline solution of liquid glass (sodium silicate Na_2SiO_3) can produce a geopolymer as poly (sialate-siloxo) and poly (sialate-multisilixo) (Trang et al., 2021). This geopolymer was used as an adhesive to improve the adhesion of different aggregates and reduce the PCB40 cement applied. As compared to traditional cement, this geopolymer is less harmful to the environment. The quality of the geopolymer depends on the ratio of Si/Al in the chemical composition, which is usually over 2.0 for fly ash. For this, the liquid glass (analytical grade Na_2SiO_3 solution) was obtained from a local vendor in Vietchem Chemical and Equipment Import Export Joint Stock Company, Hanoi, Vietnam. The chemical composition of the liquid glass was 13.4% Na_2O, 23.9% SiO_2, and 62.7% H_2O, with a density of 2.61 g/cm^3 and water solubility of 22.2 g/100 mL.

2.1.3 Additives

(1) Polypropylene fiber (PP fiber): The PP fiber is widely used as an additives in the building material field, such as adobe brick manufacturing and geopolymer concrete, to enhance the tensile strength and shrinkage of the product, which reduces the breakage of bricks and also increases the crack resistance of geopolymer concrete (Zhang et al., 2009). In addition, the PP fibers have low density and form good adhesion with the aggregate mixture of brick and concrete. In this study, the PP fiber with a length per diameter (l/d, mm) of 12/0.03 obtained from Zhongshan Kecheng Chemical Fiber Co. Limit in Guangdong, China, was used. Technical specifications of these PP fibers are shown in Table S3 of the Supplementary data.

(2) Pigment: The iron oxide pigment obtained from a local vendor (Ha Noi, Vietnam) was used to add color surface for Terrazzo tiles. This additive helps bricks to increase resistance to adverse environmental conditions. Technical specifications of this iron oxide pigment are shown in Table S4 of the Supplementary data.

2.2 Hydrostatic-press machine

The hydrostatic-press method was applied for the experimental bricks making in this study. The Terrazzo T-120 pressing machine from Huu Thang Construction Materials Manufacturing Co., Ltd. In Tien Giang Province, Vietnam, was used during the experiments. The technical specifications of the Terrazzo T-120 machine are shown in Table S5 of the Supplementary data.

2.3 Experimental procedure for brick making

A standard Terrazzo tile has 2 layers that are pressed and mounded together (Figure 1). The first surface layer is comprised of all aggregates (fly ash, bottom slag, RHA, and crushed stone), adhesives (cement, liquid glass), additives, and granite grains (100-gram grains in each experiment). Similar material components were added to the second bottom layer, except for granite grains and low water amounts. Water and liquid glass were mixed with the aggregate mixture to ensure the appropriate humidity, avoid the hardening reaction of aggregates, and facilitate the hydrostatic pressing process.

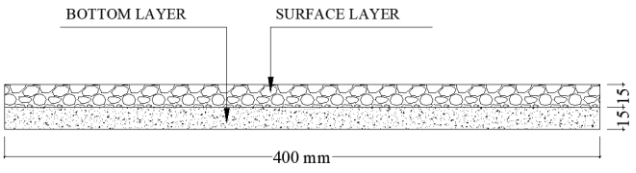

Figure 1. Structural cross-section of terrazzo tiles

According to the national standard TCVN 7744:2013 of Terrazzo tiles manufacturing (MOC, 2016), the traditional aggregate proportion is crushed stone above 60%wt., cement of 10-15%wt. The brick-making experiments E1-E5 were then designed using

20 brick samples (i.e., M1-M20) with different aggregate ingredients, as shown in Table 3. Depending on the objective of each experiment, the aggregate proportions were different. In addition, a commercial brick sample produced by Huu Thang Construction Materials Manufacturing Co., Ltd. was used as a control sample (i.e., M0 with conventional aggregates as cement, sand, and crushed stone of 15%, 25%, and 60%).

Table 3. Design of experimental Terrazzo tiles making with different aggregate ingredients

Experiment No.	Objectives	Sample No.	Aggregate ingredients						
			Fly ash (%wt.)	RHA (%wt.)	Bottom slag (%wt.)	Cement (%wt.)	Crushed stone (%wt.)	PP fiber (%/1 m^3 aggregates)	Water and liquid glass (10 mL/L)
-	Control sample	M0	Conventional aggregates as cement, sand, and crushed stone of 15%, 25%, and 60%						
E1	Determine the effects of fly ash	M1	40	Not used	Not used	0	60	Not used	Depending on each sample, a flexible amount was added to the mixing trough. The residual water (if any) was removed from the brick mold during the compression.
		M2	35			5			
		M3	30			10			
		M4	25			15			
		M5	20			20			
E2	Determine the effects of RHA	M6	Not used	40	Not used	0	60	Not used	
		M7		35		5			
		M8		30		10			
		M9		25		15			
		M10		20		20			
E3	Determine the effects of both fly ash and RHA	M11	Optimum value obtained from E1	Optimum value obtained from E2	Not used	Not used	60	Not used	
		M12							
		M13							
E4	Determine the effects of fly ash, RHA, and bottom slag	M14	Optimum value obtained from E3	Optimum value obtained from E3	5	Not used	55	Not used	
		M15			10		50		
		M16			15		45		
		M17			20		40		
E5	Determine the effects of PP fibers	M18	Optimum value obtained from E4	Optimum value obtained from E4	Optimum value obtained from E4	Optimum value obtained from E4	Optimum value obtained from E4	0.25	
		M19						0.5	
		M20						1.0	

All experiments were carried out in duplicate mode. In each experiment, all aggregate ingredients were prepared and mixed properly to obtain a homogeneous mixture, which was then added by layer into a square brick mold (400×400×30 mm) for the hydrostatic pressing step. A compressed pressure of 14 MPa was applied to achieve optimal density and compressive strength. After the pressing step, the bricks were picked up automatically from the mold by pulleys and dried at room temperature for 48 h to avoid rapid water loss. To promote the hydration process, the bricks were hydrated by soaking them in water for 24 h and storing them in at a cool temperature for 24 h.

Then, the bricks were transferred to the surface polishing and grinding process to obtain the aesthetics finish, as shown in Figure 2. After 28 days of the curing process, the brick samples were prepared for the quality testing according to TCVN 7744:2013 standards.

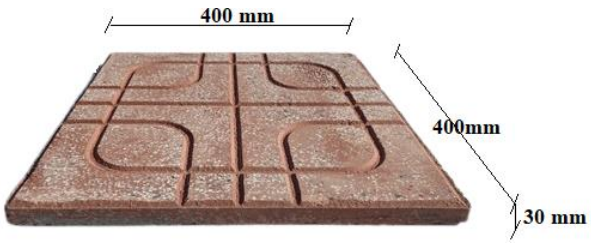

Figure 2. Typical Terrazzo tile product

2.4 Analytical methods and calculations

2.4.1 Analysis of aggregate compositions

The properties and compositions of aggregates such as coal ash and RHA were carried out using analytical grade reagents and standard methods

(APHA, 2012) in laboratory conditions. In particular, the laboratory of the Department of Civil Engineering, Ho Chi Minh City University of Architecture, Vietnam, was utilized in this study. The physical-mechanical properties and chemical compositions of fly ash and bottom slag (Table 1) were determined using the mass balance method, X-ray diffraction (XRD, model GBC Emma 3kW, Australia), and X-ray fluorescence (XRF, model 1.0 YY6312 Defan, Zhejiang Nuofan Motor Co., Ltd.) analysis. The heavy metal concentration was extracted and analyzed using an inductively coupled plasma (ICP) spectrometer (ICP-MS Model Ultramass 700, Varian - Australia).

2.4.2 Verification of brick strength

The flexural strength X (MPa) for each brick sample is determined based on the following calculation:

$$X = \frac{3.P.l}{2.b.h^2} \quad (1)$$

In which P is the destructive load of the brick sample (N); l is the distance between the two roller bearings of the testing machine (mm); b is the width of the brick sample, (mm); and h is the height of the brick sample (mm).

In this study, the electronic digital flexural strength testing machine (i.e., SKZ-10000, Hunan Zhenhua Analysis Instrument Co., Ltd., China) was employed, with l of 350 mm, corresponding to the brick dimension of 400×400 mm to facilitate the direct measurement of flexural strength of brick samples.

2.4.3 Surface water absorption $H_{m.a}$ (%) for each brick sample:

$$H_{m.a} = \frac{m_{a.c} - m_{k.s}}{m_{k.s}} \times 100\% \quad (2)$$

In which: $m_{k.s}$ is the dried weight of the brick sample (gram); $m_{a.c}$ is the total weight of the brick sample saturated by water absorbed for at least 4 days, (gram).

3. RESULTS AND DISCUSSION

3.1 Results of visual inspection of brick samples

All Terrazzo brick samples (i.e., M1-M20 with a thickness of 30 mm) obtained from experiments had a thickness difference of 0.52 mm to 1.78 mm. This difference satisfied the allowable value of $\leq \pm 2$ mm, according to TCVN 7744:2013 standards (MOC, 2016). In terms of the specific density, the results of M1-M20 varied in a range from 1.650 to 1.929 g/cm^3. This was lower than that of commercial Terrazzo tiles (M0), which normally range from 2.292 to 2.500 g/cm^3 when produced from the factory. This can be explained by the fact that the density of waste material in the experimental aggregate ingredients, which include fly ash of 2.264 g/cm^3, bottom slag of 2.557 g/cm^3, and RHA of 2.316 g/cm^3, is much lower than traditional aggregates with cement of 3.1 g/cm^3). Also, the spherical shape of fly ash, accompanied by hollow and porous particles of RHA, is different from the angular grain shape of cement and sand, which may cause the difference in internal friction between aggregate particles and affect the density of the aggregate mixture (Abdullah et al., 2011).

As for the external defects, 3 brick samples (i.e., M17, M19, and M20) were broken after pressing and could not be shaped from the mold. The others (i.e., M15, M16) were also cracked and broken partially after hydration and storage steps (Figure 3). This issue is due to the effects of aggregate ingredients: fly ash, RHA, and bottom slag. These ingredients contributed to brick samples gaining over 50-60%wt. On the other hand, Terrazzo brick samples with crushed stone was below 50 %wt., which increased their bending property and decreased their hardness. This preliminary result indicates that although poly (sialate-siloxo) and poly (sialate-multisilixo) geopolymers produced from the mixture of coal ash, RHA, and liquid glass could replace cement, the content of these alternative materials in aggregate ingredients should be limited to 50%wt. to ensure the shape and hardness of the brick samples during the pressing, hydration, and curing processes. Furthermore, the addition of a large amount of PP fiber (i.e., 0.5-1.0%/1 m^3 aggregates) to the aggregate mixture with coal ash and RHA content of 45%wt. may cause the "broken phenomenon" in M19 and M20 samples. This confirmed that the adhesion and connection of coal ash, RHA, PP fiber, and liquid glass strongly affected the shape of the brick samples, which could enhance the flexural strength but reduce the hardness of the bricks.

3.2 Technical features of control sample

The testing results of the control sample M0 showed that the flexural strength was X^7_{ave}= 3.86 MPa (after 7 days of curing) and X^{28}_{ave}= 4.53 MPa (after 28 days of curing). The results verified that the control sample with conventional aggregate is an exterior Terrazzo tile, type 2 ($X^{28}_{ave} \geq$4.0 MPa) according to national standard TCVN 7744:2013 (MOC, 2016).

The M0 sample has a bulk density of 2.390 g/cm^3 and an average surface water absorption by mass of 4.73%. These technical specifications of the M0 control sample were then used for comparison with experimental brick samples obtained from experiments E1-E5 in this study.

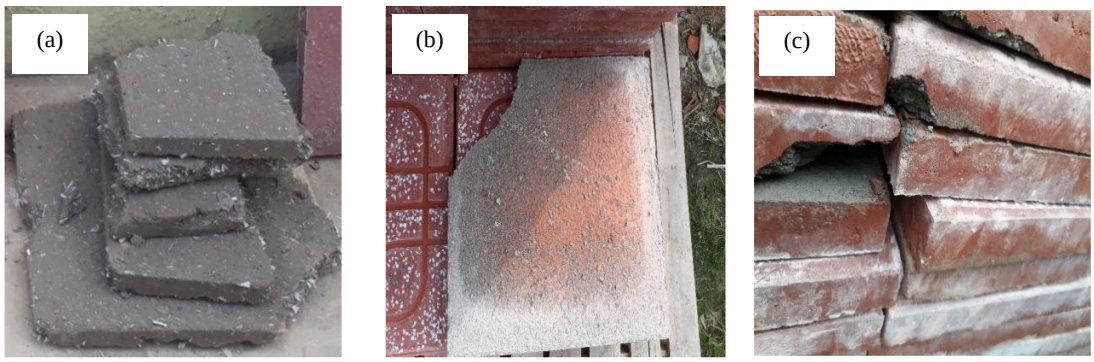

Figure 3. External defects of brick samples (a) M19, M20, (b) M16, M17, and (c) M15

3.3 Effects of aggregate ingredients on the flexural strength

3.3.1 Fly ash

Table 4 and Figure 4 present the effects of fly ash on the flexural strength, which were investigated in experiment E1 with 5 brick samples (i.e., M1-M5).

Results showed that the replacement of sand and cement by fly ash (i.e., 30-40%) in aggregate ingredients (M1, M2, M3 samples) caused a significant change in flexural strength (X_{ave}^{28}decreased from 3.82 to 3.57 MPa), corresponding to exterior Terrazzo tile type 3 (X_{ave}^{28} ≥3.5 MPa) and was lower quality as compared to M0 control samples (i.e., type 2). The lesser the fly ash, the lower the flexural strength. This was contrary to cement content. Specifically, when decreasing the fly ash and increasing the cement content, the X_{ave}^{28} decreased accordingly. The result showed that brick sample M4 and M5 did not meet the standard of exterior Terrazzo tile, type 3.

This can be explained by the fact that when the cement content in aggregate ingredients was increased, the pozzolan reaction occurred rapidly, causing more C-S-H products to be formed during the hydration of cement. In contrast, for fly ash, the C-S-H products are created slowly in the early days since the formation rate of poly (sialate-siloxo) geopolymer is faster than the pozzolan reaction rate (Phuong and Hien, 2021). Thus, the maximum cement content in aggregates should be 10%wt.

On the other hand, the improvement of flexural strength along with the increase of fly ash may be due to the spherical particle shape of fine fly ash, which helped to retain water and avoid the clumping of cement particles, leading to the increase of plasticity of the aggregate mixture and reducing water demand (CESTI-DOST, 2019). Accordingly, the minimum fly ash content to serve as aggregates for making of Terrazzo tile, type 3, with brick strength grade M 3.5, was determined to be 30%.

3.3.2 RHA

In experiment E2, the fly ash was replaced by RHA for making brick samples M6-M10. The flexural strength results of these samples are presented in Table 5 and Figure 5.

Table 4. Effects of fly ash content on the flexural strength of Terrazzo brick samples

Sample No.	Aggregate ingredients			Flexural strength X_{ave}^{7} (MPa)	Flexural strength X_{ave}^{28} (MPa)	Bulk density (g/cm^3)	Brick strength grade[(a)] (MPa)	Brick type[(a)]
	Fly ash (%wt.)	Cement (%wt.)	Crushed stone (%wt.)					
M1	40	0	60	3.27	3.82	1.650	M 3.5	Exterior Terrazzo tile, type 3
M2	35	5	60	2.98	3.63	1.691	M 3.5	
M3	30	10	60	2.89	3.57	1.733	M 3.5	
M4	25	15	60	2.71	3.46	1.775	-	-
M5	20	20	60	2.56	3.36	1.817	-	-

[(a)]Brick strength grade and brick type were determined based on the flexural strength after 28 days of curing, according to national standard TCVN 7744:2013.

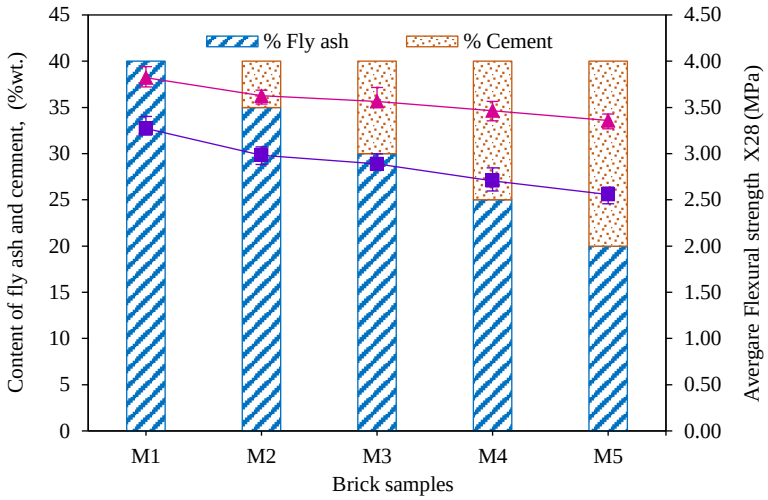

Figure 4. Change of flexural strength of brick samples with different fly ash and cement contents

Table 5. Effects of RHA content on flexural strength of Terrazzo brick samples

Sample No.	Aggregate ingredients			Flexural strength X^{7}_{ave} (MPa)	Flexural strength X^{28}_{ave} (MPa)	Bulk density (g/cm^3)	Brick strength grade[a] (MPa)	Brick type[a]
	Fly ash (%wt.)	Cement (%wt.)	Crushed stone (%wt.)					
M6	40	0	60	3.49	4.17	1.670	M 4.0	Exterior Terrazzo tile, type 2
M7	35	5	60	3.53	4.12	1.710	M 4.0	
M8	30	10	60	3.28	4.05	1.749	M 4.0	
M9	25	15	60	3.11	3.99	1.788	M 3.5	Exterior Terrazzo tile, type 3
M10	20	20	60	3.00	3.92	1.827	M 3.5	

[a] Brick strength grade and brick type were determined based on the flexural strength after 28 days of curing, according to national standard TCVN 7744:2013

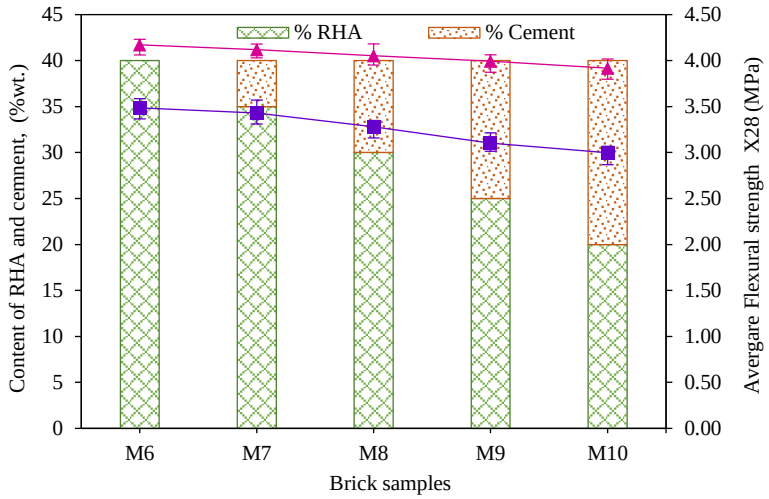

Figure 5. Change of flexural strength of brick samples with different RHA contents

The study found that although the brick samples M6, M7, and M8 could satisfy the exterior Terrazzo tile, type 2, their flexural strength was lower than that of M0. However, the bulk density and flexural strength of brick samples made from RHA in brick samples M6-M10 (Figure 7) were better than those made from FTPP fly ash in brick samples M1-M5 in Table 4 and Figure 4 under the same experimental conditions. This indicates the feasibility of both fly ash and RHA to replace sand and cement for brick making, and RHA was shown to be more effective than fly ash.

This is due to the higher specific density of RHA with 2.316 g/cm^3) as compared to fly ash with 2.264 g/cm^3). Furthermore, RHA particles with a

hollow and porous structure can show a higher ability to absorb water than round-ball-shaped fly ash. Moreover, the SiO_2 content in RHA of about 92% is higher than that found in FTPP fly ash with 52.8%), which helped to produce better technical specifications in RHA-brick samples, as compared to fly ash-products.

In summary, with the aims to produce the exterior Terrazzo tile with the brick strength grade of M 3.5-M 4.0, the fly ash and RHA can be used as aggregates with the content of 30-40%wt., accompanied by the appropriate cement of <10%wt. and crushed stone of at least 60%wt.

3.3.3 Mixture of fly ash and RHA

Based on the results of experiment E1 and E2, the brick samples M1 and M6 were used as reference samples to adjust the mixing ratio of fly ash and RHA in the aggregate ingredients of brick samples M11-M13 in experiment E3. The flexural strength results of M11-M13 are presented in Table 6 and Figure 6 below.

Results showed that when the fly ash and RHA with a total content of 40%wt. were used to replace cement in aggregates of brick samples M11-M13, the flexural strength X_{tb}^{28} of the brick samples was proportional to the RHA content, but inversely proportional to the fly ash content. Sample M13 with the ratio of fly ash and RHA of 10:30%wt. was chosen as the optimum mixing ratio to produce Terrazzo tile, type 2 (M 4.0). The aggregate ratio of M13 was then used as a reference sample for further experiments.

Table 6. Effects of fly ash and RHA mixture on flexural strength of Terrazzo brick samples

Sample No.	Aggregate ingredients			Flexural strength X_{ave}^{7} (MPa)	Flexural strength X_{ave}^{28} (MPa)	Bulk density (g/cm^3)	Brick strength grade[(a)] (MPa)	Brick type[(a)]
	Fly ash (%wt.)	Cement (%wt.)	Crushed stone (%wt.)					
M1 (reference sample)	40	0	60	3.27	3.82	1.650	M 3.5	Exterior Terrazzo tile, type 3
M11	30	10	60	3.29	3.93	1.655	M 3.5	
M12	20	20	60	3.31	3.96	1.660	M 3.5	
M13	10	30	60	3.38	4.02	1.665	M 4.0	Exterior Terrazzo tile, type 2
M6 (reference sample)	0	40	60	3.49	4.17	1.670	M 4.0	

[(a)] Brick strength grade and brick type were determined based on the flexural strength after 28 days of curing, according to national standard TCVN 7744:2013

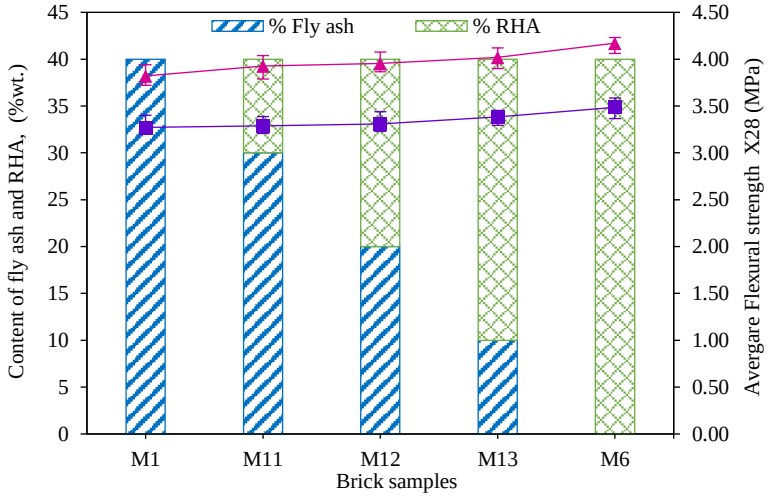

Figure 6. Change of flexural strength of brick samples with different fly ash and RHA contents without cement

3.3.4 Bottom ash (slag)

In order to investigate the feasibility of bottom ash (slag) for Terrazzo tile making, the experiment E4 was designed to partially replace the crushed stone content with slag (i.e., 5-20%wt.) in samples M14-M17. The analysis of brick samples quality is presented in Table 7 and Figure 7.

Unfortunately, the brick samples M15, M16, and M17 were broken after the hydraulic pressing and hydration process. This is due to the decrease of crushed stone (i.e., <55%wt.) and the replacement of slag (i.e., >5%wt.) in the experimental aggregates. Thus, it is believed that the maximum content of slag in aggregates should be 5% to avoid external defects during the brick shaping. The results obtained in this experiment E4 also confirmed that the high content of SiO_2 in the slag of 64.2%, as compared to that in fly ash of 52.8% in Table 1, may help to form the geopolymer adhesives poly (sialate-silixo), which enhances the flexural strength of brick samples. However, unburned coal components in FTPP bottom slag without pre-treatment by the ash separation method may cause some changes in the volume of the hydrated product during the solidification (CESTI-DOST, 2019).

Table 7. Effects of bottom ash (slag) on the flexural strength of Terrazzo brick samples.

Sample No.	Aggregate ingredients			Flexural strength X^{7}_{ave} (MPa)	Flexural strength X^{28}_{ave} (MPa)	Bulk density (g/cm^3)	Brick strength grade[(a)] (MPa)	Brick type[(a)]
	Fly ash (%wt.)	Cement (%wt.)	Crushed stone (%wt.)					
M13 (reference sample)	10	30	0	60	3.38	4.02	1.650	Exterior Terrazzo tile, type 2
M14	10	30	5	55	3.52	4.26	1.731	
M15	10	30	10	50	Not analyzed	Not analyzed	1.797	External defects
M16	10	30	15	45	Not analyzed	Not analyzed	1.863	
M17	10	30	20	40	Not analyzed	Not analyzed	1.929	

[(a)] Brick strength grade and brick type were determined based on the flexural strength after 28 days of curing, according to national standard TCVN 7744:2013.

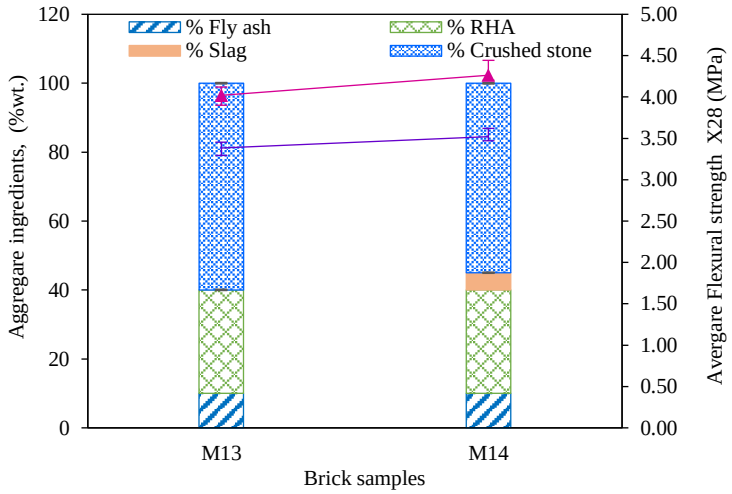

Figure 7. Effects of bottom ash (slag) on the change of flexural strength of brick samples

3.3.5 Polypropylene fiber (PP fiber)

The study showed that the addition of PP fiber to aggregate ingredients could help to improve the flexural strength of adobe bricks (Trang et al., 2021). In experiment E5, brick samples M18-M20 were prepared with the PP fiber of 0.25-1.00% to determine its effects on the Terrazzo tile quality.

Results confirmed that a small amount of PP fiber (i.e., 0.25%/1 m^3 aggregates) in sample M18 helped to increase slightly the flexural strength (i.e., 4.28 MPa), as compared to sample M14 without PP fiber (i.e., 4.26 MPa). However, when the PP fiber amount was increased (i.e., 0.5 and 1%/1 m^3 aggregates) in the samples M19 and M20, external

defects were observed visually in brick samples, as described in section 3.1. This can be explained by the fact that the addition of PP fiber leads to the increase of water content in aggregate material, which causes a pliable state and difficulty in freezing brick samples. In summary, the PP fiber did not significantly improve the Terrazzo tile strength; in contrast, the excess amount of PP fiber used in aggregate ingredients can destroy the shaping and freezing of products. Therefore, this study suggests that PP fiber should not be used as an aggregate for the manufacturing of Terrazzo tile.

Table 8. Effects of PP fiber on flexural strength of Terrazzo brick samples

Sample No.	Aggregate ingredients			Flexural strength X_{ave}^{7} (MPa)	Flexural strength X_{ave}^{28} (MPa)	Bulk density (g/cm^3)	Brick strength grade[(a)] (MPa)	Brick type[(a)]
	Fly ash (%wt.)	Cement (%wt.)	Crushed stone (%wt.)					
M14	10	30	5	55	0	3.52	4.26	Exterior Terrazzo tile, type 2
M18	10	30	5	55	0.25	3.53	4.28	
M19	10	30	5	55	0.5	Not analyzed	Not analyzed	External defects
M20	10	30	5	55	1	Not analyzed	Not analyzed	

[(a)] Brick strength grade and brick type were determined based on the flexural strength after 28 days of curing, according to national standard TCVN 7744:2013

3.4 Evaluating the water absorption of brick samples

The water absorption of adobe brick is an important factor affecting the absorption and adhesion of bricks and mortar during construction. It also indirectly reflects the permeability of bricks. Therefore, it is related to the chemical corrosion resistance of bricks (CESTI-DOST, 2019). Therefore, the water absorption requirement of Terrazzo tiles must not exceed 6% according to the Vietnam national standard TCVN 7447-2013 (MOC, 2016).

According to the results of experiment E1-E5, brick samples M1, M6, M13, M14, and M18 were chosen to determine the surface water absorption. The results are presented in Figure 8.

Results indicated that the surface water absorption of experimental Terrazzo samples varied in a range of 4.90-6.22%, which is higher than that of control sample M0 (i.e., 4.73%, section 3.2). Most brick samples satisfied the requirement of water absorption (i.e., <6%) of the national standard, except the sample M18 (i.e., 6.22%) due to the addition of PP fiber. The PP fiber may reduce the condensed structure of brick samples and form more mini-pores, which increases the surface water absorption.

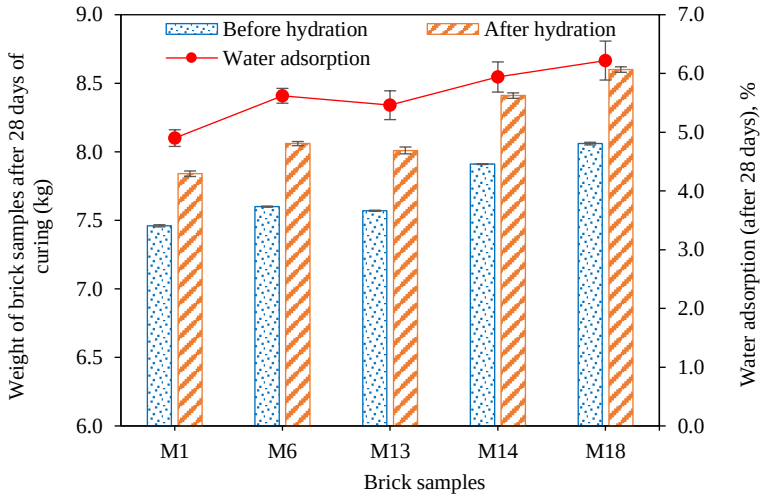

Figure 8. Changes of water absorption with different aggregate ingredients of brick samples

3.5 Evaluation of economic efficiency

In order to evaluate the economic efficiency obtained in this study, the manufacturing costs of samples M1, M6, M13, and M14 were analyzed and compared with the market price of the control sample

M0. The cost analysis is based on the actual price applied during the experiment.

Table 9 indicates that the manufacturing cost of each brick sample obtained in this study was comparable and competitive with the commercial product. Specifically, the cost of a brick sample was about 0.375-0.391 USD/ 01 sample, while the market price of a brick product from Huu Thang Construction Materials Manufacturing Co., Ltd. (Tien Giang Province, Vietnam) is currently 0.388 USD/01 brick piece. This finding raises the feasibility, applicability, and price competitiveness of brick samples produced in this study, which also confirms the economic benefits of recycling of waste from thermal power plants and rice milling factories.

Table 9. Cost analysis for Terrazzo tile manufacturing

Sample o.	Cost unit (USD/01 brick piece)						References
	Material	Labour	Electricity	Water	Depreciation of machinery and equipment	Total price	
M0	0.207	0.086	0.051	0.0031	0.029	0.388	Market price
M1	0.212	0.086	0.051	0.0015	0.029	0.391	This study
M6	0.194			0.0025		0.375	
M13	0.198			0.0019		0.379	
M14	0.211			0.0021		0.391	

4. CONCLUSION

This study was successful in demonstrating the feasibility of using coal ash from thermal power plants and rice husk ash to partially replace sand and cement for the manufacturing of Terrazzo tiles. The study also confirmed that the flexural strength, surface water absorption, and shaping and freezing of brick products were affected significantly by the mixing ratio of fly ash and RHA as alternative aggregates. Specifically, the brick samples prepared with RHA showed better flexural strength but higher bulk density and waster absorption, as compared to samples using fly ash. To achieve the quality of Terrazzo tiles (i.e., type 2, Mac 4.0, or type 3, Mac 3.5, according to national standard TCVN 7747:2013), the aggregate ingredients included the followings: (1) Fly ash content should not exceed 40%wt. and the optimum value was 10%wt.; (2) RHA should not be higher than 40%wt. and the optimum value was 30%wt.; and the highest content of bottom ash (slag) was 5%wt. In contrast, the addition of PP fiber as aggregates did not improve the quality of brick samples but destroyed the shaping and freezing of products. Thus, PP fiber was not encouraged to serve as an additive of aggregates for Terrazzo tiles manufacturing.

The consideration of economic aspects also showed the equivalence and competitiveness between the experimental brick samples obtained in this study and commercial products being distributed in the local market. This result confirmed again the feasibility of reuse and recycling of coal ash and RHA to eliminate the environmental pollution effects and then create a new and eco-friendly construction material, which adapts to the trend toward the sustainable development.

Recommendations

The coal ash and RHA employed in this study were raw materials obtained from the local factory without any step for pretreatment of unburned coal components. Thus, the quality of brick products may be affected (i.e., the brick strength grade of Mac 4.0 and type 2). Therefore, it is recommended that an activation process of raw coal ash before using it as aggregates for brick making should be investigated to enhance the flexural strength and achieve a higher brick strength grade (i.e., X_{ave}^{28} >5.0 MPs). Furthermore, the microstructural and morphological characterization of brick products using SEM, XRD, and XRF techniques is suggested to be carried out in future studies to obtain a deeper understanding of brick characteristics and demonstrate their practical applications in brick making. Moreover, advanced analysis to measure the adhesion force among different types of waste should be carried out to provide a better understanding of the effects of adhesion on the brick shaping, flexural strength, and surface water absorption.

ACKNOWLEDGEMENTS

The authors would like to acknowledge the technical support from the Department of Urban

Infrastructure Engineering, Ho Chi Minh City University of Architecture.

SUPPLEMENTARY DATA

Table S1. Physical-mechanical properties of crushed stone

Table S2. Physical-mechanical properties and chemical composition of PCB40 cement

Table S3. Technical specifications of PP fibers

Table S4. Technical specifications of iron oxide pigment

Table S5. Technical specifications of Terrazzo T-120 hydrostatic-press machine

REFERENCES

Abdullah MMA, Hussin K, Bnhussain M, Ismail KN, Ibrahim WMW. Mechanism and chemical reaction of fly ash geopolymer cement-a review. International Journal of Pure and Applied Sciences and Technology 2011;6(1):35-44.

Al-Zboon K, Tahat M, Abu-Hamatteh ZSH, Al-Harahsheh MS. Recycling of stone cutting sludge in formulations of bricks and terrazzo tiles. Waste Management and Research 2010;28(6):568-74.

Andreola F, Barbieri L, Lancellotti I, Leonelli C, Manfredini T. Recycling of industrial wastes in ceramic manufacturing: State of art and glass case studies. Ceramics International 2016;42(12):13333-8.

American Public Health Association (APHA). Standard Methods for the Examination of Water and Wastewater. Washington, DC, USA: American Public Health Association; 2012.

Ashfaq M, Moghal AAB. Cost and carbon footprint analysis of flyash utilization in Earthworks. International Journal of Geosynthetics and Ground Engineering 2022;8(2):Article No. 21.

Behera SK, Mishra DP, Singh P, Mishra K, Mandal SK, Ghosh CN, et al. Utilization of mill tailings, fly ash and slag as mine paste backfill material: Review and future perspective. Construction and Building Materials 2021;309:Article No. 125120.

Brännvall E, Kumpiene J. Fly ash in landfill top covers: A review. Environmental Science: Processes and Impacts 2016; 18(1):11-21.

Center for Statistics and Science and Technology Information, Department of Science and Technology (CESTI-DOST). The Trend of Using Thermal Ash and Slag in the Production of Construction Materials. Vietnam: Center for Statistics and Science and Technology Information, Department of Science and Technology of Ho Chi Minh City; 2019.

de Sensale GR. Strength development of concrete with rice-husk ash. Cement and Concrete Composites 2006;28(2):158-60.

Dharek MS, Sreekeshava K, Vengala J, Pramod K, Sunagar P, Shivaprakash M. Experimental investigations on utilization of bagasse ash in adobe bricks. Select Proceedings of the International Conference on Civil Engineering Trends and Challenges for Sustainability (CTCS 2020); 2020 Dec 22-23; Karkala: India; 2020.

Giaccio G, de Sensale GR, Zerbino R. Failure mechanism of normal and high-strength concrete with rice-husk ash. Cement and Concrete Composites 2007;29(7):566-74.

General Statistics Office of Vietnam (GSOV). Report on agricultural, forestry and fishery production in 2022. Vietnam: General Statistics Office of Vietnam; 2022.

Hossain Z, Islam KT. Prospects of Rice Husk Ash as a Construction Material. Elsevier; 2022.

Huynh TP, Phan HP, Pham VH, Ngo VA, Luu HT. Utilization of waste incineration bottom ash as fine aggregate in the production of terrazzo tiles for pavement. Proceedings of the 2nd International Conference on Sustainable Civil Engineering and Architecture (ICSCEA 2021); 2021 Oct 30; Ho Chi Minh City: Vietnam; 2021.

Le TH, Park DW, Park JY, Phan TM. Evaluation of the effect of fly ash and slag on the properties of cement asphalt mortar. Advances in Materials Science and Engineering 2019; 2019(1):Article No. 1829328.

Li M, Zhang J, Li A, Zhou N. Reutilisation of coal gangue and fly ash as underground backfill materials for surface subsidence control. Journal of Cleaner Production 2020;254:Article No. 120113.

Ling I, Teo D. Reuse of waste rice husk ash and expanded polystyrene beads as an alternative raw material in lightweight concrete bricks. International Journal of Chemical and Environmental Engineering 2011;2(5):328-32.

Ministry of Construction (MOC). Vietnam National Standard of Terrazzo Bricks TCVN 7744-2013. Vietnam: Ministry of Construction; 2016.

Ministry of Construction (MOC). Instructions on Using Ash and Slag of Formosa Thermal Power Plant on the Market and Putting it into Use as Raw Materials for the Production of Building Materials - CV 916/BXD-VLXD. Vietnam: Ministry of Construction; 2017.

Mohajerani A, Lound S, Liassos G, Kurmus H, Ukwatta A, Nazari M. Physical, mechanical and chemical properties of biosolids and raw brown coal fly ash, and their combination for road structural fill applications. Journal of Cleaner Production 2017;166:1-11.

Nguyen, Lam VT, Ngo HX, Van P, Dang CA H, Vu DK. Effect of fly ash on the strength of cement paste at early age. Journal of Mining and Earth Sciences 2020;61(6):10-8.

Oner A, Akyuz S, Yildiz R. An experimental study on strength development of concrete containing fly ash and optimum usage of fly ash in concrete. Cement and Concrete Research 2005;35(6):1165-71.

Pant A, Ramana G, Datta M, Gupta SK. Coal combustion residue as structural fill material for reinforced soil structures. Journal of Cleaner Production 2019;232:417-26.

Peng G, Yang J. Influence of rice husk ash on the properties of concrete: A review. 2016 International Forum on Energy, Environment and Sustainable Development, Atlantis Press; 2016.

Phuong T, Hien T. Experimental study on manufacturing of adobe bricks from slag and fly ash of Nghi Son thermal power plant. Vietnam Environment Administration Magazine 2021;4:39-41.

Shaikh J, Bordoloi S, Leung AK, Yamsani SK, Sekharan S, Rakesh RR. Seepage characteristics of three-layered landfill cover system constituting fly-ash under extreme ponding condition. Science of the Total Environment 2021;758:Article No. 143683.

Talsania S, Pitroda J, Vyas CM. Effect of rice husk ash on properties of pervious concrete. International Journal of

Advanced Engineering Research and Studies 2015;296:Article No. 299.

Teixeira ER, Camões A, Branco F. Valorisation of wood fly ash on concrete. Resources, Conservation and Recycling 2019;145:292-310.

Trang NTM, Ho NAD, Babel S. Reuse of waste sludge from water treatment plants and fly ash for manufacturing of adobe bricks. Chemosphere 2021;284:Article No. 131367.

Truong DN. Ash and ash use of coal-fired power plants. Proceedings of the Workshop on Environmental Protection in Mining, Processing and Use of Coal, Minerals and Petroleum; 2019 Aug 10; Khanh Hoa: Vietnam; 2019.

Vietnam Assemmbly (VNA). Law on Environmental Protection. Vietnam: The National Assembly of the Socialist Republic of Vietnam; 2020.

Zhang Zh, Yao X, Zhu Hj, Hua Sd, Chen Y. Preparation and mechanical properties of polypropylene fiber reinforced calcined kaolin-fly ash based geopolymer. Journal of Central South University of Technology 2009;16(1):49-52.

Environment and Natural Resources Journal

Volume 23
Issue 2
2025

Performance and Heavy Metal Leaching Behavior of Bituminous Fly Ash-Based Geopolymer in Aggressive Environments

Parichat Muensita[1], Suwimol Asavapisit[1*], and Rungroj Piyaphanuwat[2]

[1]Environmental Technology Program, School of Energy, Environment and Materials, King Mongkut's University of Technology Thonburi, Bangkok, Thailand
[2]Innovative Environmental Management and Smart Construction Materials Laboratory Ratchaburi Learning Park, King Mongkut's University of Technology Thonburi, Ratchaburi, Thailand

ARTICLE INFO

Received: 17 Jun 2024
Received in revised: 2 Jan 2025
Accepted: 8 Jan 2025
Published online: 28 Feb 2025
DOI: 10.32526/ennrj/23/20240170

Keywords:
Geopolymer/ Bituminous fly ash/ Solidification/ Heavy metal/ Leaching test

*** Corresponding author:**
E-mail: suwimol.asa@kmutt.ac.th

ABSTRACT

This article investigates the performance of a geopolymer synthesized from bituminous fly ash (BFA) activated with sodium hydroxide. The BFA-based geopolymer (BFAG) exhibited high mechanical strength and a densified microstructure. The optimal SiO_2/Al_2O_3 and Na_2O/SiO_2 molar ratios were found to be 3:1 and 0.2, respectively, yielding a 28-day compressive strength of 9.65 MPa. The inclusion of 30wt.% of a PS material containing heavy metals led to a substantial reduction in strength by 56% and 73% compared to samples with the SiO_2/Al_2O_3 molar ratio of 2:1 and 3:1, respectively, at 28 days. The ability of the BFAG matrix to contain 30wt.% PS was evaluated using a waste extraction test (WET). The leaching behavior of heavy metals from the BFAG matrix was assessed with three aggressive leachants: sodium citrate, sodium acetate, and synthetic acid rain. Results showed that, under exposure to these leachants, the leached concentrations of Cr, Fe, and Zn from samples with the SiO_2/Al_2O_3 ratio of 3:1 were lower than those from samples with the 2:1 ratio, with concentrations ranging from 0.32-1.73, 3.07-6.67, and 152-284 mg/L, respectively. Despite exposure to harsh conditions, the BFAG matrix effectively immobilized over 99% for Cr and Fe and Zn, except when exposed to sodium citrate which only retained 98.5% of Zn. BFAG can be used to treat heavy metal and heavy metal-contaminated sludge. This matrix reduces environmental exposure, thereby decreasing heavy metal leaching into the environment before safe disposal in landfills. BFAG can also be used as a cement substitute in the solidified process, which lowers treatment costs and reduces cement consumption. It can decrease carbon dioxide emissions from cement production.

1. INTRODUCTION

Geopolymers are green polymeric materials formed by the polycondensation of silica and alumina precursors. Geopolymerization reactions under alkali activation of solid aluminosilicate materials produce amorphous to semi-crystalline three-dimensional aluminosilicate networks, having cementitious properties and a strength level comparable to those of traditional cement. Moreover, the advantage of a small impact on climate change has caused these geopolymeric materials to receive considerable attention as substitute cementitious binders for cement in different applications including construction materials and waste treatment.

In environmental work, the geopolymer matrix has become widely used to immobilize heavy metal containing wastes. Most heavy metals are toxic and having amphoteric characteristics. They are readily soluble and widely distributed in the environment, causing problems due to mismanagement worldwide. To prevent the release of these toxic metals, the most common treatment method is to stabilize the toxicity

Citation: Muensita P, Asavapisit S, Piyaphanuwat R. Performance and heavy metal leaching behavior of bituminous fly ash-based geopolymer in aggressive environments. Environ. Nat. Resour. J. 2025;23(2):165-175. (https://doi.org/10.32526/ennrj/23/20240170)

and mobility of these metals and then contain them within an impermeable solidified matrix prior to disposal in the landfills. With increasing concern regarding sustainable development, geopolymers have been introduced as solidification binders with potential properties to control the release of toxic metals into the environment (Teixeira et al., 2011; Lombi et al., 2010; Tian et al., 2022).

Several studies have investigated the mechanical, physical, chemical, and microstructure of geopolymers related to the immobilization of heavy metal-containing waste (Provis and Deventer, 2009; Waijarean et al., 2017; Xia et al., 2020; Sun et al., 2022). Compressive strength of geopolymer under different conditions around 25-105 MPa at 28 days (Cong and Cheng, 2021). In terms of microstructure, the ^{27}Al spectra indicate a mixture of four-, five-, and six-fold coordinated Al-O units. (Van Jaarsveld and Van Deventer, 1999; Waijarean et al., 2017) Aluminosilicate materials from industrial by-products or residues have also been reported to be used as heavy metal-immobilizing agents. These waste-derived starting materials include coal fly ash (Silva et al., 2007; Duxson et al., 2005; Xia et al., 2020; Castillo et al., 2022; Su et al., 2023), water treatment residue (Aly et al., 2008; Lombi et al., 2010; Waijarean et al., 2017), metakaolin (Cheng et al., 2015), and red mud (Sun et al., 2022). The performance of heavy metal immobilization varies to a large extent on the chemical compositions (Si/Al) of the starting raw materials, types and compositions of alkali (Na_2O/SiO_2) activators, curing conditions, speciation of heavy metals, types of leaching solutions and leaching conditions (Zhang et al., 2008; Zheng et al., 2010; Waijarean et al., 2017; Xia et al., 2020; Sun et al., 2022).

The effects of alkaline dosage and the Si/Al ratio on the immobilization of heavy metals in municipal solid waste incineration fly ash-based geopolymers have been explored (Van Jaarsveld and Van Deventer, 1999). A geopolymer with the highest strength and the lowest leachable fraction of Cr, Cu, and Zn was obtained at an intermediate alkaline activator dosage of Na/municipal solid wastes incineration (MSWI) fly ash = 2.8 mol/kg and Si/Al molar ratio = 2.0. For the effect of Si/Al, the leachable fraction of Cr and Cu decreased with an increasing Si/Al ratio, while Zn had its lowest point at an intermediate Si/Al ratio. Various studies have shown that geopolymers exhibit better immobilization performance on MSWI fly ash than Portland cement. This is because active aluminosilicates in MSWI fly ash participate in the geopolymerization reaction, generating new phases such as Friedel's salts ($3CaO{\cdot}Al_2O_3{\cdot}CaCl_2{\cdot}10H_2O$) and hydrocalumite ($Ca_2Al(OH)_6Cl_2H_2O$). Consequently, fly ash-based geopolymers effectively encapsulate heavy metals and chloride ions. In addition, studies on the eluviation and leaching behavior of broken, fly-ash-based porous geopolymers have shown that grain size, pH, and solid-liquid ratio significantly affect the leaching of heavy metals, in that order. Thus, heavy metal leaching from fly-ash-based geopolymers can be controlled (Fan et al., 2021; Shi et al., 2021). BFA better than Ordinary Portland cement (OPC) material. Because, the C-A-S-H gel and N-A-S-H gels offer longer chain lengths and denser cross-linking structure than the C-S-H gel of OPC. Moreover, the C-A-S-H gel is more sensitive to chemical attack than the N-A-S-H gel because of the higher Ca/Si ratio (Valencia-Saavedra et al., 2020; Yang et al., 2022). Previous research has studied the use of water treatment residue (WTR) as an immobilizing agent for an electroplating sludge containing Zn, Fe and Cr as the major heavy metals. WTR with an initial SiO_2/Al_2O_3 ratio of 1.78 was pretreated by calcining at 800°C for 1 h. The performance of the WTR-based geopolymer matrix to immobilize 30wt.% electroplating sludge showed strength and metal leaching results which are acceptable for disposal in landfills (Waijarean et al., 2017). Furthermore, these three heavy metals (Zn, Fe and Cr) were synthesized in the form of hydroxides and solutions of nitrates to study the interaction of heavy metals and the microstructure of WTR-based geopolymers (Waijarean et al., 2017). It is suggested that the presence of metal hydroxides as charge-balancing cations in the geopolymer structure affected the strength rather than the incorporation and can immobilize the three heavy metals for disposal in the landfill.

The aim of this research is to investigate the potential of bituminous fly ash (BFA) as the immobilizing agent for an plating sludge. BFA is a waste-derived aluminosiliceous material generated from power plants. The source of bituminous fly ash in Thailand is from bituminous coal-fired power plants in the northeastern region. The toxicity of fly ash is influenced by factors like the type of coal burned and the combustion technology used. However, BFA is not classified as hazardous waste because the toxic levels found are lower than the permissible limit. Therefore, BFA can be used as a material for geopolymer

production. The quantity of fly ash produced is related to the country's energy production from coal. With increasing energy demands, fly ash generation is on the rise. In 2023, approximately 6.05 million tons of bituminous coal were imported, according to the Department of Primary Industries and Mines. In the present research, factors affecting the effectiveness of the BFAG to contain heavy metals present in the plating sludge were studied. Molar ratios of SiO_2/Al_2O_3 between 2 and 3, an alkali activator using NaOH at molar ratios of Na_2O/SiO_2 between 0.15 and 0.30 and various types of leachant were examined. The leaching test was applied from a waste extraction test (WET) using sodium citrate, sodium acetate and synthesis acid rain as leaching solutions. Strengths, microstructures and the ability of the BFAG solidified PS to contain heavy metals were evaluated.

2. METHODOLOGY

2.1 Materials

Bituminous fly ash (BFA) was obtained from the BLCP Power Station in Rayong Province. Si waste which was used to adjust the SiO_2/Al_2O_3 ratio for the BFAG mixtures was obtained from AGC Automotive (Thailand) Co., Ltd. located in Cholburi Province. The starting materials were analysed by X-ray fluorescence (XRF), and the chemical compositions of the elemental oxides are reported in Table 1. In addition, commercial grade NaOH was used as an alkali activator for geopolymerization reactions.

Plating sludge (PS) was generated from the wastewater treatment plant of an electroplating industry in Bangkok, Thailand. The sludge was then oven-dried at 105°C before particle size reduction to less than 50 mm. The PS was subjected to microwave digestion, and the concentration of heavy metals present in the sludge was measured by atomic absorption spectrophotometry. The main heavy metals present in PS were Zn, Fe, and Cr at the concentrations of 690, 163.5, and 37.5 g/kg dry wt. PS, respectively.

2.2 Sample preparation

The geopolymer was synthesized from BFA and activated with a commercial-grade NaOH solution. The molar ratio of BFA was adjusted to have a SiO_2/Al_2O_3 molar ratio of 2:1 and 3:1 through the addition of Si waste. The proportion of each mixture is shown in Table 2. The NaOH solution was added to the solid mixture to gain the required alkali dosage of Na_2O/SiO_2 between 0.15 and 0.3, then mixed for 10 min to obtain a homogeneous mix. The mixtures were then transferred to cylindrical PVC moulds with a diameter of 35 mm and a height of 70 mm, then vibrated for 2 min to remove entrapped air bubbles. The sample specimens were wrapped with cling film to prevent carbonation and water evaporation during curing under ambient temperature (30±2°C). The optimum alkali dosage of NaOH was determined by means of strength development after curing for 7, 28, and 60 days. The solidified PS was prepared by mixing BFA with 30wt.% PS and the solution of NaOH to gain an optimum alkali dosage. All mix proportions were prepared in a similar manner to that of the control (without PS).

Table 1. Chemical compositions of the starting materials

Materials	Chemical composition (wt.%)						
	SiO_2	Al_2O_3	Na_2O	CaO	MgO	Fe_2O_3	K_2O
BFA	60.10	28.70	0.38	1.45	0.47	4.70	1.25
Si-waste	68.10	4.85	0.16	9.53	3.98	0.96	0.55

Table 2. Mix proportions of geopolymer with and without PS

Samples	SiO_2/Al_2O_3 molar ratio	Synthesis geopolymer (% by wt.)				
		BFA	Si-waste	NaOH	PS	Total
BFA geopolymer	2:1	86	-	14	-	100
	3:1	58	28	14	-	100
BFA geopolymer +30wt.%PS	2:1	60	-	10	30	100
	3:1	40	20	10	30	100

2.3 Compressive strength test

The compressive strength of the cylindrical specimens was determined according to the ASTM D 1633-17 test method. The compaction test was done on the smooth surface samples at the age of 7, 28, and 60 days. Six samples for each mix proportion were analysed and the strength value was averaged with 95% confidence to ensure the reproducibility of the results.

2.4 Microstructure characterization

The crystalline phases of the BFAG with and without PS were examined at the age of 28 days using X-ray diffraction (XRD). A Bruker AXS series D8 Discover with Cu Kα radiation with an average wavelength of 1.54184° was used. The powder sample was scanned from 4° to 80° 2θ at a rate of 0.01 s per step. Scanning electron microscopy (SEM) was carried out using a JEOL series JSM-6400 operated at 15 kV. The fragmented samples from the 28-day strength test were used for SEM analysis and coated with gold. The solid-state MAS NMR spectra was used to characterize ^{27}Al resonance. A Bruker Avance III 500 spectrometer operating at an ^{27}Al frequency of 130.24 MHz at a magnetic field of 11.7 T was used, and the spectra were referenced with respect to $Al(H2O)_6^{+3}$.

2.5 Leaching test

A waste extraction test (WET) was used according to the Ministry of Industry, Thailand, standard for assesses the leaching of heavy metals from PS, which was solidified within the BFAG matrix. Three solutions were used as leachants for these tests to simulate the leaching performance under severe and normal scenarios that the solidified PS might encounter during placing in the landfill. These three leachants were sodium citrate, sodium acetate and synthetic acid rain. Sodium citrate and sodium acetate solutions were prepared by adjusting the pH of critic acid and acetic acid with 4 N NaOH to a pH of 5.0±0.1 and 4.93±0.05 whereas the synthetic acid rain was prepared from 80 %v/v sulfuric acid and 20%v/v nitric acid and diluted to a pH of 5.0 with deionized water. The BFAG samples with and without 30wt.% of PS at the age of 28 days were dried in a hot air oven at 105 °C for 1 h. The dried samples were crushed until the particle sizes were less than 2 mm or able to pass through a sieve (No. 10). The crushed samples were then contacted with an amount of leachant which is equal to 10 times that of the sample weight. The closed plastic vessels containing the mixtures were rotated at 300 rpm for 48 h. The leachates were then filtered through a 0.45 µm membrane filter to remove suspended solids. The filtrates were used for pH measurements and heavy metals concentration determination by ICP-AES. Each leachate was analysed in triplicate, and the mean value was reported.

3. RESULTS AND DISCUSSION

3.1 Effect of alkali dosage

Variation in the Na_2O/SiO_2 molar ratio from 0.15 to 0.3 on strength development of BFA-based resulted in a geopolymer with the highest strength of 4.8 and 11.1 MPa from BFA with the starting SiO_2/Al_2O_3 molar ratio of 2 at the age of 28 and 60 days, respectively (Figure 1). NaOH plays an important role in the mechanical strength of the geopolymer matrix in that it activates the surface dissolution of Si and Al from a solid aluminosilicate source of BFA, resulting in the gelation of aluminosilicate species, and helps charge balancing during the polymerization of the aluminosilicate network (Duxson et al., 2005; Castillo et al., 2021). At lower alkali dosage (Na_2O/SiO_2 molar ratio of 0.15), the dissolution rate of Si and Al was low, thus resulting in a lower degree of geopolymerization reactions which is accountable for the lower strength development.

When the Na_2O/SiO_2 molar ratio increased to 0.25 and 0.30, the highly alkali environment increases the rate of surface dissolution of Si and Al from BFA which is responsible for a supersaturation of silicate and aluminate species in the system. A rapid formation of aluminosilicate gel and precipitation on the surface of solid particles at the beginning obstructs further dissolution of Si and Al from the surface of the BFA. Another explanation for this phenomenon could be caused by an increased viscosity of the alkali solution at increasing Na_2O/SiO_2 molar ratio, thus delaying the transportation of silicate and aluminate species after dissolution from BFA. The accumulation of silicate and aluminate species nearby the BFA surface hinders the release of these two species into the solution due to the rise of speciation equilibrium. The excess alkaline therefore negatively affected the strength development of the BFAG. Similar observations have been reported: a very high alkali dosage will dissolve too many fly ash particles, leading to structural disruption of the aluminosilicate phases and a reduction on strength (Zheng et al., 2010; Cheng et al., 2015). Several research have reported the optimal concentrations of sodium hydroxide ranging between 7 and 12 M, with the Na_2O/SiO_2 molar ratio from 0.2

to 4.0 (Amran et al., 2021; Elmesalami and Celik, 2022). The maximum compressive strength of BFAG was found at a Na_2O/SiO_2 ratio of 0.20 that was selected to study effect of SiO_2/Al_2O_3 molar ratio.

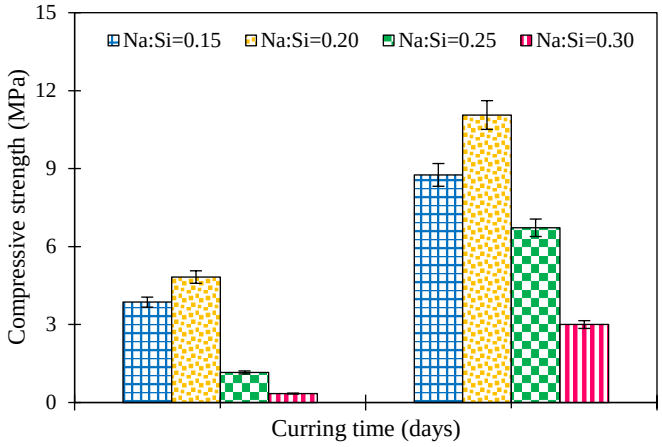

Figure 1. Strength development of BFAG under various alkali dosage

3.2 Effect of SiO_2/Al_2O_3 molar ratio of BFA

Previous research reported that a SiO_2/Al_2O_3 molar ratio of 1:1 resulted in a small amount of N-A-S-H gel, and these mechanisms did not contribute to the development of compressive strength. Conversely, at a SiO_2/Al_2O_3 molar ratio of 4:1, N-A-S-H gel was not observed, and it formed a large pore structure, leading to lower strength and it formed a large pore structure, leading to lower strength. A SiO_2/Al_2O_3 molar ratio of 2:1 and 3:1 was found to promote the formation of a well-dispersed N-A-S-H gel within the geopolymer binder (Aly et al., 2008; Castillo et al., 2022). As these ratios influence compressive strength development, they were chosen for further study in this topic. Higher strength development was obtained from BFA-based geopolymers with a SiO_2/Al_2O_3 molar ratio of 3:1 and a Na_2O/SiO_2 ratio of 0.20 at all curing durations (Figure 2). It is generally known that the structure of geopolymers formed varies from polysialate (-Si-O-Al-O-), to poly sialate-siloxo (-Si-O-Al-O-Si-O-), and poly sialate-disiloxo (-Si-O-Al-O-Si-O-Si-O-) when the SiO_2/Al_2O_3 molar ratios increase from 1:1, 2:1, and 3:1, respectively (Amran et al., 2021; Luhar and Luhar, 2022). In this research, Si-waste was used to adjust the SiO_2/Al_2O_3 molar ratio from an initial value of approximately 2:1 (2.09) to 3:1. It could be possible that the presence of CaO and Al_2O_3 in Si-waste at 9.53 and 4.85wt.% is beneficial for strength development from the formation of CSH gel (calcium silicate hydrate) and additional geopolymer products. CSH gel is formed by the reaction between CaO from Si-waste and silicate species from both Si-waste and BFA which can transform into a solid and harden (Castillo et al., 2021; Su et al., 2023). However, there are several factors affecting strength gain of geopolymers including the availability of the solid aluminosilicate source from the starting materials.

3.3 Effect of plating sludge on strength

A significant reduction in mechanical strength of BFAG containing 30wt.% of PS at the SiO_2/Al_2O_3 molar ratio of 2:1 and 3:1 activating with alkali at a Na_2O/SiO_2 ratio of 0.20 was gained from samples at all curing durations (Figure 3). The strengths of geopolymers at 7 days were 0.38 and 0.55 MPa at the SiO_2/Al_2O_3 molar ratio of 2:1 and 3:1, respectively, while at 28 days, the strengths of geopolymers at the SiO_2/Al_2O_3 molar ratio of 2:1 and 3:1 increased to 1.87 and 2.57 MPa, respectively. The strengths of geopolymers with a SiO_2/Al_2O_3 molar ratio of 2:1 and 3:1 reduced by 56% and 73% compared with control geopolymer. This observation agrees with several publications which were reported to be caused by the interferences of heavy metals on the geopolymerization reactions (Zhang et al., 2008). These heavy metals could be immobilized through physical encapsulation or chemical mechanisms depending on their chemical forms. It was found that the presence of heavy metals as hydroxides affected the strength of geopolymers synthesized by the alkali activation of water treatment residue greater than their presence in the form of soluble nitrates (Waijarean et al., 2017).

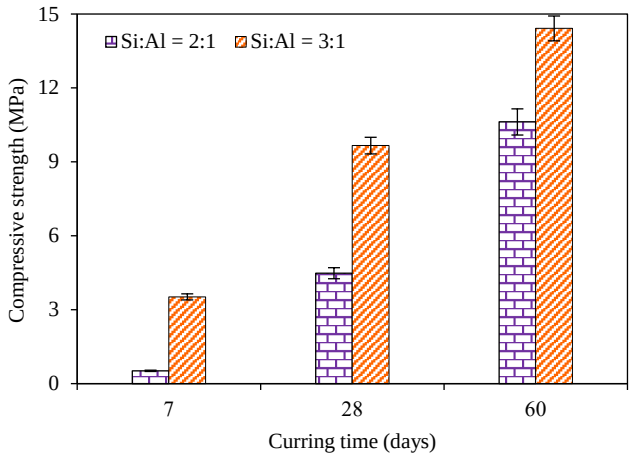

Figure 2. Strength development of BFAG at SiO_2/Al_2O_3 molar ratio of 2:1 and 3:1

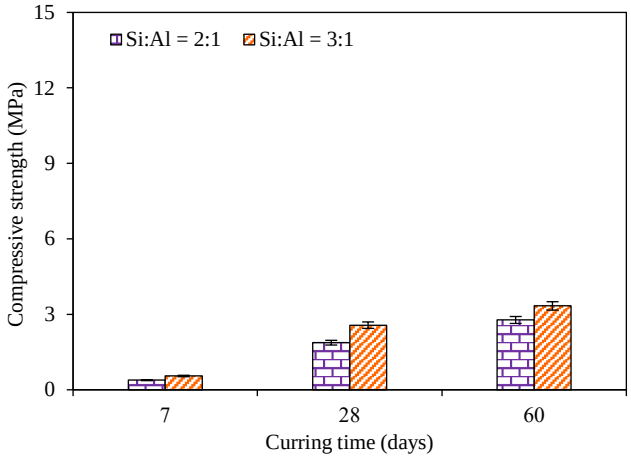

Figure 3. Strength development of BFAG containing 30wt.% PS

Reduction of compressive strength of geopolymer solidified PS results from physical encapsulation and chemical mechanisms. Physical encapsulation adsorbing heavy metal ions on pore structure with Van der Waals force (Zhang et al., 2008; Tian et al., 2022). The chemical mechanisms such as sorption, precipitation, and substitution can be found in geopolymer matrix. Previous research reported that the interfering effects caused by both synthesized metal hydroxides such as $Zn(OH)_2$, $Cr(OH)_3$, and $Fe(OH)_3$, and electroplating sludges. The metal hydroxide ion was adsorbed with chemical bond and high alkalinity can precipitated ion on surface of BFAG that impede geopolymerization reactions. In addition, adsorbed and precipitated metal hydroxide ion reacted and incorporate with alumino-silicious materials and form to metal silicate or metal oxide which reduce SiO in the metrix (Asavapisit and Macphee, 2007; Waijarean et al., 2017). In addition, the negative charge of Al tetrahedrons can bind to metal oxide ions, which replace Na^+ or K^+ in the geopolymer structure (Castillo et al., 2021; Tian et al., 2022). The samples were higher than the minimum requirement of the standard criteria regulated by U.S.EPA 1992 and the ministry of industry (Thailand) standard (0.34 MPa).

3.4 Microstructures of BFAG

In this research, ^{27}Al MAS NMR spectroscopy was used to investigate the structure of the Al-O units. The ^{27}Al MAS NMR spectra of BFA and BFAG with SiO_2/Al_2O_3 molar ratios of 2:1 and 3:1 are shown in Figure 4. The ^{27}Al spectrum of BFA contained broad resonances at 59.4, 54.3, and 1.5 ppm (Figure 4(a)), corresponding to four- and six-fold coordinated Al-O units, respectively. The investigation of the reacted samples of the BFAG at SiO_2/Al_2O_3 molar ratios of 2:1 and 3:1 exhibit the appearance of different aluminium spectra comprising four-, five-, and six-fold coordinated Al. The single sharp tetrahedral Al resonance at 61.0 ppm (Figure 4(b)), and 60.2 ppm (Figure 4(c)) indicates a higher degree of structural

order. The reaction products produced from alkali activation of BFA, which corresponds to the strength gain of the BFAG could be associated with a well-formed geopolymer. When alkali solution was mixed with BFA and forms geopolymer, the material exhibits typical characteristics of a well-reacted geopolymer, evidenced by a sharp tetrahedral ^{27}Al resonance at 61.0 ppm (Figure 4(b)), and 60.2 ppm (Figure 4(c)) indicates a higher degree of structural order. Previous studies showed that the ^{27}Al spectra indicate a mixture of four- and six-fold coordinated Al, the peaks in the spectra of the samples shift of 58.5 and 2.2 ppm (Van Jaarsveld and Van Deventer, 1999). While the ^{27}Al spectrum of the water treatment residue-based geopolymers is typical of dehydroxylated kaolinite-type minerals, containing Al resonances at 59.0, 27.7, and 3.2 ppm, corresponding to four-, five- and six-fold coordinated Al-O units, respectively (Waijarean et al., 2017) The reaction products produced BFAG, and the strength gain of the BFAG could be associated with the formation of a well-formed geopolymer.

SEM micrographs of BFAG with a SiO_2/Al_2O_3 molar ratio of 2:1 and curing for 28 days indicated the presence of unreacted or partially reacted spherical BFA with a variation in particle sizes (Figure 5(a)). The gel-like aluminosilicate materials or geopolymer products were deposited everywhere on the surface of the BFA particles alongside small and large pores or voids scattered throughout the sample. By increasing the SiO_2/Al_2O_3 molar ratio to 3:1, the appearance of a dense microstructure of the geopolymer products were obtained with less pores and voids (Figure 5(b)). This evidence is in-line with the mechanical strength performance of the BFAG (Askarian et al., 2019; Cong and Cheng, 2021; Luhar and Luhar, 2022)

When the PS was added to the BFAG at 30wt.% (Figure 6(a)-(b)), a microstructure consisting of gel-like agglomerations in a less homogenous manner was developed compared to the control (without PS). The formation of these complex mixtures of gel-like products could have arisen from the chemical mechanisms of metal hydroxides present in the PS. These metal hydroxides are very soluble under the highly alkali environment of the system and transport into the aqueous phase of the mixture. This affects the speciation equilibrium during the transformation of the silicate and aluminate species into gel-like products and subsequently hindering the polymerization process. As a result, a less homogenous microstructure containing large pores is responsible for a reduction in mechanical strength (Duxson et al., 2005; Su et al., 2023). The matrix has high porosity and contains unreacted fly ash that may be caused from interfering effect of metal hydroxide ion from PS (Asavapisit and Macphee, 2007; Zheng et al., 2010).

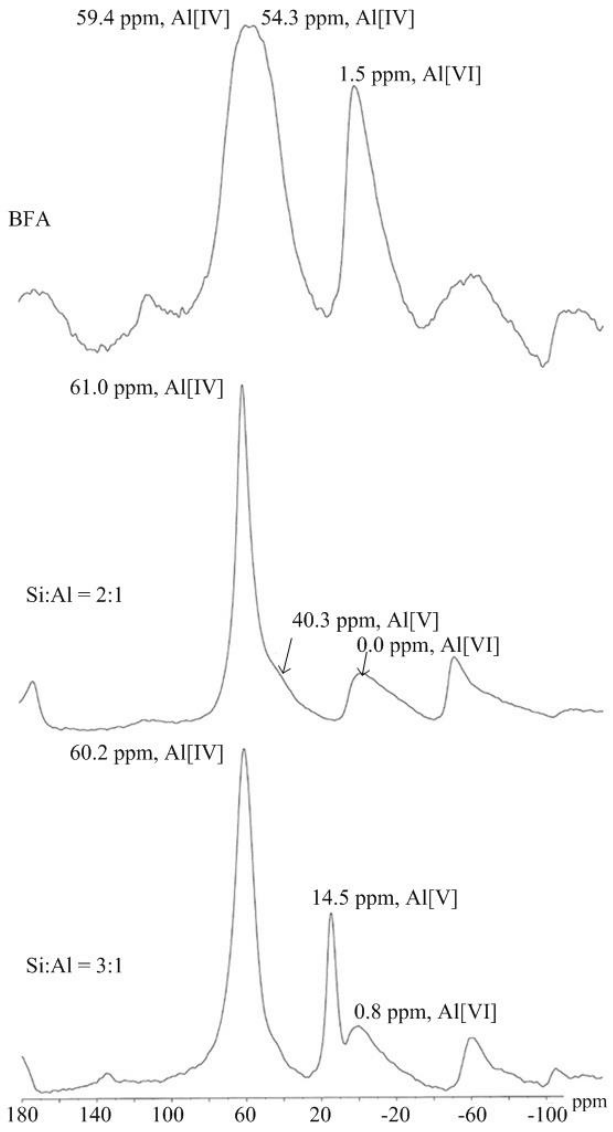

Figure 4. ^{27}Al MAS NMR of BFA, BFAG at SiO_2/Al_2O_3 molar ratio of 2:1 and 3:1

The XRD patterns of BFA and BFAG with SiO_2/Al_2O_3 molar ratios of 2:1 and 3:1 with and without PS are shown in Figure 7 (a)-(c). Quartz and mullite are the two major crystalline phases detected from the BFA sample (Figure 7(a)). The presence of a broad hump in the 2 theta values between 18 and 25 degrees indicates the presence of amorphous materials. In addition to quartz and mullite, the peaks of the sodium aluminium silicate hydrate (NASH) were observed from the BFAG with SiO_2/Al_2O_3 molar ratios of 2:1 and 3:1 (Figure 7(b)). The broad hump in

the 2 theta values from approximately 20 to 40 degrees with low and dispersed intensity diffractograms could be described as semi-crystalline phases including gel-like silicate and aluminate precursors (Van Jaarsveld and Van Deventer, 1999; Silva et al., 2007; Luhar and Luhar, 2022). The addition of the PS at 30wt.% to the alkali activated BFA resulted in the transformation of the original metal hydroxides into different crystalline phases such as zinc silicate ($ZnSiO_4$), maghemite (Fe_2O_3), zinc iron oxide ($ZnFe_2O_4$), aluminium iron oxide ($FeAlO_3$), and chromium oxide (CrO) as shown in Figure 7(c). Previous research reported that the immobilization of heavy metal in fly ash binders activated alkali solutions may be included in the gepolymer matrix in metal silicate hydrate (MSH) form that does not contribute to strength development. (Zheng et al., 2010; Waijarean et al., 2017). Under a highly alkali environment, it could be possible that heavy metals in the original form of hydroxide were solubilized and interacted with other ion species within the system and transformed into other insoluble compounds including zinc silicate. Zinc was present in the PS at the highest concentration among other heavy metals, which was equal to 690 g/kg dry weight. This results in the insufficient silicate anions that can undergo geopolymerization reactions leading to significant a mechanical strength reduction.

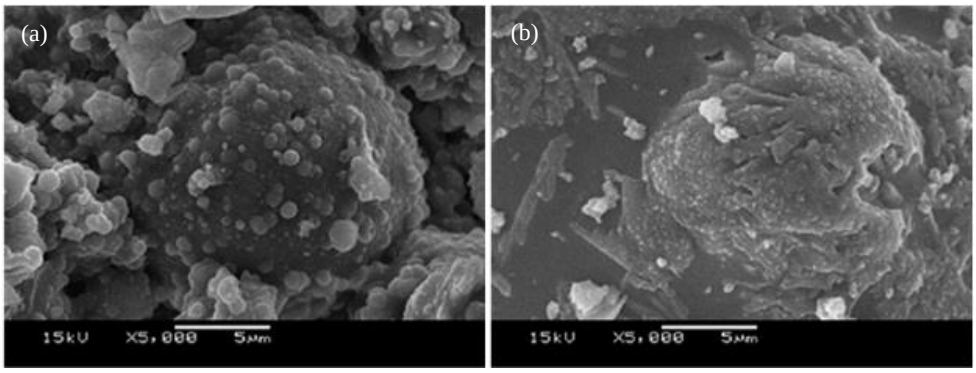

Figure 5. SEM micrographs of BFAG; (a) SiO_2/Al_2O_3 = 2:1, (b) SiO_2/Al_2O_3 = 3:1

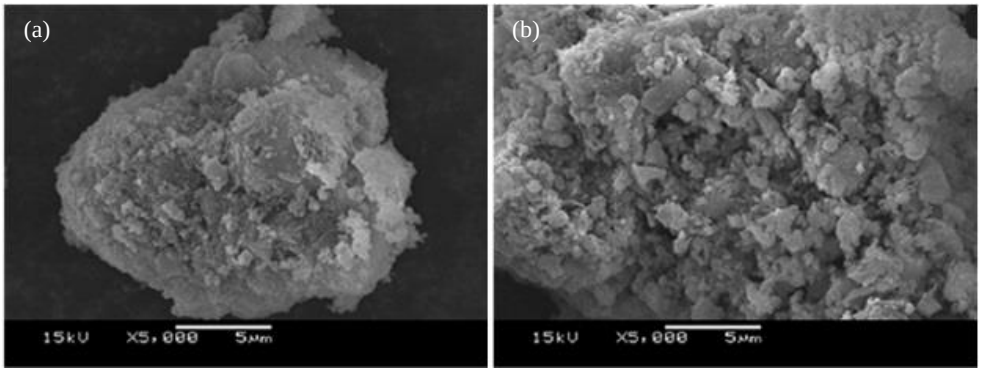

Figure 6. SEM micrograph of BFAG containing 30wt.% PS; (a) SiO_2/Al_2O_3 = 2:1, (b) SiO_2/Al_2O_3 = 3:1

3.5 Effect of various leachants on the heavy metal containment

A waste extraction test was applied to evaluate the leaching performance of heavy metals from BFAG containing 30wt.% PS using different leachants (Table 3). After the solidified PS samples with a SiO_2/Al_2O_3 molar ratio of 2:1 was extracted with the leachants for 48 h, the leachate pH values made with sodium citrate, sodium acetate and synthetic acid rain increased from the initial pH values of 5±0.1 to 7.13, 7.59, and 11.39, respectively. Sodium citrate and sodium acetate are acidic buffer solutions and therefore can resist changes in pH upon contact with a highly alkali solidified sample better than synthetic acid rain. Similar variation in leachate pH values were observed from solidified samples with a SiO_2/Al_2O_3 molar ratio of 3:1.

PS contains Zn, Fe, and Cr at concentrations of 690, 163.5, and 37.5 g/kg dry weight, respectively. The concentration of Zn in the leachates from all samples upon contact with various leachants were the

highest followed by Fe and Cr (Table 3). The leaching process occurs when leachant into the solidified samples through micro-cracking, connected pores and voids. This interrupts the chemical equilibrium within the solidified matrix, resulting in the solubilization of heavy metals immobilized within the geopolymer network. The soluble heavy metals were then transported out of the solidified sample into the leachant via diffusion, a process controlled by the concentration gradient between the solid and solution (Asavapisit and Macphee, 2007; Amran et al., 2021; Tian et al., 2022).

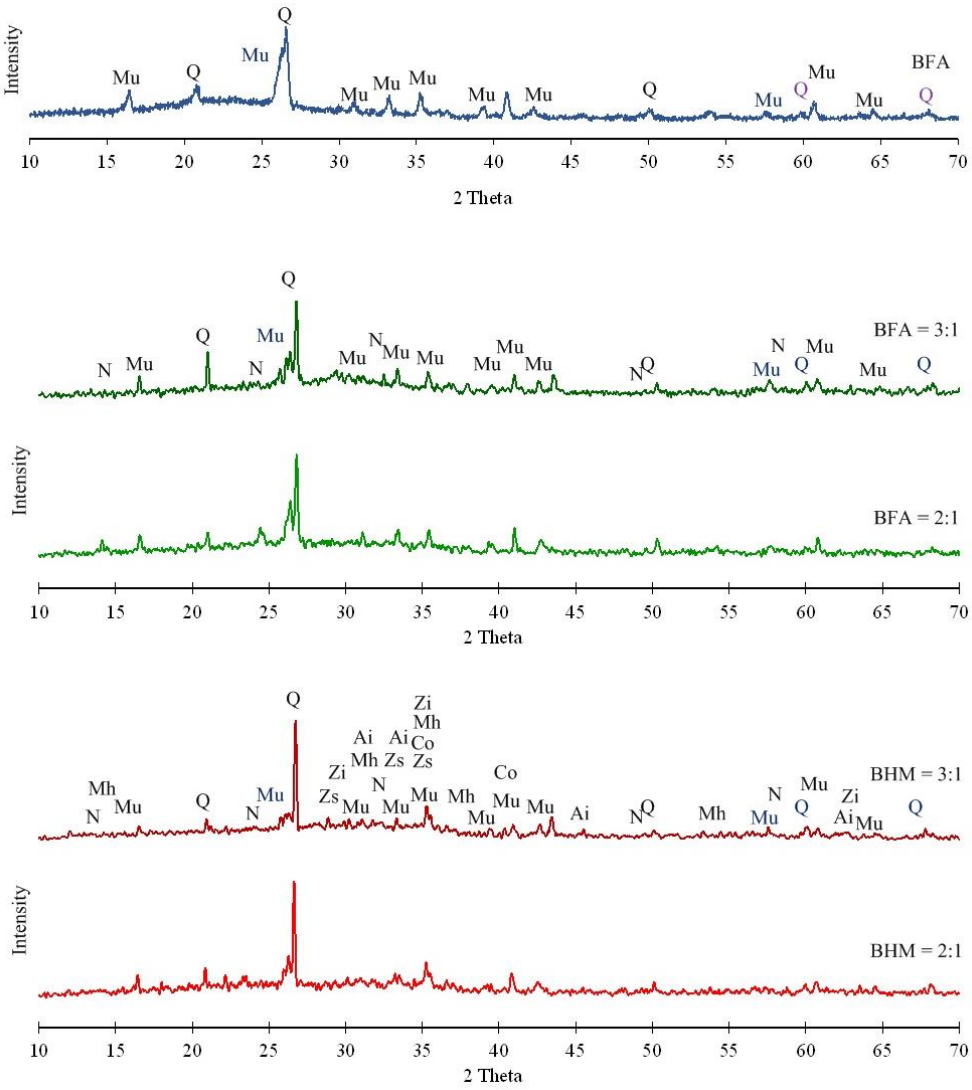

Figure 7. XRD patterns of (a) BFA, (b) BFAG at SiO_2/Al_2O_3 = 2:1 and 3:1 and (c) BFAG containing 30wt.% PS, (Q=Quartz, Mu=Mullite, N=NASH-Sodium aluminum silicate hydrate, Ma=Maghemite, Zs=Zinc Silicate, Co= Chromium Oxide, Zi=Zinc Iron Oxide, Ai=Aluminium Iron Oxide)

The highest concentration of Zn, Fe, and Cr were found in sodium citrate solution. This is because sodium citrate is more aggressive than sodium acetate and synthetic acid rain. Both sodium citrate and sodium acetate are leachants made with organic acids (citric and acetic) which can act as chelators by bonding to Zn, Fe, and Cr resulting in the formation of complexes with these metal ions. Citric and acetic acids are weak carboxylic acids and can partially dissociate in water to generate hydronium (H_3O^+) and carboxylate ($RCOO^-$) ions. Sodium citrate which is a tricarboxylic acid can generate hydronium ions greater than sodium acetate, which is a monocarboxylic acid and as a result, could lead to a higher solubility of heavy metals (Asavapisit and Macphee, 2007; Zhang et al., 2008; Tian et al., 2022). In addition, pKa of sodium citrate (pKa=3.13) is lower than pKa of sodium acetate (pKa=4.76), which can donate a proton very easily and destroy the geopolymer matrix easily.

On the other hand, synthetic acid rain consists of nitric and sulfuric acids, which are strong mineral acids. But during the preparation of synthetic acid rain, the nitric and sulfuric acids may be dissociated in the second and third rounds in water, resulting in a lower pKa value compared to the citrate and acetate acids. It is rapidly neutralized by hydroxide ions (OH^-) from the highly alkali solidified sample which caused the leachate pH values of all samples to increase from an initial value of 5 to 11.3. The hydrolysis of the amphoteric metal oxides or hydroxides in the leachate comprising excess OH^-, lead to the formation of complex ions with heavy metals which are soluble (Asavapisit and Macphee, 2007; Zhang et al., 2008; Tian et al., 2022). Although Zn was found to have the highest concentration in all leachates, the ability of the BFAG matrix to contain all heavy metals of interest was higher than 98%.

Table 3. Concentration of heavy metals in leachate extracted using waste extraction test and contacted with various types of leachant.

Types of leachant	Initial pH	Leachate pH	Concentration of heavy metals (mg/L)			%Containment		
			Cr*	Fe	Zn*	Cr	Fe	Zn
The ministry of industry (Thailand) Standard*			5	-	250			
SiO_2/Al_2O_3 = 2:1								
sodium citrate	4.93	7.13	4.97	12.44	408.40	99.52	99.72	97.84
sodium acetate	5.00	7.59	2.06	3.84	218.60	99.80	99.91	98.84
synthetic acid rain	5.00	11.39	1.54	4.95	224.10	99.86	99.90	98.92
SiO_2/Al_2O_3 = 3:1								
sodium citrate	4.93	7.65	1.73	6.67	284.20	99.83	99.85	98.50
sodium acetate	5.00	7.11	0.50	3.07	152.10	99.95	99.93	99.19
synthetic acid rain	5.00	11.30	0.32	4.53	154.20	99.97	99.91	99.26

4. CONCLUSIONS

BFA, a waste-derived aluminosiliceous material from power plants is suitable to be used for the synthesis of geopolymers by alkali activation. Geopolymers produced with a Na_2O/SiO_2 molar ratio of 0.2 and a SiO_2/Al_2O_3 molar ratio of 3:1 were capable of immobilizing heavy metal-containing PS. SEM and XRD results indicate that the addition of 30wt.% PS significantly affected the mechanical strength and structure of the BFAG. This arises because the heavy metals present in the PS as hydroxides were transformed into different insoluble crystalline phases and physically encapsulated within the matrix instead of being incorporated as charge-balancing cations in the geopolymer network. A leaching test suggested that the BFAG with a SiO_2/Al_2O_3 molar ratio of 3:1 achieved the best immobilization of the PS. The leaching behaviour of heavy metals is dependent on both the chemical forms of heavy metals and the types of leachant. BFAG can substitute ordinary Portland cement (OPC) as solidified binder for treat metals hydroxide from PS before landfilling. This substitution offers two benefits: reducing cement usage and CO_2 emissions from cement production. Furthermore, it aligns with the bio-circular-green process by utilizing industrial waste for beneficial purposes. It provides the additional advantage of reducing waste through the repurposing of fly ash, serving as a guideline for studying waste utilization to sustainability in the industry.

ACKNOWLEDGEMENTS

This research is partially funded by the national research council of Thailand. The Environmental technology Laboratory, School of Energy, Environmental and Materials, KMUTT, deserved appreciation for providing access to their laboratories.

REFERENCES

Aly Z, Vance ER, Perera DS, Hanna JV, Griffith CS, Davis J, et al. Aqueous leachability of metakaolin-based geopolymers with molar ratios of Si/Al=1.5-4. Journal of Nuclear Materials 2008;378(2):172-9.

Amran M, Debbarma S, Ozbakkaloglu T. Fly ash-based eco-friendly geopolymer concrete: A critical review of the long-term durability properties. Construction and Building Materials 2021;270:Article No. 121857.

Asavapisit S, Macphee DE. Immobilization of metal-containing waste in alkali-activated lime-RHA cementitious matrices. Cement and Concrete Research 2007;37(5):776-80.

Askarian M, Tao Z, Samali B, Adam G, Shuaibu R. Mix composition and characterisation of one-part geopolymers

with different activators. Construction and Building Materials 2019;225:526-37.

Castillo H, Collado H, Droguett T, Sánchez S, Vesely M, Garrido P, et al. Factors affecting the compressive strength of geopolymers: A review. Minerals 2021;11(12):Article No. 1317.

Castillo H, Collado H, Droguett T, Vesely M, Garrido P, Palma S. State of the art of geopolymers: A review. e-Polymers 2022;22(1):108-24.

Cheng H, Lin KL, Cui R, Hwang CL, Chang YM, Cheng TW. The effects of SiO_2/Na_2O molar ratio on the characteristics of alkali-activated waste catalyst-metakaolin based geopolymers. Construction and Building Materials 2015;95:710-20.

Cong P, Cheng Y. Advances in geopolymer materials: A comprehensive review. Journal of Traffic and Transportation Engineering (English Edition) 2021;8(3):283-314.

Duxson P, Provis JL, Lukey GC, Mallicoat SW, Kriven WM, Deventer JSJ. Understanding the relationship between geopolymer composition, microstructure and mechanical properties. Colloids and Surfaces A: Physicochemical and Engineering Aspects 2005;269(1-3):47-58.

Elmesalami N, Celik K. A critical review of engineered geopolymer composite: A low-carbon ultra-high-performance concrete. Construction and Building Materials 2022; 346:Article No. 128491.

Fan C, Wang B, Ai H, Qi Y, Liu Z. A comparative study on solidification/stabilization characteristics of coal fly ash-based geopolymer and Portland cement on heavy metals in MSWI fly ash. Cleaner Production 2021;319:Article No. 128790.

Lombi E, Stevens DP, McLaughlin MJ. Effect of water treatment residuals on soil phosphorus, copper and aluminium availability and toxicity. Environmental Pollution 2010; 158(6):2110-16.

Luhar I, Luhar S. A comprehensive review on fly ash-based geopolymer. Journal of Composites Science 2022;6(8):Article No. 219.

Provis JL, Deventer JSJ. Geopolymers: Structure, Processing, Properties and Industrial Applications. Cambridge, United Kingdom: Woodhead Publishing; 2009.

Shi P, Zhang Y, Sun Q, Ta X. Eluviation and leaching of elements from broken fly-ash-based porous geopolymer. Materials 2021;14(22):Article No. 6884.

Silva P, Crenstil KS, Sirivivatnanon V. Kinetics of geopolymerization: Role of Al_2O_3 and SiO_2. Cement and Concrete Research 2007;37(4):512-8.

Su Y, Luo B, Luo Z, Xu F, Huang H, Long Z, et al. Mechanical characteristics and solidification mechanism of slag/fly ash-based geopolymer and cement solidified organic clay: A comparative study. Journal of Building Engineering 2023;71:Article No. 106459.

Sun Z, Tang Q, Xakalashe BS, Fan X, Gan M, Chen X, et al. Mechanical and environmental characteristics of red mud geopolymers. Construction and Building Materials 2022;321:Article No. 125564.

Teixeira SR, Santos GTA, Souza AE, Alessio P, Souza SA, Souza NR. The effect of incorporation of a Brazilian water treatment plant sludge on the properties of ceramic materials. Applied Clay Science 2011;53(4):561-5.

Tian Q, Bai Y, Pan Y, Chen C, Yao S, Sasaki K, et al. Application of geopolymer in stabilization/solidification of hazardous pollutants: A Review. Molecules 2022;27(14):Article No. 4570.

Valencia-Saavedra WG, Mejía de Gutiérrez R, Puertas F. Performance of FA-based geopolymer concretes exposed to acetic and sulfuric acids. Construction and Building Materials 2020;275:Article No. 119503.

Van Jaarsveld JGS, Van Deventer FSJ. The effect of metal contaminants on the formation and properties of waste-based geopolymers. Cement and Concrete Research 1999;29(8): 1189-200.

Waijarean N, MacKenzie KJD, Asavapisit S, Piyapanuwat R, Jameson GNL. Synthesis and properties of geopolymers based on water treatment residue and their immobilization of some heavy metals. Journal of Materials Science 2017;52:7345-59.

Xia M, Muhammad F, Li S, Lin H, Huang X, Jiao B, et al. Solidification of electroplating sludge with alkali-activated fly ash to prepare a non-burnt brick and its risk assessment. The Royal Society of Chemistry 2020;10:4640-9.

Yang M, Zheng Y, Li X, Yang X, Rao F, Zhong L. Durability of alkali-activated materials with different C-S-H and N-A-S-H gels in acid and alkaline environment. Materials Research and Technology 2022;16:619-30.

Zhang J, Provis JL, Feng D, Van Deventer JSJ. Geopolymers for immobilization of Cr^{+6}, Cd^{+2}, and Pb^{+2}. Journal of Hazardous Materials 2008;157(2-3):587-98.

Zheng L, Wang W, Shi Y. The effects of alkaline dosage and Si/Al ration on the immobilization of heavy metals in municipal solid waste incineration fly ash- based geopolymer. Chemosphere 2010;79(6):665-71.

Environment and Natural Resources Journal

Volume 23
Issue 2
2025

Fiber Morphology of *Syzygium tripinnatum* (Blanco) Merr. Stemwood and Branchwood and Their Derived Values

Jayric F. Villareal[1*], Cindy E. Poclis[1], Mark Gerry B. Barron[2], Reymark P. Rivera[2], and Oliver S. Marasigan[3]

[1]*College of Forestry and Environmental Studies, Mindanao State University-Maguindanao, Dalican, Datu Odin Sinsuat, Maguindanao del Norte, Bangsamoro Autonomous Region in Muslim Mindanao (BARMM), Philippines*
[2]*College of Agroforestry and Forestry, Don Mariano Marcos Memorial State University, North La Union Campus, Bacnotan, La Union, Philippines*
[3]*Forest Products Research and Development Institute (FPRDI), Department of Science and Technology (DOST), College, Laguna, Philippines*

ARTICLE INFO

Received: 1 Oct 2024
Received in revised: 10 Jan 2025
Accepted: 14 Jan 2025
Published online: 21 Feb 2025
DOI: 10.32526/ennrj/23/20240245

Keywords:
Pulp and paper suitability/ Rigidity coefficient/ Runkel ratio/ *Syzygium tripinnatum* (Blanco) Merr./ Wood-derived values

*** Corresponding author:**
E-mail:
jfvillareal@msumaguindanao.edu.ph

ABSTRACT

Syzygium tripinnatum (Blanco) Merr. is an indigenous fruit tree species in the Philippines. This study characterizes the fiber morphology (fiber length, diameter, lumen diameter, and cell wall thickness) and derived values (Runkel ratio, slenderness ratio, flexibility ratio, Mulhsteph ratio, and rigidity coefficient) of *S. tripinnatum* wood grown in the Philippines. The results revealed that branchwood fibers were 1.610% longer, and both fiber and lumen diameters were 2.170% and 9.600% thicker, respectively, compared to stemwood. However, the cell wall thickness of stemwood was 1.670% greater than that of branchwood. In terms of derived values, stemwood exhibited higher values by 10.410% for the Runkel ratio, 0.580% for the slenderness ratio, 1.990% for the Mulhsteph ratio, and 3.030% for the rigidity ratio, while branchwood displayed a 7.350% higher flexibility ratio. Statistical analysis indicated no significant difference in fiber morphology or derived values between the two wood types. Based on the fiber morphology, *S. tripinnatum* wood is highly rigid and stiff, making it difficult to collapse, and thus less efficient for pulp and paper production, and bulkier for paper. However, the study suggests that *S. tripinnatum* could be suitable for construction, furniture, tool handles, cabinetry and pilings due to its cell wall thickness, Runkel ratio, flexibility ratio, Mulhsteph ratio, and rigidity coefficient. Further research into other properties of *S. tripinnatum* wood, considering factors such as tree maturity, height, sample size, and habitat would be crucial for accurately determining its suitability for the intended applications.

1. INTRODUCTION

The Philippines recorded more than 300 species of edible fruit-bearing trees, wherein more than half are endemic and native, but very few are cultivated commercially (Dulay et al., 2023). With a favorable climate and soil fertility, the Philippines become an ideal location for tropical fruit production. Also, promoting the local native fruits of the country that show huge market potential may help increase the incomes of the community, especially farmers and their families who are into fruit production and processing.

One of the economically useful indigenous fruit tree species in the country is *Syzygium tripinnatum* (Blanco) Merr. under the Myrtaceae family, commonly known as Hagis (Coronel, 2002). It is also native to some parts of Southeast Asia which primarily grow in the wet tropical biome and are characterized as a small to medium-sized evergreen tree growing up to 20 m high (Malabrigo and Umali, 2022). The fruits

Citation: Villareal JF, Poclis CE, Barron MGB, Rivera RP, Marasigan OS. Fiber morphology of *Syzygium tripinnatum* (Blanco) Merr. stemwood and branchwood and their derived values. Environ. Nat. Resour. J. 2025;23(2):176-184. (https://doi.org/10.32526/ennrj/23/20240245)

of *S. tripinnatum* can be processed into jam, jelly, wine, or juice, and can also be eaten raw and mixed with salt or sugar to neutralize its sour taste. The fruit was characterized as color white when young yet turned into cherry-like red when becomes ripened with a juicy and sour taste and could be processed into wine. *S. tripinnatum* was considered a lesser-known native fruit tree species and often overlooked not because of its unpleasant taste and not nutritious compared to other fruits, but due to its unfamiliarity.

Moreover, fruit-bearing trees are often overlooked as wood sources, with the timber industry traditionally focusing on fast-growing exotic species (Alipon et al., 2016). According to Marasigan et al. (2023) and Marasigan et al. (2024), 18 senile fruit-bearing trees cultivated in the Philippines, including *Syzygium cumini* (related to *S. tripinnatum*), can be used for various wood applications such as construction, plywood, flooring, furniture, and pulp and paper. *S. cumini*, classified under medium strength, is particularly suitable for these uses (Marasigan et al., 2024). Additionally, fruit-bearing trees are abundant in many areas in the Philippines, and harvesting senile or unproductive trees not only expands their potential for diverse applications, but also provides a sustainable timber alternative while offering farmers additional income (Del Castillo, 2021).

To date, there is limited literature on the botanical and morphological characteristics of *S. tripinnatum* trees, and no specific studies have addressed the wood properties and potential uses of this species not just in the Philippines but also worldwide. Thus, *S. tripinnatum* was classified as not evaluated (NE) plant under IUCN 2021-3 (Malabrigo and Umali, 2022). Mainstreaming of the native tree species nowadays would be of great help to spread awareness of their significant role in the ecological balance and sustainable ecosystem.

Understanding the wood properties of *S. tripinnatum* is crucial in promoting its potential uses. To evaluate the quality of its wood, it is vital to characterize the basic wood properties of this species to uncover the full potential and determine the suitability for proper utilization and sustainable production, while driving innovations in eco-friendly material science and advancing technical expertise in wood-based industry.

This study also provides significant data on the characteristics of *S. tripinnatum* wood that would serve as a basis for further studies on this species and related topics. Particularly, this study aims to characterize the fiber morphology and derived values of *S. tripinnatum* stemwood and branchwood, which ultimately affects final wood product properties and energy efficient production for sustainable forest management and eco-friendly product development.

2. METHODOLOGY

2.1 Plant materials and wood samples collection

S. tripinnatum wood samples were collected at Don Mariano Marcos Memorial State University - North La Union Campus, Bacnotan, La Union (16°43′32″N 120°23′16″E), Philippines with an elevation ranging from 45-50 meter above sea level (m.a.s.l.) (Figure 1), typically experiences a Type I climate under the Philippine climate classification system.

Wood samples with three (3) replications were taken from the two wood types (i.e., stemwood and branchwood) of the selected three (3) mature *S. tripinnatum* trees, with an estimated age of 20 years old with different diameters at breast height (DBH) (D_1-18 cm, D_2-23 cm, and D_3-29 cm). Using the increment borer, the wood samples were gathered. Stemwood samples were collected from the trees' DBH, while branch samples were collected at the first branch of the tree with a 10 cm diameter and above. After the wood sample extraction, the holes caused by increment borer in the trees were patched with wood and painted to prevent wood-boring/degrading macro/microorganisms like fungi and insects.

2.2 Fiber morphology of *S. tripinnatum* wood

2.2.1 Fiber maceration

Matchstick-sized samples were prepared from the collected wood samples and then macerated in equal volumes (1:1) of acetic acid and hydrogen peroxide (50% concentration) following the procedure of Villareal et al. (2022a). The maceration was done in a water bath and heated for 6-h until the samples turned white and soft to separate individual fibers. The samples were then washed with distilled water until acid-free and subjected to microscopic observation and measurement.

2.2.2 Fiber measurement

Before fiber measurement, the macerated samples inside the test tubes were shaken to ensure the separation of different structural elements. Thirty undamaged fibers were observed per replicate under the Phenix 300 series microscope and measured using

ImageJ Software. The fibers' length, diameter, and lumen diameter of each fiber were measured following the International Association of Wood Anatomists (IAWA) standard (Wheeler et al., 1989), while the cell wall thickness was determined based on the difference between the fiber diameter and lumen diameter.

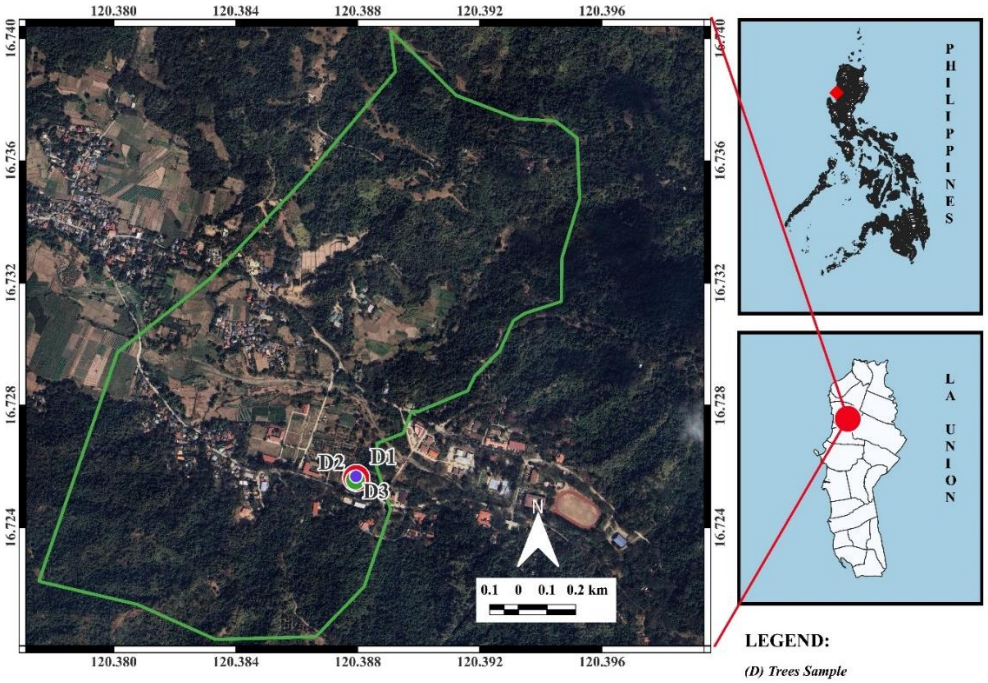

Figure 1. Location map of the collected *S. tripinnatum* wood samples

2.2.3 Derived values

Based on the fiber morphology data, the derived values such as Runkel ratio (1), slenderness ratio (2), flexibility ratio (3), Mulhsteph ratio (4), and rigidity coefficient (5) were computed using the equations used by Hartono et al. (2022). The assessment of the potential of *S. tripinnatum* as raw materials for pulp and paper production was conducted using the Indonesian Timber Assessment Criteria as Raw Materials for Pulp and Paper (Hartono et al., 2022).

$$\text{Runkel ratio} = \frac{2 \times \text{Cell wall thickness}}{\text{Lumen diameter}} \quad (1)$$

$$\text{Slenderness ratio} = \frac{\text{Fiber length}}{\text{Fiber diameter}} \quad (2)$$

$$\text{Flexibility ratio} = \frac{\text{Lumen diameter}}{\text{Fiber diameter}} \times 100 \quad (3)$$

$$\text{Mulhsteph ratio (\%)} = \frac{\text{Fiber diameter}^2 - \text{Lumen diameter}^2}{\text{Fiber diameter}^2} \times 100 \quad (4)$$

$$\text{Rigidity coefficient} = \frac{\text{Cell wall thickness}}{\text{Fiber diameter}} \quad (5)$$

2.3 Statistical analysis

T-test analysis was used to compare the stemwood and branchwood fiber morphology and derived values of *S. tripinnatum*. The statistical analysis was carried out using Jamovi version 2.3 (Jamovi Project, 2022).

3. RESULTS AND DISCUSSION

3.1 Fiber morphology

The fiber morphology (e.g., fiber length, fiber diameter, lumen diameter, and cell wall thickness) of *Syzygium tripinnatum* Blanco (Merr.) stemwood and branchwood and other *Syzygium* species, were presented in Table 1.

3.1.1 Fiber length (mm)

The result of the study showed that the longest fiber was recorded in D_2 (23 cm diameter) with 1.473 mm, followed by D_3 (29 cm diameter) with 1.434 mm, while the shortest was recorded in D_1 (18 cm diameter) with 1.428 mm. On the other hand, the mean fiber length of branchwood (1.450 mm) was 1.610% longer than stemwood (1.427 mm). However, the observed difference in fiber length was not significant (p-value of 0.697). Moreover, the mean fiber length of *S. tripinnatum* was relatively longer than *Eucalyptus tereticornis* Sm. (0.720 mm), *Eucalyptus grandis* W.Hill ex Maiden (0.920 mm) (Sharma et al., 2011), and *Aquilaria cumingiana* (Decne.) Ridl. (0.980 mm) (Villareal et al., 2022a). However, the result was

relatively comparable with 3-, 5-, and 7-year-old *Falcata* trees (1.160, 1.140, and 1.170 (mm), respectively) (Alipon et al., 2021). In comparation to other *Syzygium* species (Table 1), *S. tripinnatum* fiber was longer than *S. fruticosum* (Roxb.) DC., *S. nervosum* DC., and *S. praecox* (Roxb.) Rathakr. & N.C. Nair, while shorter than *S. cumini* (L.) Skeels, *S. jambos* (L.) Alston, *S. album* Q.F. Zheng, and *S. brevistylum* (C.B. Rob) Merr. According to Thumm and Dickson (2013), fiber length is positively correlated with wood density, flexural strength, and stiffness. Based on this, the results suggest that compared to *E. tereticornis*, *S. fruticosum*, *S. nervosum*, and *S. praecox*, *S. tripinnatum* may exhibit higher flexural strength and stiffness, enabling it to withstand higher bending loads. However, it could have lower strength than *S. cumini*, *S. jambos*, *S. album*, and *S. brevistylum*.

Table 1. Fiber morphology of *Syzygium tripinnatum* Blanco (Merr.) stemwood and branchwood and other *Syzygium* species

Species	Fiber length (mm)	Fiber diameter (µm)	Lumen diameter (µm)	Cell wall thickness (µm)
S. Tripinnatum Blanco (Merr.)				
(Stemwood)	1.427	26.023	8.853	8.587
(Branchwood)	1.450	26.590	9.703	8.443
S. cumini (L.) Skeels*	1.767	25.130	18.620	3.260
S. fruticosum (Roxb.) DC.*	1.287	23.300	16.660	3.320
S. jambos (L.) Alston*	1.658	22.200	11.620	5.290
S. nervosum DC.*	1.405	24.040	17.910	3.070
S. praecox (Roxb.) Rathakr. & N.C. Nair*	1.362	20.760	14.390	3.180
S. album Q.F. Zheng**	1.578	20.660	4.420	8.095
S. brevistylum (C.B. Rob) Merr.***	1.688	26.000	12.000	7.000

Source: * Wangkhem et al. (2020); ** Sun et al. (2023); *** FPRDI (1996)

Based on the groupings devised by Salehi (2001), the fibers of *S. tripinnatum* fall under the second group which is characterized to have an average fiber length ranging from 0.9 to 1.9 mm and classified as medium-length of fiber under the Forest Product Research and Development Institute (FPRDI) (1996). According to Sharma et al. (2011), paper made from a longer fiber exhibited higher tearing resistance, and long fibers with thin cell walls were much preferable for pulp and paper manufacturing. Further, fibers with an average greater than 0.4 mm are considered suitable raw materials for papermaking (Suansa and Al-Mefarrej, 2020), while fibers of 1 to 5 mm length are commonly used for making composite materials (Madsen et al., 2013). Thus, *S. tripinnatum* fibers might be ideal for pulp and paper with a tolerable tearing strength and could potentially be used as a raw material for composite boards in furniture and structural applications when the trees become senile.

3.1.2 Fiber diameter (µm)

The results showed that D_1 had the largest fiber diameter, measuring 26.850 µm, followed by D_2 at 26.540 µm, and D_3 at 25.530 µm. The larger fiber diameter observed in D_1 could be attributed to a higher proportion of juvenile wood than the other diameter classes. According to Kartikawati et al. (2024), juvenile wood typically has a larger fiber diameter than mature wood. It is also observed that fibers in stemwood (26.020 µm) were 2.170% thinner than the fibers in branchwood (26.590 µm). However, the observed difference of fiber diameter between stemwood and branchwood was not significant with a p-value of 0.161. As compared to the fiber diameter of *E. tereticornis* (14.600 µm), and *E. grandis* (19.200 µm) (Sharma et al., 2011), *S. tripinnatum* fiber was relatively larger. However, it was thinner than the fibers of 3- and 7-year-old *Falcata* trees (35.440 µm and 38.010 µm, respectively) (Alipon et al., 2021). As shown in Table 1, *S. tripinnatum* fiber was relatively larger than other *Syzygium* species. According to Yahaya (2001), wood with a larger fiber diameter tends to exhibit higher strength properties. Thus, the relatively larger fiber diameter of *S. tripinnatum* suggests that this species could potentially possess higher strength than the other *Syzygium* species.

3.1.3 Lumen diameter (µm)

With the largest fiber diameter, D_1 also exhibited the largest lumen diameter, measuring 10.590 µm. This was followed by D_2 (9.640 µm) and D_3 (7.610 µm). The higher lumen diameter observed in D_1 is likely due to

the greater proportion of juvenile wood in this diameter class, an occurrence also reported by Kartikawati et al. (2024) in *Diospyros kaki* wood. However, the proportion of juvenile and mature wood was not explored in the present study. This presents an interesting area for future research on this species to determine which diameter class has the higher proportion of mature wood for optimal wood production.

As to wood type, branchwood (9.703 µm) showed 9.600% larger lumen than stemwood (8.853 µm). However, analysis showed that the difference in result was not significant with a p-value of 0.147. The mean result of the study was relatively larger compared to *E. tereticornis* (5.120 µm), and *E. grandis* (6.670 µm) (Sharma et al., 2011), but thinner than 3- and 7-year-old *Falcata* trees (31.700 µm and 28.900 µm, respectively) (Alipon et al., 2021). Moreover, the majority of the *Syzygium* species (Table 1) exhibited larger lumen diameter than *S. tripinnatum*, except for *S. album*. According to Izani et al. (2008), wood with a larger lumen diameter tends to have lower relative density and strength properties. As shown in Table 1, the lumen diameter of *S. tripinnatum* was smaller compared to other *Syzygium* species, except for *S. album*, supporting the notion that this species could have better relative density and strength properties, reinforcing the earlier claim about its fiber diameter. Kiaei et al. (2014) noted that lumen diameter influences the beating process in pulp and paper production, as larger lumen diameters allow for better liquid penetration in the fibers. Based on this, *S. tripinnatum* fibers might facilitate an effective beating process.

3.1.4 Cell wall thickness (µm)

With the thinnest fiber and lumen diameter, D_3 recorded the thickest cell wall with 8.960 µm, followed by D_2 (8.450 µm) and D_1 (8.130 µm). The thicker cell wall in D_3 could indicate a higher proportion of mature wood in this diameter class. According to Kartikawati et al. (2024), mature wood typically has a thicker cell wall than juvenile wood which was also displayed in this present study.

Stemwood fibers (8.587 µm) recorded 1.670% thicker cell walls than branchwood fibers (8.443 µm). The result further validates the findings on Plumwood by Kiaei et al. (2014), and *G. falcatum* by Villareal et al. (2022b) that cell wall thickness increases as the wood matures, considering the property of the branch usually having juvenile wood and commonly exhibits thinner cell walls than the mature wood from the stem. However, analysis revealed no significant difference in cell wall thickness between wood types with a p-value of 0.681. The mean result of cell wall thickness was relatively thicker than *E. tereticornis* (4.740 µm), *E. grandis* (6.270 µm) (Sharma et al., 2011), 3- and 7-year-old *Falcata* trees (3.270 µm and 3.140 µm) (Alipon et al., 2021), and *A. cumingiana* (4.360 µm) (Villareal et al., 2022a). Compared to other *Syzygium* species (Table 1), *S. tripinnatum* fibers exhibited thicker cell wall. Cell wall thickness increases towards maturity. The present result suggests that *S. tripinnatum* fiber could be more rigid and produce less dense paper since the cell wall governs the fiber flexibility and the bulkiness of paper (Sharma et al., 2011). Furthermore, due to its thicker cell wall compared to *E. tereticornis*, Falcata trees, *A. cumingiana*, and other *Syzygium* species, *S. tripinnatum* could likely have better relative density and higher strength properties (NagarajaGanesh and Rekha, 2020).

3.2 Derived values

The derived values of *S. tripinnatum* stemwood and branchwood, such as the Runkel ratio, slenderness ratio, flexibility ratio, Mulhsteph ratio, and rigidity coefficient were presented in Table 2.

Table 2. Derived values of *Syzygium tripinnatum* Blanco (Merr.) stemwood and branchwood

Derived values	Wood type		Significant level of difference (p-value)
	Stemwood	Branchwood	
Runkel ratio	1.950	1.747	0.265^{ns}
Slenderness ratio	54.833	54.513	0.877^{ns}
Flexibility ratio (%)	34.017	36.520	0.272^{ns}
Mulhsteph ratio (%)	88.387	86.623	0.275^{ns}
Rigidity coefficient	0.330	0.320	0.288^{ns}

ns-not significant at 0.05 significant level

3.2.1 Runkel ratio

The highest Runkel ratio was recorded in the larger diameter (D_3) with a value of 2.840, followed by D_2 and D_1 having 2.070 and 1.890 Runkel ratio values, respectively. This result might be due to a higher proportion of mature wood in D_3 than D_2 and D_1. Also, the result showed an increasing trend wherein as the diameter increases, the Runkel ratio also increases. In terms of wood types, stemwood fibers (1.950) exhibited a 10.410% higher Runkel ratio than branchwood fibers (1.747). This result also conforms to the diameter status of the stem and branch since the stem diameter is normally larger than the branch diameter. On the other hand, no significant difference (p-value of 0.265) was observed signifying a comparable result of wood types. Moreover, the result of the study was relatively higher compared to *S. brevistylum* (1.170) (FPRDI, 1996), 3-, 5-, and 7-year-old *Falcata* trees (0.240, 0.220, and 0.260, respectively) (Alipon et al., 2021), and *A. cumingiana* (0.390) (Villareal et al., 2022a). Sharma et al. (2011) and Kiaei et al. (2014) stated that a Runkel ratio below 1.0 tends to indicate thin-walled fibers with good mechanical strength properties and are considered as the standard values that are relatively favorable in the viewpoint of papermaking. Based on the Runkel ratio results, the fiber of *S. tripinnatum* might be stiff, and difficult to collapse, thus forming bulkier paper with less venue for bonding, and relatively good for general construction purposes, cabinetry, tool handling, and pilings (FPRDI, 1996; Malabrigo and Umali, 2022). A similar observation was noted by Marasigan et al. (2024) on *S. cumini*, a species related to *S. tripinnatum*. They stated that the wood from this species is suitable for various applications, including construction, plywood, flooring, furniture, and pulp and paper production.

3.2.2 Slenderness ratio

The result showed that the highest value of slenderness ratio was recorded in D_3 (61.650), followed by D_2 (56.370), and D_1 (54.880) with the same trend of result to Runkel ratio. As for wood types, stemwood (54.833) recorded a 0.580% higher slenderness ratio than branchwood (54.513). This result corroborates the findings of Kiaei et al. (2014) on Plumwood exhibiting higher stemwood value (73.280) than branchwood (58.850). However, the analysis showed a comparable result (p-value of 0.877). The present result was relatively higher than those of 3-, 5-, and 7-year-old *Falcata* trees (34.330, 31.980, and 31.900, respectively) (Alipon et al., 2021), and *A. cumingiana* (30.950) (Villareal et al., 2022a). Moreover, the slenderness result of *S. tripinnatum* was within the acceptable value for papermaking which is 33 and above (Kiaei et al., 2014). This result further suggests the suitability of *S. tripinnatum* fibers for papermaking manufacture. Compared to Falcata trees and *A. cumingiana*, composite board made from *S. tripinnatum* could potentially have a higher modulus of elasticity and rupture, owing to its higher slenderness ratio (Ayrilmis et al., 2017).

3.2.3 Flexibility ratio (%)

Opposite to runkel and slenderness ratios, the sample with a larger stem diameter recorded the smallest value of 30.070% (D_3), while the D_1 with a smaller stem diameter recorded the highest value of 38.370% flexibility ratio. Likewise, the stemwood flexibility ratio (34.017%) was 7.350% lower than branchwood (36.520%). This result conforms to the findings of Kiaei et al. (2014) that branchwood (48.580%) showed a relatively higher flexibility ratio than stemwood (41.380%). However, this difference in the present result was not significant with a p-value of 0.272. Also, *S. tripinnatum* result was lower compared to 3-, 5-, and 7-year-old *Falcata* trees (81.990%, 82.780%, and 82.840%, respectively) (Alipon et al., 2021), and *A. cumingiana* (72.310 %) (Villareal et al., 2022a). Based on the flexibility groupings developed by Bektas et al. (1999), *S. tripinnatum* wood fibers were considerably rigid, signifying less efficiency and might require more chemicals to process and breakdown lignin component. Technically, the flexibility ratio underscores the potential of fibers to collapse during the beating of the paper web which greatly provides more bonding area (Zobel and Van Buijtenen, 1989). With higher flexibility ratio, it is expected to display higher tensile strength (Hartono et al., 2022).

3.2.4 Mulhsteph ratio (%)

The highest value of Mulhsteph ratio was recorded in D_3 with 91.115%, followed by D_2 (86.807%) and D_1 (84.444%). Further, stemwood with 8.387% Mulhsteph ratio showed a 1.990% higher than branchwood having 86.623% Mulhsteph ratio. Statistically, the result showed no significant difference (p-value of 0.275) indicating comparable Mulhsteph ratios of stemwood and branchwood. Based on the classification used by Hartono et al. (2022), the *S. tripinnatum* mulhsteph ratio falls in

quality class III which is considered a high value that tends to produce a plastic paper which difficult to tear when folded. The result of the study was in the same class (quality class III) of *Dendrocalamus asper* (Schult.) Backer (Hartono et al., 2022), *Dendrocalamus strictus* (Roxb.) Nees, and *Guadua angustifolia* Kunt. (Marasigan et al., 2024), while the African wood fibers studied by Lestari et al. (2023) fell under quality class I. The value of the Mulhsteph ratio affects the tear and tensile strength, pulp's density, and the smoothness and durability of the paper (Hartono et al., 2022; Lestari et al., 2023).

3.2.5 Rigidity coefficient

The result showed a higher rigidity coefficient in D_3 (0.351), followed by D_2 (0.318) and D_1 (0.303). As to wood types, stemwood with 0.330 rigidity coefficient recorded a 3.030% higher than branchwood having 0.320 rigidity coefficient, although not a significant result. Moreover, this rigidity coefficient result of *S. tripinnatum* falls in quality class III with values greater than 0.15 based on the classification used by Hartono et al. (2022). The result of the study was in the same class (quality class III) *D. strictus* and *G. angustifolia* (Marasigan et al., 2024), while *D. asper* (Hartono et al., 2022) and African wood (Lestari et al., 2023) fell under quality class II. The rigidity coefficient is directly related to paper stiffness while inversely related to paper tensile strength. This means that the higher values of rigidity coefficient resulted to an increased stiffness, while the lower values of rigidity coefficient typically result in better tensile strength (Herlina et al., 2018; Lestari et al., 2023). Fibers with low rigidity coefficient value signify a good value wherein the fiber will be more flexible, and the paper produced will not easily be torn when given a tensile load (Hartono et al., 2022). With the present result, paper made from *S. tripinnatum* fibers seems to display high rigidity and stiffness but might easily tear when given a tensile load.

4. CONCLUSION

This study characterized the fiber morphology (fiber length, fiber diameter, lumen diameter, and cell wall thickness) and derived values (Runkel ratio, slenderness ratio, flexibility ratio, Mulhsteph ratio, and rigidity coefficient) of *S. tripinnatum* stemwood and branchwood. Results revealed that stemwood had thicker cell walls and higher values for the Runkel ratio, slenderness ratio, Mulhsteph ratio, and rigidity coefficient. In contrast, branchwood exhibited longer fibers, larger fiber and lumen diameters and higher flexibility ratio values. However, no significant differences were observed in any properties between stemwood and branchwood. Based on the fiber morphology, *S. tripinnatum* wood fibers are characterized as highly rigid and stiff which difficult to collapse potentially leading to bulkier paper with less bonded area, signifying less efficiency and suitability for pulp and paper requiring more chemicals to process. However, the result also suggested that *S. tripinnatum* wood would be potential for construction purposes, cabinetry, tool handling, and pilings based on the cell wall thickness, Runkel ratio, flexibility ratio, Mulhsteph ratio, and rigidity coefficient results. Farmers who cultivate this tree for fruit production might consider utilizing the wood for various applications or selling it to the wood industry once it reaches senility, rather than converting it to fuelwood. Further, characterization of the basic wood properties (i.e., physical, mechanical, and chemical properties) and technological properties (e.g., machining, veneering, seasoning) of *S. tripinnatum* wood in consideration of the maturity of trees, height levels, greater sample size, and habitat would be relevant information and factors to consider validating its suitability for the intended uses accurately.

ACKNOWLEDGEMENTS

The authors would like to express sincere thanks to the faculty and staff of the College of Agroforestry and Forestry, Don Mariano Marcos Memorial State University - North La Union Campus, and to the College of Forestry and Environmental Studies, Mindanao State University - Maguindanao for the technical assistance.

AUTHOR CONTRIBUTIONS

(1) Conception and design of study: Jayric F. Villareal, Cindy E. Poclis, Mark Gerry B. Barron, Reymark P. Rivera, Oliver S. Marasigan

(2) Acquisition of data: Jayric F. Villareal, Mark Gerry B. Barron

(3) Analysis and/or interpretation of data: Jayric F. Villareal, Cindy E. Poclis, Oliver S. Marasigan

(4) Drafting the manuscript: Jayric F. Villareal, Cindy E. Poclis, Mark Gerry B. Barron, Reymark P. Rivera, Oliver S. Marasigan

(5) Revising the manuscript for significant intellectual content: Jayric F. Villareal, Cindy E. Poclis, Oliver S. Marasigan

(6) Approval of the version of the manuscript to be published: Jayric F. Villareal, Cindy E. Poclis, Oliver S. Marasigan

DECLARATION OF COMPETING INTERESTS

The authors declare no conflict of interest.

REFERENCES

Alipon MA, Alcachupas PL, Bondad EO, Cortiguerra EC. Assessing the utilization of Falcata [*Falcataria moluccana* (Miq.) Barneby & J. W. Grimes] for lumber production. Philippine Journal of Science 2016;145(3):225-35.

Alipon MA, Bondad EO, Gilbero DM, Jimenez JP, Emmanuel PD, Marasigan OS. Anatomical properties and utilization of 3-, 5-, and 7-yr-old Falcata (*Falcataria moluccana* Miq. Barneby & J.W. Grimes) from CARAGA Region, Mindanao Philippines. Philippine Journal of Science 2021;150(5):1307-19.

Ayrilmis N, Akbulut T, Yurttaş E. Effects of core layer fiber size and face-to-face core layer ratio on the properties of three-layered fiberboard. BioResources 2017;12(4):7964-74.

Bektas I, Tutus A, Eroglu H. A study of the Suitability of Calabrian Pine (*Pinus brutia* Ten.) for Pulp and Paper Manufacture. Turkish Journal of Agriculture and Forestry 1999;23(3):589-99.

Coronel RE. Collection, Propagation and Conservation of Indigenous Fruits in thePhilippines. Acta Hortic 2002; 575:211-9.

Del Castillo MC. Philippine Wood Products Report. United States Department of Agriculture, Foreign Agricultural Service; 2021.

Dulay ED, Codilan AL, Galang MA, Tiburan CL, Veran GML, Balonga BP, et al. Diversity and conservation status of indigenous fruit trees in selected mountains of CALABARZON, Philippines. Ecosystems and Development Journal 2023;13(2):77-90.

Forest Products Research and Development Institute (FPRDI). Utilization of Lesser-Used Species (LUS) as Alternative Raw Materials for Forest-Based Industries. Japan: International Tropical Timber Organization (ITTO); 1996.

Hartono R, Purba FVA, Iswanto A, Priadi T, Sutiawan J. Fiber quality of yellow bamboo (*Bambusa vulgaris* vitata) from forest area with special purpose Pondok, Buluh, Simalungun Regency, North Sumatera Province. IOP Conference Series: Earth and Environmental Science 2022;1115(1):1315-755.

Herlina, Istikowati WT, Fatriani. Chemical analysis and fiber of pandan rasau (*Pandanus helicopus*) as an alternative raw material for paper pulp. Journal of the Sylva Scientaeae 2018;1(2):150-9.

Izani MAN, Sahri MH. Wood and cellular properties of four new Hevea species. Proceedings of the FORTROP II International Conference; Bangkok, Thailand; 2008.

Jamovi Project. Jamovi (Version 2.3) [Internet]. 2022 [cited 2024 Jul]. Available from: https://www.jamovi.org.

Kartikawati E, Bienitta, Prastiwi FW, Nugroho WD. Determination of the boundary between juvenile-mature wood of *Diospyros kaki* and their wood anatomical variations. Journal of the Korean Wood Science and Technology 2024;52(2):191-203.

Kiaei M, Tajik M, Vaysi R. Chemical and biometrical properties of plumwood and its application in pulp and paper production. Ciencia y tecnología 2014;16(3):313-22.

Lestari D, Ningsih RV, Fahrussiam F. Anatomical properties and quality of african wood fiber as a raw material for pulp and paper. Perennial 2023;19(2):17-22.

Madsen B, Brondsted P, Andersen TL. Biobased Composites: Materials and Potential Applications as Wind Turbine Blade Materials. Advances in Wind Turbine Blade Design and Materials. Amazon; 2013. p. 363-86.

Malabrigo PL, Umali AGA. Alay: Philippine Native Trees at the Victor O. Ramos Arboretum. Philippine Native Tree Enthusiasts (PNTE). Quezon City: 2022. p. 1-322.

Marasigan OS, Alipon MA, Bondad EO. Senile fruit-bearing trees as possible timber alternative: Physical and mechanical properties. Journal of Tropical Forest Science 2023;35(3):350-65.

Marasigan OS, Alipon MA, Bondad EO, Hopia KA, Mundin MAM. Physical and mechanical properties of thirteen senile fruit-bearing trees in the Philippines and their potential uses. Journal of Tropical Forest Science 2024;36(1):91-104.

NagarajaGanesh B, Rekha B. Intrinsic cellulosic fiber architecture and their effect on the mechanical properties of hybrid composites. Archives of Civil and Mechanical Engineering 2020;20(4):1-12.

Salehi K. Study and Determine the Properties of Chemi-Mechanical Pulping High Yields from bagasse. Wood and Paper Research No. 232, Research Institute of Forests and Rangelands; 2001.

Sharma AK, Dutt D, Upadhyaya JS, Roy TK. Anatomical, morphological, and chemical characterization of *Bambusa tulda*, *Dendrocalamus hamiltonii*, *Bambusa balcooa*, *Malocana baccifera*, *Bambusa arundinaceae*, and *Eucalyptus tereticornis*. Bioresources 2011;6(4):5062-73.

Suansa NI, Al-Mefarrej HA. Branchwood properties and potential utilization of this variable resource. Bioresources 2020; 15(1):479-91.

Sun M, Cao C, Zuo L, Yue X, Zhan M, Xu B. Study on basic wood properties of critically endangered species *Syzygium album*. Wood Research 2023;68(1):1-16.

Thumm A, Dickson AR. The influence of fibre length and damage on the mechanical performance of polypropylene/wood pulp composites. Composites Part A: Applied Science and Manufacturing 2013;46(1):45-52.

Villareal JF, Abasolo WP, Mendoza RC, Maldia LSJ. Fiber morphology and extractive content of *Aquilaria cumingiana* (Decne.) Ridl. wood from Davao Oriental, Philippines. Philippine Journal of Science 2022a;151(5):1623-31.

Villareal JF, De Guzman WB, Cortado JG, Poclis CE. Fiber morphology of Arangen (*Ganophyllum falcatum* Blume) stemwood and branchwood in San Gabriel, La Union, Philippines. Ecosystems and Development Journal 2022b;12(2):97-102.

Wangkhem M, Sharma M, Sharma CL. Comparative wood anatomical properties of genus *Syzygium* (Family Myrtaceae) from Manipur, India. Indonesian Journal of Forestry Research 2020;7(1):27-42.

Wheeler EA, Baas P, Gasson PE. IAWA list of microscopic features for hardwood identification. IAWA Bulletin 1989;10(3):219-332.

Yahaya MIB. Quality assessment of two timber latex clones of rubberwood (*Hevea brasiliensis*) [dissertation]. Serdang, Malaysia: Faculty of Forestry, University of Putra Malaysia; 2001.

Zobel BJ, Van Buijtenen JP. Wood Variation: Its Causes and Control. Berlin, Heidelberg, New York: Springer-Verlag; 1989.

Environment and Natural Resources Journal

Volume 23
Issue 2
2025

Microplastic Pollution in an Urban Wastewater Treatment Plant: Unravelling Problems and Proposing Solutions

Anh Tuan Ta[1,2], Sandhya Babel[3*], Lukas Klocke[4], and Andreas Haarstick[4]

[1]*Department of Sanitary Engineering, Faculty of Public Health, Mahidol University, Bangkok 10400, Thailand*
[2]*Center of Excellence on Environmental Health and Toxicology (EHT), OPS, MHESI, Bangkok, Thailand*
[3]*School of Biochemical Engineering and Technology, Sirindhorn International Institute of Technology, Thammasat University, P.O. Box 22, Pathum Thani 12121, Thailand*
[4]*Institute for Sanitary and Environmental Engineering, Technical University of Braunschweig, Beethovenstr. 51a, 38106 Braunschweig, Germany*

ARTICLE INFO

Received: 29 Mar 2024
Received in revised: 2 Dec 2024
Accepted: 16 Jan 2025
Published online: 10 Feb 2025
DOI: 10.32526/ennrj/23/20240092

Keywords:
Microplastics/ Wastewater treatment/ Removal efficiency/ Granulated activated carbon/ Tertiary treatment

*** Corresponding author:**
E-mail: sandhya@siit.tu.ac.th

ABSTRACT

Microplastics (MPs) are detected ubiquitously in aquatic environments worldwide, with wastewater treatment plants (WWTPs) serving as significant pathways for their entry. This study investigates MP removal efficiency and suggests improvements in a conventional municipal WWTP in Bangkok, Thailand. Wastewater samples were collected using a volume-reduced method and filtered into three size ranges (0.05-0.5, 0.5-1.0, and 1.0-5.0 mm). Particles bigger than 0.5 mm were assessed for abundance using an optical microscope and identified for polymer types using attenuated total reflection Fourier transform infrared (ATR-FTIR) spectroscopy, while smaller particles were analyzed using fluorescence microscopy and micro-FTIR. The average concentration of MPs entering the WWTP was 16.55±9.92 MPs/L, whereas the concentration discharged into the environment was 3.52±1.43 MPs/L. The resultant MP removal efficiency of the Bangkok WWTP stands at approximately 78%, a figure lower than that of WWTPs in developed countries. This discrepancy is attributed to the absence of a primary clarifier within the Bangkok WWTP and an under-designed grit channel. Thus, the implementation of a filter system using activated carbon is suggested. Based on the calculations, 21 filter units are required for the Bangkok WWTP to improve MPs' removal effectiveness. This study provides vital data on the presence of MPs in a Bangkok WWTP, emphasizing challenges that impede effective removal efficiency. Additionally, this study proposes potential solutions to enhance the removal of MPs and address these issues.

1. INTRODUCTION

Plastics have become integral to various aspects of human life, including packaging, textiles, construction, consumer goods, transportation, industrial processes, and medical uses. These items enhance our lives by providing increased comfort, convenience, and safety. The global production of plastics reached approximately 404.3 million tonnes in 2022 (PlasticsEurope, 2023). This results in continuously growing plastic waste entering freshwater and marine ecosystems. Recently, significant focus has been placed on distributing small-sized plastic particles, microplastics (MPs). MPs are plastic particles less than 5 mm in diameter and exist in two distinct forms: primary and secondary. Resin pellets and microbeads used in cosmetics are examples of primary MPs that are purposefully produced in this size range. Conversely, secondary MPs are generated from the breakdown of larger plastic materials through physical and chemical degradation processes (Ta et al., 2025).

Organisms ingest MPs because they cannot differentiate between MPs and actual prey or ingest other organisms containing MPs (De Sá et al., 2015;

Citation: Ta AT, Babel S, Klocke L, Haarstick A. Microplastic pollution in an urban wastewater treatment plant: Unravelling problems and proposing solutions. Environ. Nat. Resour. J. 2025;23(2):185-195. (https://doi.org/10.32526/ennrj/23/20240092)

Ta et al., 2022). This could lead to physical harm for organisms, encompassing digestive system disruptions, hormone level imbalances, decreased feeding efficiency, and potential repercussions on reproductive processes (Carr et al., 2012; Lusher et al., 2013). The interaction between MPs and harmful substances presents another significant ecological concern. Due to their small size and high surface area-to-volume ratio, MPs effectively adsorb hazardous compounds onto their surfaces (De Sá et al., 2018; Ta and Babel, 2023a). These particles can transport toxic substances across long distances and accumulate within organisms after ingestion (Bakir et al., 2016). Additionally, MPs act as vectors for pathogens by providing surfaces for their attachment (Viršek et al., 2017). Studies have revealed that pathogens can form colonies on MP particles in marine environments (Kirstein et al., 2016).

An important pathway of MP input into aquatic environments has been found through WWTPs (Horton et al., 2017). Wastewater entering WWTPs originates from households, businesses, institutions, and occasionally urban rainwater overflow. These wastewater sources contain various types of MPs, such as microbeads and microfibers. Microbeads are commonly found in personal care products like toothpaste and face scrubs. Meanwhile, synthetic garments made from polyester and nylon can release hundreds of microfibers into wastewater during washing (Ta and Babel, 2020).

Recent research has focused on improving the detection, removal, and management of MPs in WWTPs, addressing the growing concerns over their environmental and human health impacts. Advances in sampling and analytical methods have significantly enhanced the reproducibility and applicability of MP detection in WWTPs, with improvements in techniques like Fourier-transform infrared spectroscopy (FTIR) and Raman spectroscopy (Sadia et al., 2022; Ta and Promchan, 2024). In terms of removal technologies, preliminary and primary treatments are effective at removing MPs through physical processes. For example, MPs can be removed from raw wastewater during the grit and grease removal stage, with studies showing up to 79% removal efficiency in countries like Australia (Ziajahromi et al., 2021) and 69% in the UK (Murphy et al., 2016). Air flotation technology captures low-density MPs, while polyethylene (PE) microbeads can be skimmed off easily due to their buoyancy (Murphy et al., 2016). Primary treatment mainly eliminates MPs through sedimentation, where larger MPs settle in solid flocs. However, some studies from China suggest that grit and grease chambers are less effective than sedimentation (Liu et al., 2021). Combining grit and grease stage with primary sedimentation can enhance MP removal rates, with sedimentation achieving reductions of 91.7% in Vancouver, Canada, and 71.67% in Beijing, China (Gies et al., 2018; Liu et al., 2019). Factors like the density and morphology of MPs significantly affect removal efficiency, with fibers being particularly challenging to retain (Long et al., 2019). Secondary treatment utilizes biological processes to degrade suspended particles and dissolve solids in wastewater, causing MPs to accumulate within sludge flocs. In the activated sludge process, smaller MPs (106-300 µm) are more readily removed than larger ones (>300 µm) (Lee and Kim, 2018). However, configurations like the anaerobic-anoxic-oxic process show lower MP removal rates, with significant recirculation of MPs back into the aqueous phase (Liu et al., 2021). Tertiary treatment technologies enhance MP removal efficiency by 5-20%. Membrane bioreactors demonstrated up to 99.9% removal efficiencies in various studies (Talvitie et al., 2017). Sand filtration has shown a 97% removal rate, while advanced oxidation processes like ozonation significantly degrade MP structures, leading to high removal rates (Chen et al., 2018; Hidayaturrahman and Lee, 2019). However, not all advanced treatments effectively reduce MP concentrations, especially for smaller particles (Sutton et al., 2016).

While WWTPs in many parts of the world are achieving high MP removal rates, the situation is different in urban areas of developing countries, where rapid urbanization and inadequate upgrades to treatment technologies have led to overloaded systems with lower removal efficiencies (Chirisa et al., 2017; Nguyen et al., 2023; Zhang et al., 2016). Although primary and secondary treatment processes in well-functioning WWTPs can remove up to 99% of MPs (Murphy et al., 2016; Ta and Promchan, 2024), many of these facilities in developing countries struggle to achieve such performance levels. To address these challenges, research has explored the installation of activated carbon or biochar filters as a cost-effective solution, particularly suited for regions where these materials are abundant as agricultural byproducts (Lewoyehu, 2021). Studies indicate that granular activated carbon (GAC) filters are promising for removing MPs from wastewater. For example, Amirah Mohd Napi et al. (2023) demonstrated that GAC could

remove up to 95.5% of MPs that range in size from 40 to 48 μm. Similarly, Kim and Park (2021) documented the effectiveness of GAC in a Korean WWTP as a tertiary treatment step, where a pilot-scale GAC filtration tower (10 m^3/day) achieved an MPs removal efficiency of 92.8%. In a larger pilot-scale GAC filtration system with a flow rate of 12 m^3/h (288 m^3/day), Sturm et al. (2023) reported removal efficiencies of 86.2% for both MPs and other micropollutants. These studies validate the use of GAC as an effective tertiary treatment option and indicate its feasibility for large-scale applications in wastewater management. The evidence presented in the literature supports the rationale for employing GAC as a critical component in advancing wastewater treatment technologies, especially in tackling the escalating issue of MP pollution.

The primary objective of this study is to evaluate the efficiency of MP removal in a conventional municipal WWTP from a developing country (Thailand) in the Southeast Asia Region. The abundance and properties of MPs in each unit operation of the WWTP were also examined. A comparison of the MP removal effectiveness in the studied WWTP and others from developed countries was conducted to indicate the advantages and disadvantages of the WWTPs. Then, a suggestion for improvement of MP removal in the studied WWTP by activated carbon filter is evaluated.

2. METHODOLOGY

2.1 Study sites and sampling

A conventional WWTP in Thailand was selected for investigation in this study. The WWTP serves an area of 37 km^2 with a population of about 1 million. The plant has a capacity of 350,000 m^3/day and uses the treatment technology of a biologically activated sludge process with nutrient removal. A flow diagram of the WWTP treatment processes is shown in Figure 1. Treated water is discharged into surrounding canals.

MP samples were collected at three points on the WWTP, including influent (S1), after grit channels (S2), and effluent (S3). Samples were collected using a volume-reduced method through on-site filtration. At each sampling point, triplicate 20 L wastewater samples were filtered through a 0.05 mm mesh sieve (n=3). The remaining materials on the sieve were rinsed with deionized water and then transferred into laboratory glass bottles for storage (Duran, 1 L).

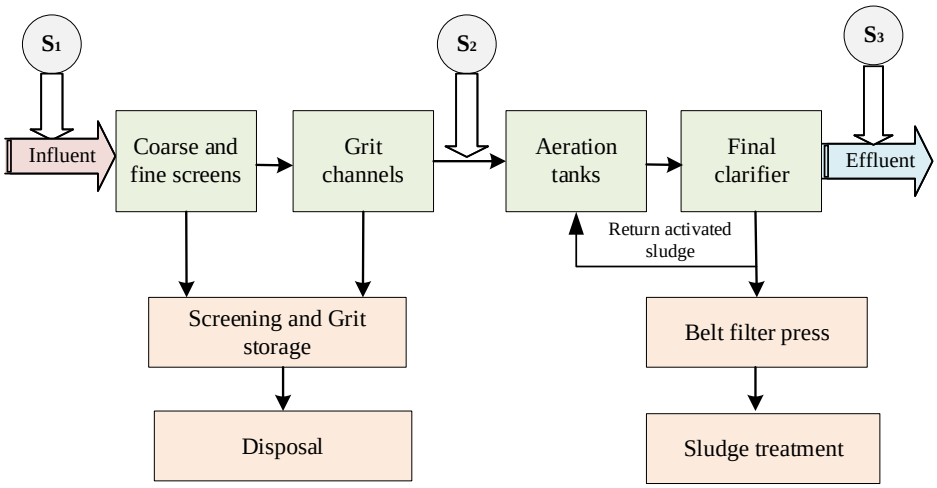

Figure 1. Flow diagram of the selected WWTP with sampling locations

2.2 Samples analysis

At the laboratory, MPs in wastewater were extracted and examined following the method suggested by Tadsuwan and Babel (2022), as shown in Figure 2. Particles in the wastewater samples were categorized into three size ranges: 0.05-0.50, 0.5-1.0, and 1.0-5.0 mm using sieves made of stainless steel. Fractions containing particles bigger than 0.5 mm (retained on 0.5 mm and 1.0 mm sieve meshes) were visually examined. Suspected plastic particles within this size range were manually removed using stainless-steel tweezers and transferred onto Petri dishes. The fractions with particles smaller than 0.5 mm in size (retained on 0.5 mm and 1.0 mm sieve meshes) were more challenging to examine visually due to their small size and the presence of sediment and organic debris. Thus, the organic debris was removed using Fenton's reagent (composed of 20 mL

of 30% H_2O_2 and 20 mL of 0.05 M $FeSO_4 \cdot 7H_2O$). The treated particles were then subjected to density separation using sodium iodide (NaI), which has a 1.5 g/cm³ density. The samples were combined with NaI solution and stirred thoroughly for 15 min. After settling for 24 h, the buoyant solids were carefully collected and passed through a 0.45 µm pore-size cellulose nitrate membrane filter.

Following pre-treatment, particles within the size ranges of 1.0-5.0 and 0.5-1.0 mm were visually assessed using an optical microscope (Olympus CX41). Polymer types were identified utilizing ATR-FTIR spectroscopy (Thermo Scientific - Nicolet iS50). Particles sized between 0.05 and 0.5 mm were split into two groups and filtered using the Whatman cellulose nitrate membranes (0.45 µm pore size). Due to their smaller dimensions, this size range posed a risk of underestimation when analyzed with an optical microscope. To address this, a Nile Red solution was prepared by dissolving Nile Red in chloroform at a concentration of 1 mg/mL, which was then used to stain the first set (Ta and Babel, 2023b). The stained filters were then analyzed using a fluorescence microscope (GE Healthcare - Delta Vision™ Elite Cell) to quantify MPs. The fluorescence microscope was equipped with a DAPI (4',6-diamidino-2-phenylindole) filter, facilitating visualization based on fluorescence properties. The setup was configured for blue fluorescence, utilizing an emission wavelength of 435/48 nm and an excitation wavelength of 390/18 nm to selectively detect fluorescently labeled particles. Images of the filter surfaces were captured at ×4 magnification with a camera attached to the Delta Vision microscope, aiding in identifying MPs. For quantification, visible fluorescent spots in the images were counted, with each spot corresponding to an individual MP particle. Micro-FTIR spectroscopy (Thermo Scientific - Nicolet iN10) was employed to determine polymer types for the second set of filters. The analysis was performed in ATR mode, with an aperture size ranging from 50 to 300 µm in height and length. The spectroscopy has an 8 cm^{-1} resolution and 64 scans encompassing a 4,000 to 650 cm^{-1} range. Using OMNIC Spectra Software, the ATR-FTIR and micro-FTIR spectra were compared to a library of polymer spectra, using a 70% minimum matching criterion to determine the types of polymers.

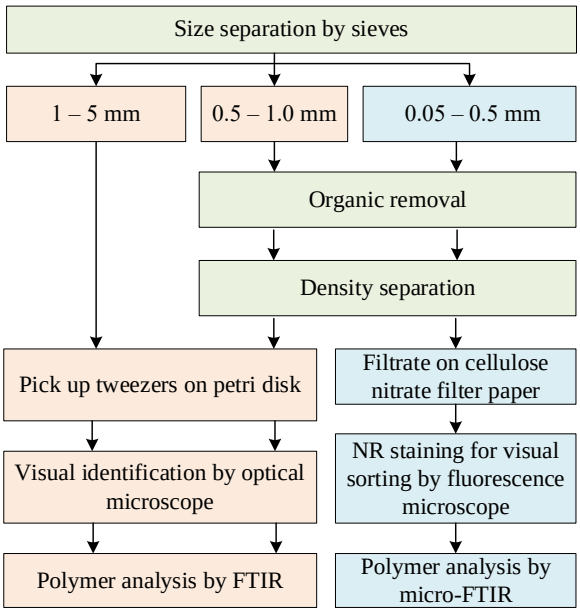

Figure 2. Procedure for analysis of MPs in wastewater samples

3. RESULTS AND DISCUSSION

3.1 Microplastic characteristics and removal efficiency in the studied WWTP

Figure 3(a) illustrates the concentration of MPs per liter of wastewater across various sampling locations, categorized by size classes. On average, 16.55±9.92 MPs/L entered the WWTP, while 3.52±1.43 MPs/L were discharged into the environment. Most MPs were concentrated in the 0.05-0.5 mm size range at the WWTP inlet, with a measured concentration of 12.2 MPs/L. This was followed by the 0.5-1.0 mm size range, which had 4.33 MPs/L, and the 1-5 mm size range, with a concentration of 2.02 MPs/L. Similarly, the final effluent was dominated by MPs in the 0.05-0.50 mm range (2.23 MPs/L), followed by concentrations of 0.75 MPs/L in the 0.5-1.0 mm range and 0.53 MPs/L in the 1-5 mm range.

FT-IR and micro-FTIR fingerprint spectra were compared with reference databases, identifying polyethylene (PE) as the most abundant polymer, followed by polyethylene terephthalate (PET) and acrylic polymers (Figure 3(b)). Transparent fragments and films, frequently composed of PE, were likely linked to its widespread application in packaging and containers. These fragments were classified as secondary MPs, formed through plastic material breakdown and physical degradation.

The removal efficiencies of various size classes across the treatment units are shown in Table 1. The selected WWTP achieved an overall MP removal efficiency of 78.73%. Removal rates by size class were 73.76% for 1-5 mm, 82.68% for 0.5-1.0 mm, and 78.14% for 0.05-0.50 mm. The grit trap removed 47.13% of MPs, while secondary treatment achieved a higher reduction rate of 59.77% across all size ranges compared to earlier processes like screening and grit trapping. MPs in the 1-5 mm range were the least effectively removed after screening. However, the WWTP's daily treatment capacity of 350,000 m³ still releases an estimated 1.23 billion MPs into the environment daily.

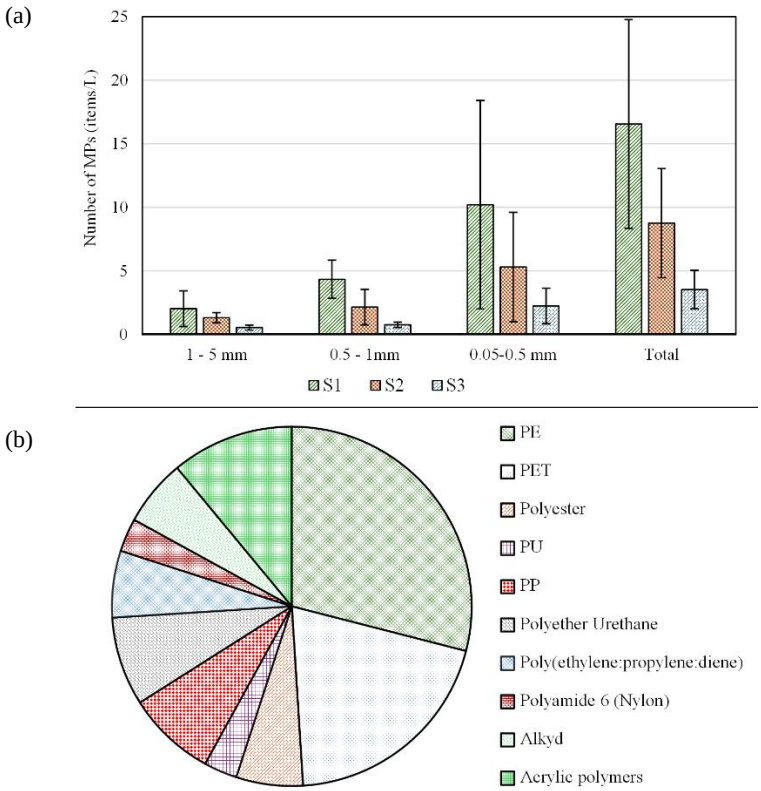

Figure 3. (a) Number of MP particles in each treatment step of the selected WWTP; (b) Polymer types of MPs at all sampling locations in the selected WWTP

Table 1. The efficiency of MP removal across size fractions in treatment units of the selected WWTP

Size range	Removal efficiency (%)		
	Screening and grit chamber	Secondary treatment	Overall
1-5 mm	35.64	59.23	73.76
0.5-1 mm	50.35	65.12	82.68
0.05-0.50 mm	48.04	57.92	78.14
Total	47.13	59.77	78.73

3.2 Comparison of MP removal from different WWTPs

A comparison of MPs extracted from various WWTPs worldwide is shown in Figure 4. The data indicate that the MP removal efficiency in the WWTP from Thailand is much lower than that of others. In a study conducted in South Korea, the wastewater treatment process began with preliminary treatment, which included a grit removal unit and a primary settling tank for screening the wastewater. The secondary treatment utilized a bioreactor containing activated sludge and a secondary settling tank. Tertiary treatment processes were implemented to enhance the removal of residual pollutants. This comprehensive treatment approach achieved an approximately 99% removal efficiency for MPs from the inlet wastewater (Hidayaturrahman and Lee, 2019). The selected WWTP in the Italian study

featured multiple treatment stages, including screening, grit and grease chamber, biological treatment, sedimentation, sand filtration, and disinfection. This facility achieved an overall MP removal efficiency of 84% (Magni et al., 2019). The WWTP in Finland employed treatment technologies comprising primary clarification, a conventional activated sludge process, and rapid sand filtration. The removal efficiency was specifically reported for the rapid sand filtration stage (tertiary treatment), achieving a 97% reduction in MPs from the influent (Talvitie et al., 2017).

There are two main reasons for the selected WWTP's low MP removal efficiency in Thailand compared to the other studies. The first factor pertains to the under-design of the grit channels. Due to the short length of the grit channels, the surface loading with MP particles is too high. Furthermore, the standard flow velocity due to the mixed water inflow should be 25 m/h. However, the flow velocity in the Bangkok WWTP is 32 m/h. This means the MPs do not have enough time to settle or float on the water's surface, where they can be removed from the wastewater stream. The second reason is the missing primary clarifier in the selected WWTP from Thailand. As mentioned above, all the WWTPs have primary clarifiers, while the wastewater in the Thailand WWTP goes directly from the screening and the grit chamber to the secondary treatment (Figure 1). This contributes to a decrease in the WWTP's total MP removal efficiency.

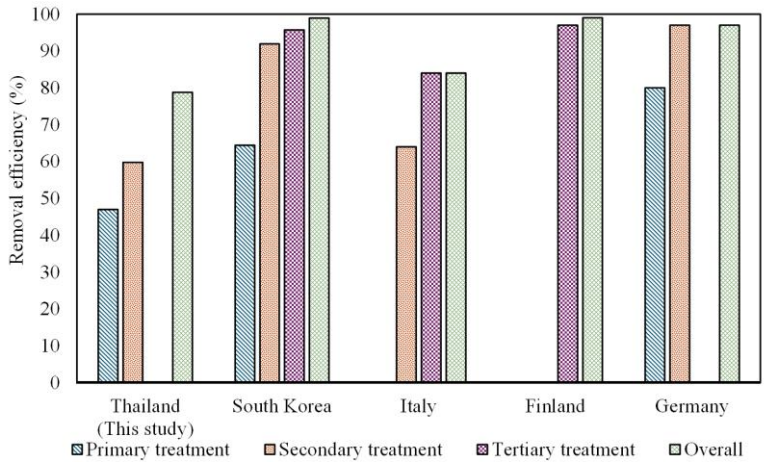

Figure 4. Removal efficiency of MPs in different WWTPs: South Korea (Hidayaturrahman and Lee, 2019), Italy (Magni et al., 2019), Finland (Talvitie et al., 2017), Germany (Mintenig et al., 2017).

3.3 Solutions for improvement of MP removal in the studied WWTP

3.3.1 Activated carbon filters as a potential solution for MP removal

As shown in the above section, most WWTPs from other developed countries are equipped with tertiary treatment. The treatment step has been proven to be an efficient technique for removing MPs. Thus, activated carbon filters are proposed as a tertiary treatment step to improve the MP removal efficiency at the Thailand WWTP. Activated carbon has been used to adsorb various micropollutants in wastewater, such as antibiotics, X-ray contrast medium, beta-blockers, and other human pharmaceuticals (Gidstedt et al., 2022; Khalidi-Idrissi et al., 2023). Since MPs also include sizes of <100 µm, activated carbon filters are proposed here as an efficient method to reduce the MPs in the WWTP effluent. According to Benstöm (2017), the parameters influencing activated carbon's adsorption efficiency include the molecular structure, molecular weight, solubility, and polarity of pollutants. In the context of the chemical composition and molecular weights of polymers, MPs can readily adsorb onto the surface of activated carbon, as common MPs found in wastewater are typically insoluble. A study by Wang et al. (2020) shows that activated carbon from biomass provides significant capacity for the removal of 10 µm diameter MPs (above 95%). Given the diverse chemical nature of MPs, the interactions with activated carbon should be studied in detail. This is so that precise knowledge can be gained of the required filtering characteristics to optimize the removal performance of granulated activated carbon (GAC) filters. However, no institutionalized guidelines for designing GAC filter units are published in the literature. The most

important process values for sizing GAC units are L_B (height of filter bed) and filter velocity (v_f). Another relevant parameter is the empty bed contact time (EBCT), which is calculated from v_f and L_B values (Benstöm, 2017). The calculation approach for the dimensioning of a GAC filter unit is shown in Figure 5(a). The filter unit was finally dimensioned using iteration steps based on different filter flow rates.

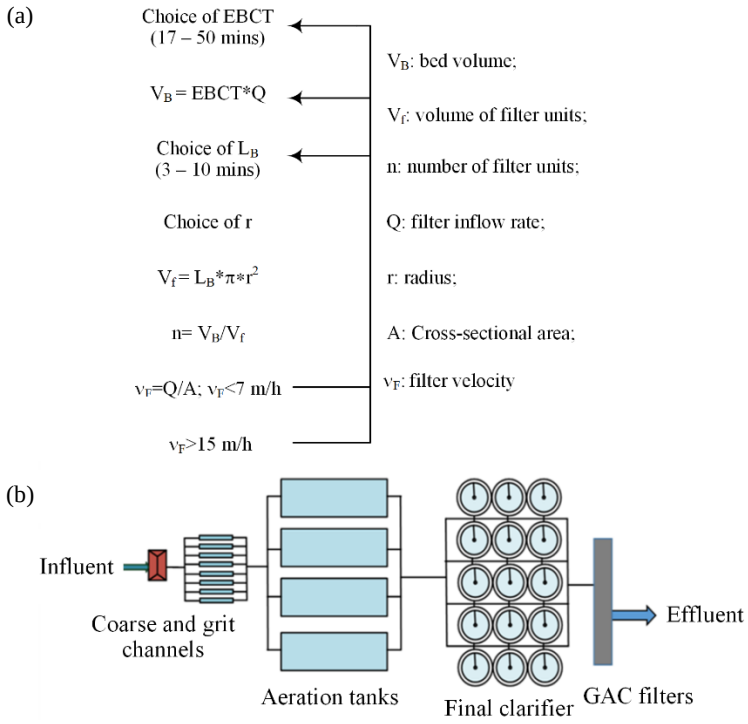

Figure 5. (a) Process of calculation for dimensioning the GAC filter; (b) Flow diagram of the selected WWTP in Bangkok, with the implementation of GAC filters.

3.3.2 Design of GAC filters

The wastewater flow of the Bangkok sewage treatment plant is 341,289 m³/d. The selected contact time is 17 min. If the wastewater flow and the contact time are multiplied, the total filter volume is 4,029 m³. However, to keep the number of filter units small, a filter radius per unit (3.9 m) was used with a filter bed height of 4.3 m. This results in a cross-sectional area of 47.8 m^2 and a filter bed volume per unit of 205 m³. The calculated total volume of 4,029 m^3 divided by the filter volume of one single filter unit (205 m^3) results in 20 filter units. Regarding the proposed parallel operation of the filter units, one filter unit is added to reactivate each filter unit (one after the other) in a certain time sequence. Dividing the total wastewater flow of 341,289 m³/d by 21 filter units results in a daily inflow per individual filter unit of 677 m³/h. Referring to the cross-sectional area of each filter unit (47.8 m^2), the filter velocity is calculated as 14.2 m/h. This value is below 15 m/h, which is reported as the recommended upper limit (Benstöm, 2017).

Figure 5(b) shows the implementation of an activated carbon filter system on the Bangkok WWTP. With the implementation of the GAC units, the wastewater passes through the following treatment stages. First, the influent flows into 8 aerated grit channels. Each of them has a surface of 111 m². Then, the wastewater flows through 4 activated sludge channels of 96×32 m per channel, followed by 15 final clarifiers, each with a diameter of 31 m. The last step is the GAC filter units. Each of them has a radius of 3.9 m. Figure 6(a) shows the arrangement of individual GAC filter units in the selected WWTP. The filter units are arranged in parallel to ensure continuous operation of the plant. Details of the arrangement and the cleaning concept are explained in Section 3.3.

The structure of the GAC filter (Figure 6(b)) consists of granular activated carbon with a mesh size of 8×30 mm (grain diameter: 0.63-2.36 mm). This mesh size is usually used and is successful in many treatment systems (Benstöm, 2017). At the bottom of the filtration unit, different granulated activated carbon layers with a 4×8 mm mesh size (grain diameter: 2.36-4.75 mm) are installed. This layer prevents upper-layer GAC particles from being washed out of the filter unit and reaching surface waters.

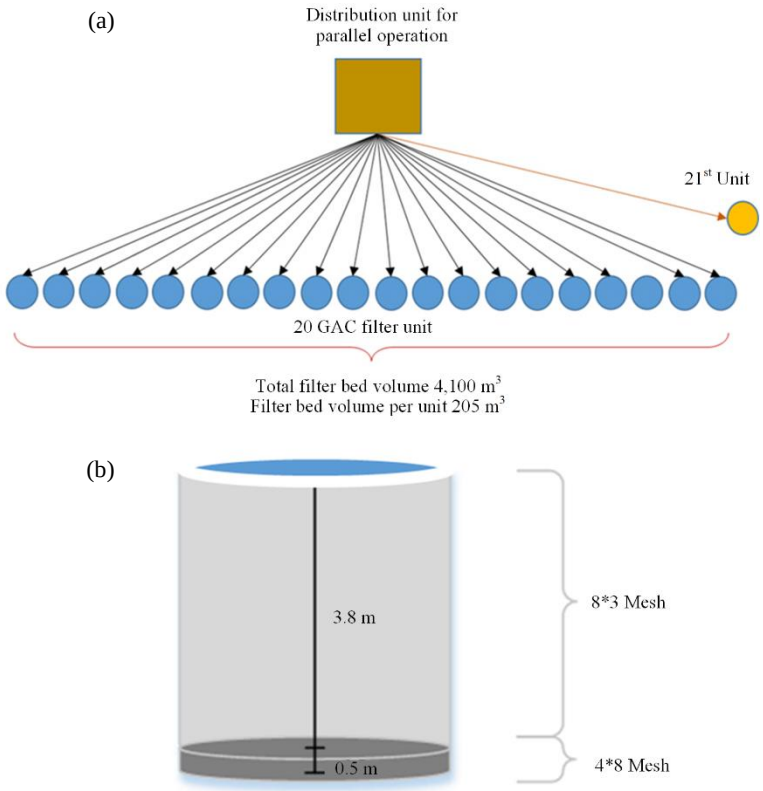

Figure 6. (a) Arrangement of GAC units in parallel operation; (b) Structure of a GAC filter unit

3.3.3 Operation of GAC filters

As shown in Figure 6, 21 units of GAC filters were operated in a parallel position. This operation removes MPs more efficiently than in serial operation. Parallel operation simplifies the procedure for operating and inspecting. Furthermore, parallel operation is less expensive because it has lower investment and operational costs (e.g., the pressure loss is lower compared to serial operation). Parallel operation also achieves the maximum availability for a load of activated carbon compared to serial operation (Fundneider et al., 2021).

3.3.4 Cleaning of GAC filter unit

The procedure for cleaning is shown in Figure 7. The first cleaning step involves cleaning the GAC filter with an airflow of 60 m/h for 90 s to loosen the material in the filter. The second step is to rinse the filter with clean water at 25 m/h for 300 s to remove pollutants from the filter. The last step is to rinse the filter with water again, but with a higher flow rate and in a shorter time (50 m/h for 180 s). However, the flow rate of cleaning water, which rinses the layers from the bottom to the top, should not exceed 60 m/h. Otherwise, the two layers (Figure 5(b)) would be mixed. It is also important to avoid the influence of abrasion. For example, in the case of lignite, hard coal, and coconut husk when used as the GAC, the abrasion losses are between 0.1 and 1.5 wt.% per year with a daily rinse (Çeçen and Aktas, 2011). Tests with GAC layers over a longer period show that it is sufficient to clean the GAC filter once a week (Çeçen and Aktas, 2011).

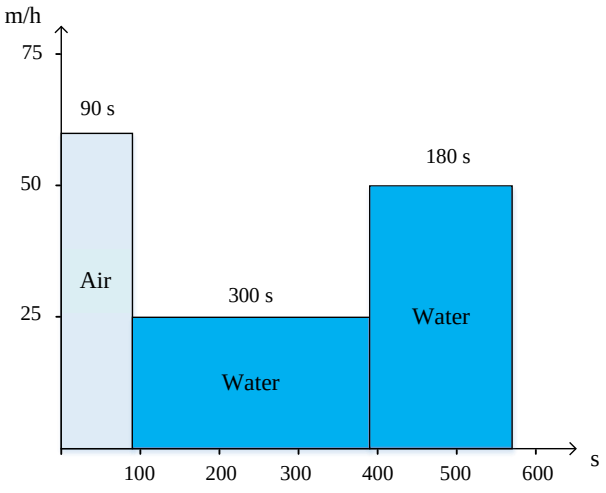

Figure 7. Cleaning of GAC filter unit

3.3.5 Regeneration and reactivation of GAC

The filtering efficiency of GAC decreases over time, necessitating determining when reactivation is required. Filtering efficiency is defined by the ratio of MP concentration in the filter outflow (S) to the MP

concentration in the filter inflow (S0). The filter must be regenerated and reactivated if this ratio reaches 20% (S/S0=0.2). Experimental data for this process typically represented through breakthrough curves, are not readily available in the literature. The "bed volume number" (BVN) is a useful reference to mitigate potential overloading. Typical BVN values range between 22,000 and 31,400 (Çeçen and Aktas, 2011). For the Bangkok WWTP, we assume a BVN of 22,000, corresponding to a throughput of 4,520,327 m^3 (22,000×205 m^3) per filter unit.

To determine the specific timeline for exchanging or reactivating GAC in filters, the normalized throughput volume is divided by the inflow rate per filter unit, calculated as follows: 4,520,327 m^3 / 16,252 m^3/d. The inflow rate is derived from 341,289 m^3/d divided by 21 filter units. Thus, complete reactivation is needed after 278 days. Given the continuous operation of the treatment plant, one filter is reactivated every 13 days while maintaining 20 active filter units.

To establish a sustainable green cycle for GAC, selecting eco-friendly sources for activated carbon is crucial. Activated carbon produced from biomass provides an eco-friendly and cost-efficient substitute for traditional commercial activated carbon. Coconut husk, in particular, is an excellent raw material for activated carbon production, offering a more sustainable option compared to lignin or hard coal (Arena et al., 2016). The production process of activated carbon from coconut husk involves carbonization followed by activation, creating a porous structure that enhances its adsorptive capacity. After reaching the end of its life cycle in the filter, the used GAC can be reactivated through thermal processes, which restore its adsorptive properties and reduce waste. This green cycle minimizes the environmental impact and supports the circular economy by reintroducing reactivated GAC into the filtering system, thereby reducing the need for virgin materials and promoting resource efficiency (Arena et al., 2016).

4. CONCLUSION

MPs were found in all samples from Bangkok's selected WWTP. The average concentration of MPs entering the WWTP was 16.55±9.92 MPs/L, while the concentration in the discharged effluent was 3.52±1.43 MPs/L, indicating an overall removal efficiency of 78.73%. Higher removal rates were observed in the fractions of 0.5-1.0 mm. Despite this, the MP concentration in the treated effluent reveals that significant quantities, amounting to over one billion MPs daily, are still being released into the environment. The MPs' removal efficiency in this Bangkok WWTP is lower than that observed in WWTPs in South Korea, Italy, Finland, and Germany. The main factors influencing this outcome are likely the high flow rates in the grit channels, which hinder MP particle settling or flotation, and the absence of a primary clarifier in the Bangkok WWTP, a key step typically preceding secondary treatment. To address these limitations, this study proposes implementing GAC filters as a tertiary treatment step to enhance MP removal in the Bangkok WWTP. This recommendation includes detailed guidance on GAC filters' design, operational procedures, and regeneration processes. Since WWTPs serve as one of the primary routes through which MPs are released into the environment, this study provides essential data on MP occurrence in a Bangkok WWTP in one of Asia's major cities. Additionally, it highlights the challenges impeding MP removal efficiency and proposes solutions that could be adapted to other developing Asian countries facing similar challenges.

ACKNOWLEDGEMENTS

The authors would like to thank the academic collaboration between the Technische Universität Braunschweig and Sirindhorn International Institute of Technology, Thammasat University, and the DAAD Exceed-Swindon project for the support. This research project was supported by the Thailand Science Research and Innovation Fundamental Fund fiscal year 2024, Thammasat University.

REFERENCES

Amirah Mohd Napi Nn, Ibrahim N, Adli Hanif M, Hasan M, Dahalan FA, Syafiuddin A, et al. Column-based removal of high concentration microplastics in synthetic wastewater using granular activated carbon. Bioengineered 2023;14(1):Article No. 2276391.

Arena N, Lee J, Clift R. Life Cycle Assessment of activated carbon production from coconut shells. Journal of Cleaner Production 2016;125:68-77.

Bakir A, O'Connor IA, Rowland SJ, Hendriks AJ, Thompson RC. Relative importance of microplastics as a pathway for the transfer of hydrophobic organic chemicals to marine life. Environmental Pollution 2016;219:56-65.

Benstöm F. Granular Activated Carbon for the Elimination of Organic Micropollutants form Municipal Wastewater [dissertation]. Germany: RWTH Aachen University; 2017.

Carr KE, Smyth SH, McCullough MT, Morris JF, Moyes SM. Morphological aspects of interactions between microparticles

and mammalian cells: Intestinal uptake and onward movement. Progress in Histochemistry and Cytochemistry 2012;46(4):185-252.

Çeçen F, Aktas Ö. Activated Carbon for Water and Wastewater Treatment: Integration of Adsorption and Biological Treatment. John Wiley and Sons; 2011.

Chen R, Qi M, Zhang G, Yi C. Comparative experiments on polymer degradation technique of produced water of polymer flooding oilfield. IOP Conference Series: Earth and Environmental Science 2018;113:Article No. 012208.

Chirisa I, Bandauko E, Matamanda A, Mandisvika G. Decentralized domestic wastewater systems in developing countries: The case study of Harare (Zimbabwe). Applied Water Science 2017;7(3):1069-78.

De Sá LC, Luís LG, Guilhermino L. Effects of microplastics on juveniles of the common goby (*Pomatoschistus microps*): Confusion with prey, reduction of the predatory performance and efficiency, and possible influence of developmental conditions. Environmental Pollution 2015;196:359-62.

De Sá LC, Oliveira M, Ribeiro F, Rocha TL, Futter MN. Studies of the effects of microplastics on aquatic organisms: what do we know and where should we focus our efforts in the future? Science of the Total Environment 2018;645:1029-39.

Fundneider T, Alonso VA, Wick A, Albrecht D, Lackner S. Implications of biological activated carbon filters for micropollutant removal in wastewater treatment. Water Research 2021;189:Article No. 116588.

Gidstedt S, Betsholtz A, Falås P, Cimbritz M, Davidsson Å, Micolucci F, et al. A comparison of adsorption of organic micropollutants onto activated carbon following chemically enhanced primary treatment with microsieving, direct membrane filtration and tertiary treatment of municipal wastewater. Science of the Total Environment 2022; 811:Article No. 152225.

Gies EA, LeNoble JL, Noël M, Etemadifar A, Bishay F, Hall ER, et al. Retention of microplastics in a major secondary wastewater treatment plant in Vancouver, Canada. Marine Pollution Bulletin 2018;133:553-61.

Hidayaturrahman H, Lee TG. A study on characteristics of microplastic in wastewater of South Korea: Identification, quantification, and fate of microplastics during treatment process. Marine Pollutution Bulletin 2019;146:696-702.

Horton AA, Walton A, Spurgeon DJ, Lahive E, Svendsen C. Microplastics in freshwater and terrestrial environments: Evaluating the current understanding to identify the knowledge gaps and future research priorities. Science of the Total Environment 2017;586:127-41.

Khalidi-Idrissi A, Madinzi A, Anouzla A, Pala A, Mouhir L, Kadmi Y, et al. Recent advances in the biological treatment of wastewater rich in emerging pollutants produced by pharmaceutical industrial discharges. International Journal of Environmental Science and Technology 2023;20(10):11719-40.

Kim KT, Park S. Enhancing microplastics removal from wastewater using electro-coagulation and granule-activated carbon with thermal regeneration. Processes 2021;9(4):Article No. 617.

Kirstein IV, Kirmizi S, Wichels A, Garin-Fernandez A, Erler R, Loder M, et al. Dangerous hitchhikers? Evidence for potentially pathogenic *Vibrio* spp. on microplastic particles. Marine Environment Research 2016;120:1-8.

Lee H, Kim Y. Treatment characteristics of microplastics at biological sewage treatment facilities in Korea. Marine Pollution Bulletin 2018;137:1-8.

Lewoyehu M. Comprehensive review on synthesis and application of activated carbon from agricultural residues for the remediation of venomous pollutants in wastewater. Journal of Analytical and Applied Pyrolysis 2021;159:Article No. 105279.

Liu W, Zhang J, Liu H, Guo X, Zhang X, Yao X, et al. A review of the removal of microplastics in global wastewater treatment plants: Characteristics and mechanisms. Environment International 2021;146:Article No. 106277.

Liu X, Yuan W, Di M, Li Z, Wang J. Transfer and fate of microplastics during the conventional activated sludge process in one wastewater treatment plant of China. Chemical Engineering Journal 2019;362:176-82.

Long Z, Pan Z, Wang W, Ren J, Yu X, Lin L, et al. Microplastic abundance, characteristics, and removal in wastewater treatment plants in a coastal city of China. Water Research 2019;155:255-65.

Lusher AL, McHugh M, Thompson RC. Occurrence of microplastics in the gastrointestinal tract of pelagic and demersal fish from the English Channel. Marine Pollutution Bulletin 2013;67(1-2):94-9.

Magni S, Binelli A, Pittura L, Avio CG, Della Torre C, Parenti CC, et al. The fate of microplastics in an Italian Wastewater Treatment Plant. Science of the Total Environment 2019; 652:602-10.

Mintenig SM, Int-Veen I, Löder MG, Primpke S, Gerdts G. Identification of microplastic in effluents of waste water treatment plants using focal plane array-based micro-Fourier-transform infrared imaging. Water Research 2017;108:365-72.

Murphy F, Ewins C, Carbonnier F, Quinn B. Wastewater treatment works (WwTW) as a source of microplastics in the aquatic environment. Environmental Science and Technology 2016;50(11):5800-8.

Nguyen P-D, Tran Q-V, Le T-T, Nguyen Q-H, Kieu-Le T-C, Strady E. Evaluation of microplastic removal efficiency of wastewater-treatment plants in a developing country, Vietnam. Environmental Technology and Innovation 2023;29:Article No. 102994.

PlasticsEurope. Plastics - the Fast Facts 2023. Brussels, Belgium: Plastics Europe; 2023.

Sadia M, Mahmood A, Ibrahim M, Irshad MK, Quddusi AHA, Bokhari A, et al. Microplastics pollution from wastewater treatment plants: A critical review on challenges, detection, sustainable removal techniques and circular economy. Environmental Technology and Innovation 2022;28:Article No. 102946.

Sturm MT, Myers E, Schober D, Korzin A, Thege C, Schuhen K. Comparison of AOP, GAC, and novel organosilane-based process for the removal of microplastics at a municipal wastewater treatment plant. Water 2023;15(6):Article No. 1164.

Sutton R, Mason SA, Stanek SK, Willis-Norton E, Wren IF, Box C. Microplastic contamination in the San Francisco bay, California, USA. Marine Pollution Bulletin 2016;109(1):230-5.

Ta AT, Babel S. Microplastics pollution with heavy metals in the aquaculture zone of the Chao Phraya River Estuary, Thailand. Marine Pollutution Bulletin 2020;161:Article No. 111747.

Ta AT, Babel S. Microplastics and heavy metals in a tropical river: Understanding spatial and seasonal trends and developing

response strategies using DPSIR framework. Science of the Total Environment 2023a;897:Article No. 165405.

Ta AT, Babel S. Occurrence and spatial distribution of microplastic contaminated with heavy metals in a tropical river: Effect of land use and population density. Marine Pollutution Bulletin 2023b;191:Article No. 114919.

Ta AT, Babel S, Wang LP. Prevalence and characteristics of microplastic contamination in soft drinks and potential consumer exposure. Journal of Environmental Management 2025;373:Article No. 123810.

Ta AT, Promchan N. Microplastics in wastewater from developing countries: A comprehensive review and methodology suggestions. TRAC Trends in Analytical Chemistry 2024; 171:Article No. 117537.

Ta AT, Pupuang P, Babel S, Wang LP. Investigation of microplastic contamination in blood cockles and green mussels from selected aquaculture farms and markets in Thailand. Chemosphere 2022;303:Article No. 134918.

Tadsuwan K, Babel S. Unraveling microplastics removal in wastewater treatment plant: A comparative study of two wastewater treatment plants in Thailand. Chemosphere 2022;307:Article No. 135733.

Talvitie J, Mikola A, Koistinen A, Setälä O. Solutions to microplastic pollution-Removal of microplastics from wastewater effluent with advanced wastewater treatment technologies. Water Research 2017;123:401-7.

Viršek MK, Lovšin MN, Koren Š, Kržan A, Peterlin M. Microplastics as a vector for the transport of the bacterial fish pathogen species *Aeromonas salmonicida*. Marine Pollution Bulletin 2017;125(1-2):301-9.

Wang Z, Sedighi M, Lea-Langton A. Filtration of microplastic spheres by biochar: Removal efficiency and immobilisation mechanisms. Water Research 2020;184:Article No. 116165.

Zhang QH, Yang WN, Ngo HH, Guo WS, Jin PK, Dzakpasu M, et al. Current status of urban wastewater treatment plants in China. Environment International 2016;92-93:11-22.

Ziajahromi S, Neale PA, Silveira IT, Chua A, Leusch FD. An audit of microplastic abundance throughout three Australian wastewater treatment plants. Chemosphere 2021;263:Article No. 128294.

INSTRUCTION FOR AUTHORS

Publication and Peer-reviewing processes of Environment and Natural Resources Journal

Environment and Natural Resources Journal is a peer reviewed and open access journal that is published in six issues per year. Manuscripts should be submitted online at https://ph02.tci-thaijo.org/index.php/ennrj/about/submissions by registering and logging into this website. Submitted manuscripts should not have been published previously, nor be under consideration for publication elsewhere (except conference proceedings papers). A guide for authors and relevant information for the submission of manuscripts are provided in this section and also online at: https://ph02.tci-thaijo.org/index.php/ennrj/author. All manuscripts are refereed through a **single-blind peer-review** process.

Submitted manuscripts are reviewed by outside experts or editorial board members of **Environment and Natural Resources Journal**. This journal uses double-blind review, which means that both the reviewer and author identities are concealed from the reviewers, and vice versa, throughout the review process. Steps in the process are as follows:

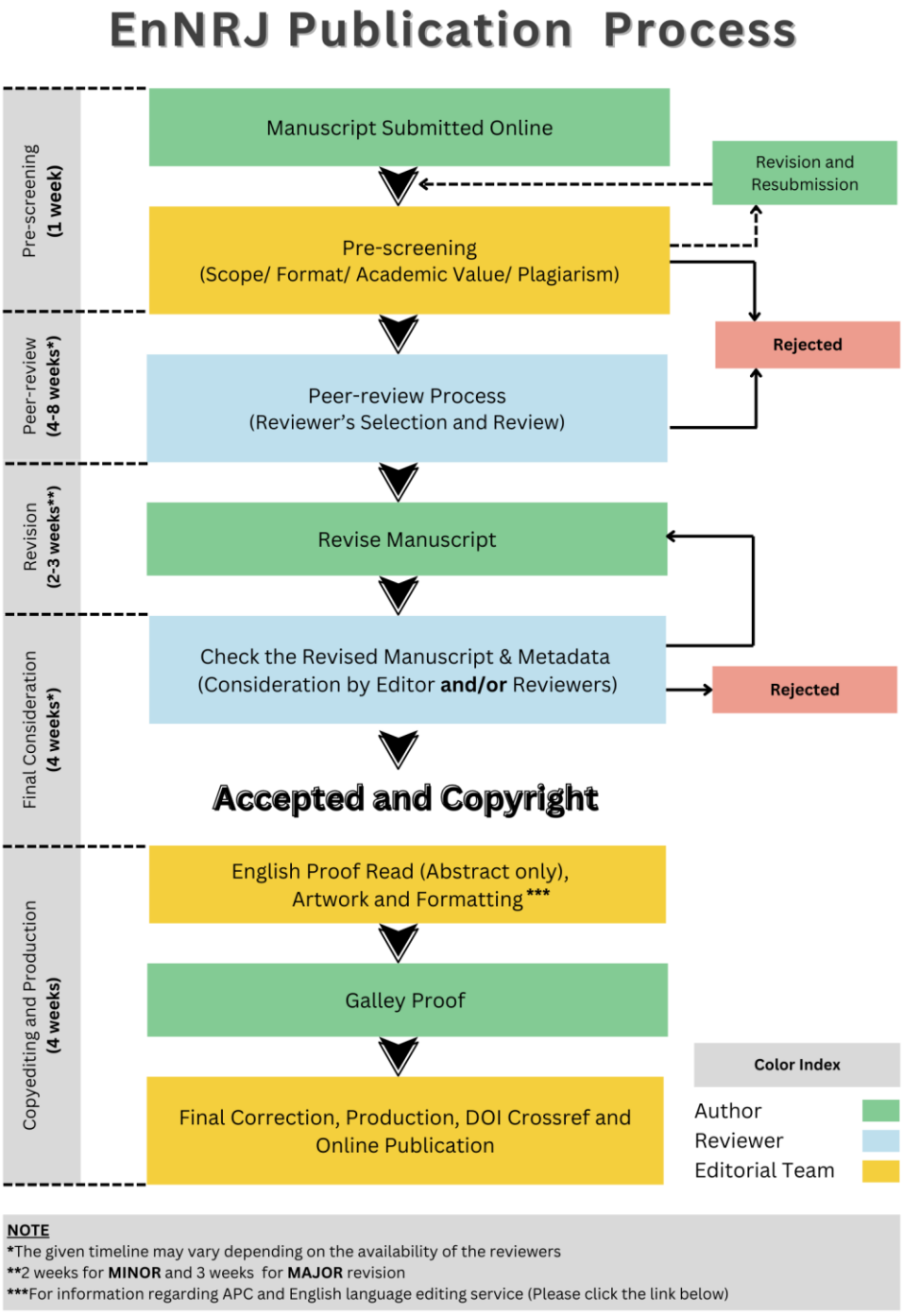

NOTE
*The given timeline may vary depending on the availability of the reviewers
2 weeks for **MINOR and 3 weeks for **MAJOR** revision
***For information regarding APC and English language editing service (Please click the link below)

The Environment and Natural Resources Journal (EnNRJ) considers and accepts two types of articles for publication as follows:

- *Original Research Article*: This is the most common type of article. It showcases new, innovative or unique findings surrounding a focused research question. Manuscripts should not exceed 4,000 words (excluding references) - see more details in the Preparation of Manuscript section below.
- *Review Article (by invitation)*: This type of article focuses on the in-depth critical review of a special aspect of an environmental-related research question, issue, or topic. It provides a synthesis and critical evaluation of the state of the knowledge of the subject. Manuscripts should not exceed 6,000 words (excluding references).

Submission of Manuscript

The items that the author needs to upload for the submission are as follows:

Manuscript: The manuscript must be submitted as a Microsoft Word file (.doc or .docx). Refer to the **Preparation of Manuscript** section below for detailed formatting instructions.

Cover Letter: The letter should address the Editor and include the following: a statement declaring that the author's paper has not been previously published and is not currently under consideration by another journal.

- a brief description of the research the author reports in the paper, including why the findings are important and why the journal readers should be interested
- contact information of the author and any co-authors
- a confirmation that the author has no competing interests to disclose

Graphical Abstract (Optional): The author is encouraged to submit a graphical abstract with the manuscript. The graphical abstract depicts the research and findings with visuals. It attracts more potential readers as it lets them understand the overall picture of the article within a few glances. Note that the graphical abstract must be original and unpublished artwork. It should be a high-quality illustration or diagram in any of the following formats: TIFF, PDF, JPEG, or PNG. The minimum required size is 750 × 750 pixels (height × width). The size should be of high quality (600 dpi or larger) in order to reproduce well.

Reviewers Suggestion (mandatory): Please provide the names of three potential reviewers, with information about their affiliations as well as their email addresses. The recommended reviewers should not have any conflict of interest with the authors. Each reviewer must represent a different affiliation and not have the same nationality as the author. Please note that the editorial board retains the sole right to decide whether or not the recommended reviewers will be selected.

Declaration of Competing Interest: The author must include a declaration of competing interest form during submission. If there is no conflict of interest, please state, "The authors declare no conflict of interest." Otherwise, authors should declare all interests to avoid inappropriate influence or bias in their published work. Examples of potential conflicts of interest in research projects include but are not limited to financial interests (such as employment, consultancies, grants, and other funding) and non-financial interests (such as personal or professional relationships, affiliations, and personal beliefs).

CrediT (Contributor Roles Taxonomy) Author Statement or Author Contributions: For research articles with several authors, we require corresponding authors to provide co-author contributions to the manuscript using the relevant CRediT roles. CRediT is a taxonomy that shows the contributions of the author and co-author(s), reduces possible authorship disputes, and facilitates collaboration among research team members. The CRediT taxonomy includes 14 different roles describing each contributor's specific contribution to the scholarly output.

The roles are: Conceptualization; Data curation; Formal analysis; Funding acquisition; Investigation; Methodology; Project administration; Resources; Software; Supervision; Validation; Visualization; Roles/Writing – original draft; and Writing – review & editing.

Note that authors may have contributed through multiple roles, and those who contributed to the research work but do not qualify for authorship should be listed in the acknowledgments.

An example of a CRediT author statement is given below:
"Conceptualization, X.X. and Y.Y.; Methodology, X.X.; Software, X.X.; Validation, X.X., Y.Y. and Z.Z.; Formal Analysis, X.X.; Investigation, X.X.; Resources, X.X.; Data Curation, X.X.; Writing – Original Draft Preparation, X.X.; Writing – Review & Editing, X.X.; Visualization, X.X.; Supervision, X.X.; Project Administration, X.X.; Funding Acquisition, Y.Y."

Artwork for the Journal Cover: The author may provide and propose a piece of artwork (with a description) for the journal issue cover. This is an excellent opportunity for the author to promote their article, if accepted, on the cover of a published issue. Alternatively, the editorial team may invite the author to submit a piece of artwork for the cover after their manuscript has been accepted for publication. The final cover artwork selection will be made by the editorial team.

Final Author Checks: In addition to the basic requirements, the author should review this checklist before submitting their manuscript. Following it ensures the manuscript is complete and in accordance with all standards.

Preparation of Manuscript

Format and Style

The manuscript should be prepared strictly as per the guidelines given below. Any manuscript with an incorrect format will be returned, and the corresponding author may have to resubmit a new manuscript with the correct format.

Overall Format

The manuscript must be submitted as a Microsoft Word file (.doc or .docx). The formatting should be as follows:

- File format - .doc or .docx
- Page size - A4
- Page orientation - portrait (some landscape pages are accepted if necessary)
- Page margin - 2.54 cm (left and the right margin) and 1.9 cm (bottom and the top margin)
- Page number (bottom of the page)
- Line number
- Line spacing - 1.5
- Font - 12 point, Times New Roman (unless stated otherwise)

Unit - The use of abbreviation must follow the International System of Units (SI Unit) format.

- The unit separator is a virgule (/) and not a negative coefficient: 10 mg/L not 10 mgL^{-1}
- Liter always has a capital letter: mg/L

Equations

- Insert equations using the dedicated tool in Microsoft Word. Do not use pictures or text boxes.
- Equations that are referenced in the text should be identified by parenthetical numbers, such as (1), and should be referred to in the manuscript as “Equation 1”.

Inclusive Language: The language used in the manuscript acknowledges diversity, promotes equal opportunity, respects all people, and is sensitive to all aspects of differences. The manuscript content should not make assumptions about the beliefs or commitments of any individual. It should not imply superiority regarding age, race, ethnicity, culture, gender, sexual orientation, disability, or health conditions. Moreover, the manuscript must be free from bias, stereotypes, slang, and derogatory terms.

Reference Style: Vancouver style should be used for the reference list and in-text citations throughout the manuscript. Please follow the format of the sample references and citations, as shown in the Body Text Sections portion below.

Front Page

Title: The title of the manuscript should be concise and not longer than necessary. The title should be bold, 12-point size, and Times New Roman. The first letter of major words should be capitalized (as in standard title case).

Author(s) Name: The first and last names of all authors must be given, in bold, Times New Roman, and 12-point font.

Affiliation of All Author(s): Affiliation(s) must be in italics, Times New Roman, and 11-point font. Specify the Department/School/Faculty, University, City/Province/or State, and Country of each affiliation. Do not include positions or fellowships, or postal zip codes.
Each affiliation should be indicated with superscript Arabic numerals. The Arabic numeral(s) should appear immediately after the author’s name, and represent the respective affiliation(s).

Corresponding Author: One author should be responsible for correspondence, and their name must be identified in the author list using an asterisk (*).

- All correspondence with the journal, including article submission and status updates, must be handled by the corresponding author.

- The online submission and all associated processes should be operated by the corresponding author.

*Corresponding author: followed by the corresponding author's email address.

Example:

Papitchaya Chookaew[1], Apiradee Sukmilin[2], and Chalor Jarusutthirak[1*]
[1]Department of Environmental Technology and Management, Faculty of Environment, Kasetsart University, Bangkok, Thailand
[2]Environmental Science and Technology Program, Faculty of Science and Technology, Phranakhon Rajabhat University, Bangkok, Thailand
**Corresponding author: abcxx@xx.ac.th*

Abstract Page

Abstract: The abstract should include the significant findings paired with relevant data. A good abstract is presented in one paragraph and is limited to 250 words. Do not include a table, figure, or references.
Keywords - Up to six keywords are allowed, and they should adequately index the subject matter.

Highlights: Please include 3-5 concise sentences describing innovative methods and the findings of the study. Each sentence should contain at most 85 characters (not words).

Body Text Sections
The main body text of the manuscript normally includes the following sections: 1. Introduction 2. Methodology 3. Results and Discussion 4. Conclusions 5. Acknowledgments 6. Author Contributions 7. Declaration of Competing Interests 8. References

Introduction should include the aims of the study. It should be as concise as possible, with no subheadings. The significance of the problem and the essential background should also be given.

Methodology is sufficiently detailed so that the experiments can be reproduced. The techniques and methods adopted should be supported with standard references.
There should be no more than three levels of headings in the **Methodology and Results and Discussion** sections. Main headings are in bold letters, second-level headings are in bold and italic letters, and third-level headings are in normal letters.

Here is an example:

2. Methodology
2.1 Sub-heading
2.1.1 Sub-sub-heading

Results presents the key findings in figures and tables with descriptive explanations in the text.

Tables
- Tables - look best if all the cells are not bordered; place horizontal borders only under the legend, the column headings, and the bottom.

Figures
- Figures - should be submitted in color. The author must ensure that the figures are clear and understandable. Regardless of the application used to create them, when electronic artworks are finalized, please 'save as' or convert the images to TIFF or JPG and send them separately to EnNRJ. Images require a resolution of at least 600 dpi (dots per inch) for publication. The labels of the figures and tables must be Times New Roman, and their size should be adjusted to fit the figures without borderlines.
- Graph - The font style in all graphs must be Times New Roman, 9-10 size, and black color. Please avoid bold formatting, and set the border width of the graphs to 0.75 pt.

- Graph from MS Excel: Please attach an editable graph from MS Excel within your manuscript. Then please also submit the full MS Excel file used to prepare the graph as a separate document. This helps us customize our layout for aesthetic beauty.
- Graph from another program: Feel free to use whichever program best suits your needs. But as noted above, when your artwork is finalized, please convert the image to TIFF or JPG and send them separately Again, images should be at least 600 dpi. Do not directly cut and paste.

***All figures and tables should be embedded in the text, and also mentioned in the text.**

Discussion shows the interpretation of findings with supporting theory and comparisons to other studies. The Results and Discussion sections can be either separated, or combined. If combined, the section should be named Results and Discussion. **Conclusions** should include a summary of the key findings and take-home messages. This should not be too long, or repetitive but this section is absolutely necessary so that the argument of the manuscript is not uncertain or left unfinished.

Acknowledgments should include the names of those who contributed substantially to the work, but do not fulfill the requirements for authorship. It should also include any sponsor or funding agency that supported the work.

Author Contributions: For research articles with several authors, we require corresponding author contributions listed using the relevant CRediT roles. This should be done by the author responsible for correspondence.

Declaration of Competing Interest: The author must include a declaration of competing interest form during submission. If there is no conflict of interest, please state, "The authors declare no conflict of interest." Otherwise, authors should declare all interests to avoid inappropriate influence or bias in their published work.

References should be cited in the text by the surname of the author(s) and the year. This journal uses the author-date method of citation. The author's last name and date of publication are inserted in the text in the appropriate place. If there are more than two authors, “et al.” must be added after the first author’s name. Examples: (Frits, 1976; Pandey and Shukla, 2003; Kungsuwas et al., 1996). If the author’s name is part of the sentence, only the date is placed in parentheses: “Frits (1976) argued that . . .”

Please ensure that every reference cited in the text is also in the reference list (and vice versa).

In the list at the end of the manuscript, complete references must be arranged alphabetically by the surnames of the first author in each citation. Examples are given below.

Book

Tyree MT, Zimmermann MH. Xylem Structure and the Ascent of Sap. Heidelberg, Germany: Springer; 2002.

Chapter in a book

Kungsuwan A, Ittipong B, Chandrkrachang S. Preservative effect of chitosan on fish products. In: Steven WF, Rao MS, Chandrkachang S, editors. Chitin and Chitosan: Environmental and Friendly and Versatile Biomaterials. Bangkok: Asian Institute of Technology; 1996. p. 193-9.

Journal article

Muenmee S, Chiemchaisri W, Chiemchaisri C. Microbial consortium involving biological methane oxidation in relation to the biodegradation of waste plastics in a solid waste disposal open dump site. International Biodeterioration and Biodegradation 2015;102(3):172-81.

Journal article with Article Number

Sah D. Concentration, source apportionment and human health risk assessment of elements in $PM_{2.5}$ at Agra, India. Urban Climate 2023;49:Article No. 101477.

Non-English articles

Suebsuk P, Pongnumkul A, Leartsudkanung D, Sareewiwatthana P. Predicting factors of lung function among motorcycle taxi drivers in the Bangkok metropolitan area. Journal of Public Health 2014;44(1):79-92 (in Thai).

Article in press

Dhiman V, Kumar A. Biomass and carbon stock estimation through remote sensing and field methods of subtropical Himalayan Forest under threat due to developmental activities. Environment and Natural Resources Journal 2024. DOI: 10.32526/ennrj/22/20240018.

Published in conference proceedings

Wiwattanakantang P, To-im J. Tourist satisfaction on sustainable tourism development, Amphawa floating market Samut Songkhram, Thailand. Proceedings of the 1st Environment and Natural Resources International Conference; 2014 Nov 6-7; The Sukosol hotel, Bangkok: Thailand; 2014.

Ph.D./Master thesis

Shrestha MK. Relative Ungulate Abundance in a Fragmented Landscape: Implications for Tiger Conservation [dissertation]. Saint Paul, University of Minnesota; 2004.

Website

Orzel C. Wind and temperature: why doesn't windy equal hot? [Internet]. 2010 [cited 2016 Jun 20]. Available from: http://scienceblogs.com/principles/2010/08/17/wind-and-temperature-why-doesn/.

Report organization

Intergovernmental Panel on Climate Change (IPCC). IPCC Guidelines for National Greenhouse Gas Inventories: Volume 1-5. Hayama, Japan: Institute for Global Environmental Strategies; 2006.

Royal Gazette

Royal Gazette. Promotion of Marine and Coastal Resources Management Act 2059. Volume 132, Part 21, Dated 26 Mar B.E. 2558. Bangkok, Thailand: Office of the Council of State; 2015a. (in Thai).

Remark

** Please be note that manuscripts should usually contain at least 15 references and some of them must be up-to-date research articles.*

** Please strictly check all references cited in text, they should be added in the list of references. Our Journal does not publish papers with incomplete citations.*

Changes to Authorship

This policy of journal concerns the addition, removal, or rearrangement of author names in the authorship of accepted manuscripts:

Before the accepted manuscript

For all submissions, that request of authorship change during review process should be made to the form below and sent to the Editorial Office of EnNRJ. Approval of the change during revision is at the discretion of the Editor-in-Chief. The form that the corresponding author must fill out includes: (a) the reason for the change in author list and (b) written confirmation from all authors who have been added, removed, or reordered need to confirm that they agree to the change by signing the form. Requests form submitted must be consented by corresponding author only.

After the accepted manuscript

The journal does not accept the change request in all of the addition, removal, or rearrangement of author names in the authorship. Only in exceptional circumstances will the Editor consider the addition, deletion or rearrangement of authors after the manuscript has been accepted.

Copyright transfer

The copyright to the published article is transferred to Environment and Natural Resources Journal (EnNRJ) which is organized by Faculty of Environment and Resource Studies, Mahidol University. The accepted article cannot be published until the Journal Editorial Officer has received the appropriate signed copyright transfer.

Online First Articles

The article will be published online after receipt of the corrected proofs. This is the official first publication citable with the Digital Object Identifier (DOI). After release of the printed version, the paper can also be cited by issue and page numbers. DOI may be used to cite and link to electronic documents. The DOI consists of a unique alpha-numeric character string which is assigned to a document by the publisher upon the initial electronic publication. The assigned DOI never changes.

Mahidol University

Wisdom of the Land

Faculty of Environment and Resource Studies, Mahidol University, Thailand
999 Phutthamonthon Sai 4 Rd, Salaya, Phutthamonthon District, Nakhon Pathom 73170
E-mail: ennrjournal@gmail.com